universität wien

MASTERARBEIT / MASTER'S THESIS

Titel der Masterarbeit / Title of the Master's Thesis

„Stellar wind simulations in the age of PSP and Solar Orbiter"

verfasst von / submitted by

Simon Schleich, BSc

angestrebter akademischer Grad / in partial fulfilment of the requirements for the degree of

Master of Science (MSc)

Wien, 2021 / Vienna 2021

Studienkennzahl lt. Studienblatt / degree programme code as it appears on the student record sheet:	A 066 861
Studienrichtung lt. Studienblatt / degree programme as it appears on the student record sheet:	Masterstudium Astronomie
Betreut von / Supervisor:	Dr. Sudeshna Boro Saikia

Abstract

Being the star closest to Earth, the Sun provides us with the only possibility of *in situ* measurements regarding its continuous mass flow emanating into the heliosphere. This *solar wind*, as understood today, was initially proposed over 50 years ago. Numerous science missions have advanced our understanding of this phenomenon, but the exact nature of its origin and driving forces in the solar corona are still very active fields of study. Research in the evolutionary processes of the Sun, as well as investigations of stellar winds associated to solar-like stars are closely connected to our understanding of the solar wind.

In this work, I have used the 3D MHD code `NIRVANA` to generate a single-fluid, global model of the magnetized solar wind. I have modified the code to include a wave-turbulence driven heating mechanism, accelerating the solar wind. Additionally, I have analysed a large amount of measurements taken by the *Parker Solar Probe* and *Solar Orbiter*. This data provides empirical constraints on solar wind parameters over a large range of heliocentric distances. Through certain constraints imposed by and on the code, the model represents a somewhat basic approach to this complex problem. The resulting solar wind parameter profiles reproduce the general radial behaviour seen in the *in situ* measurement constraints, although they are not in exact agreement.This displays the potential of further improving this model to generate a more accurate solar wind description that can be used to investigate the behaviour of stellar winds.

Zusammenfassung

Als der der Erde am nächsten gelegene Stern bietet uns die Sonne die einzige Möglichkeit, den kontinuierlichen Massenstrom, der von ihr in die Heliosphäre eindringt, *in situ* zu messen. Dieser *Sonnenwind*, wie er heute verstanden wird, wurde ursprünglich vor über 50 Jahren postuliert. Zahlreiche wissenschaftliche Missionen haben unser Verständnis dieses Phänomens verbessert, aber die genaue Natur seines Ursprungs und die treibenden Kräfte in der Sonnenkorona sind immer noch sehr aktive Forschungsgebiete. Die Erforschung der Entwicklungsprozesse der Sonne sowie die Untersuchung stellarer Winde in Verbindung mit sonnenähnlichen Sternen sind eng mit unserem Verständnis des Sonnenwindes verbunden.

In dieser Arbeit habe ich den 3D-MHD-Code `NIRVANA` verwendet, um ein globales Ein-Fluid-Modell des magnetisierten Sonnenwindes zu erstellen. Ich habe den Code so modifiziert, dass er einen wellen-turbulenzgetriebenen Heizmechanismus inkludiert, welcher den Sonnenwind beschleunigt. Außerdem habe ich eine große Anzahl an Messungen analysiert, die von der *Parker Solar Probe* und dem *Solar Orbiter* durchgeführt wurden. Diese Daten liefern empirische Begrenzungen der Sonnenwindparameter über einen großen Bereich heliozentrischer Entfernungen. Durch bestimmte Beschränkungen, die durch und auf den Code auferlegt werden, stellt das Modell einen recht einfachen Ansatz für dieses komplexe Problem dar. Die sich daraus ergebenden Parameterprofile des Sonnenwindes reproduzieren das allgemeine radiale Verhalten, das sich aus den *in situ* Messungen ergibt, wobei sie sich nicht in genauer Übereinstimmen befinden. Dies zeigt das Potenzial für eine weitere Verbesserung dieses Modells, um eine genauere Beschreibung des Sonnenwindes zu erstellen, die zur Untersuchung des Verhaltens von Sternwinden verwendet werden kann.

Acknowledgments

First and foremost, I would like to thank my thesis supervisor, Dr. Sudeshna Boro Saikia, for the continuous support and input I have received during the process of working on this project. Her door, both physically and virtually during this at times trying last year, was always open for me to barge in and ask my questions. I also want to extend my gratitude to Michael Bartel and Lukas Winkler, who both helped me understand `C` and the intricacies of an extensive numerical code whenever these topics went over my head.

For the use of data I acknowledge the NASA Parker Solar Probe Mission and the SWEAP team led by J. Kasper, as well as Solar Orbiter as a mission of international cooperation between ESA and NASA, operated by ESA. This work used the `NIRVANA` code developed by Udo Ziegler at the Leibniz-Institut für Astrophysik Potsdam. The presented results were partially achieved at the Vienna Scientific Cluster (VSC) and data visualization was partially achieved using VisIt, SpiceyPy and the SPICE toolkit.

Finally, I would like to express my deepest gratitude to my family: without their continuous encouragement and support, I might not haven been able to climb over many a rock strewn on this road. I want to thank my parents for enduring my long ramblings on the problems I was working on, even if the subject matter might not have been the most interesting to them, and for letting me now that sometimes it is alright to take a breather. I want to thank my grandfather, who has shown me that a fascination for all things scientific in space can hit you, no matter your age or academic background. And I want to thank my grandmother, for her frequent calls and never ending positive attitude, giving me alleviation during some of the more stressful days. I am grateful for all of your support.

Simon Schleich

Contents

List of Figures

List of Abbreviations

AMR adaptive mesh refinement

CME coronal mass ejection

HCS heliospheric current sheet

HIC heliocentric inertial coordinates

IMR initial mesh refinement

MHD magnetohydrodynamics

PSP Parker Solar Probe

SolO Solar Orbiter

SPAN Solar Probe Analyzers

SPC Solar Probe Cup

SWA Solar Wind Analyzer

SWA-PAS Proton-Alpha System

SWEAP Solar Wind Electrons, Alphas and Protons

WTD wave-turbulence driven

Chapter 1

Introduction

As our nearest star, the Sun has fascinated humanity for thousands of years. Together with our ever expanding knowledge of the Solar System, we have also increased our ability to observe and understand the Suns role in it. Among the many discoveries made in studying the heliosphere is the knowledge that an ever-present mass flow radiates from the Sun throughout the Solar System (Biermann 1951; Parker 1958), now known as the *solar wind*. It is now well established that this phenomenon greatly influences the conditions in the heliosphere and that it can have a significant impact on planetary atmospheres and their magnetic fields (see e.g. Cohen et al. 2014; Kislyakova et al. 2014; Lichtenegger et al. 2010).

Since a stellar mass flow carries away angular momentum from the star, understanding the solar wind is also an important factor in the rotational evolution of the Sun (Matt et al. 2012). The rotation rate, magnetic field and mass flow of the Sun are connected in a closely linked circle - the rotation of the Sun influences its magnetic field, which in turn drives the acceleration of the solar wind, and the solar wind itself slows down the rotation of the Sun (Vidotto 2021). Expanding our knowledge in one of these areas is therefore also important in overall investigations about the solar evolution.

Since the detection of the first exoplanetary systems, thousands of new host stars have been identified, many of them similar to the Sun[1] . It is therefore reasonable to make efforts in relating our increasing knowledge of the solar wind to other stellar hosts in an attempt to study the impact of stellar winds in exoplanetary systems: both on the host star and on potential planets in orbit around them. Knowing what governs and drives the main components of the solar wind, and how its behaviour changes for different types of host stars, is therefore a key factor in the study of exoplanetary system conditions. However, because the Sun is the only star for which we can directly measure the parameters of a stellar wind, it is important that we find viable ways of describing the solar wind based on

[1] *The Extrasolar Planets Encyclopaedia*.

physical mechanisms and backed up by observations.

1.1 The Sun and the Heliosphere

The idea of a causal link between events on the Sun and on Earth is not a recent conclusion. A famous example for this is a coronal mass ejection (CME) observed in the late nineteenth century, which was closely followed by a strong geomagnetic storm (Carrington 1859; Hodgson 1859), now known as the *Carrington Event*. The observation of such phenomena lead to deliberations about a transient connection between highly energetic events on the Sun and their impact on Earth. As an example, Chapman (1918) linked these geomagnetic events to beams of corpuscular radiation emitted from the Sun. While these conclusions are applicable in the case of rare and highly energetic events such as CMEs, it would be another few decades before the now well established theory about a continuous mass flow connecting the Sun to the broader heliosphere would be published (Parker 1958, 1965).

Shortly after the observations from Carrington (1859), the first spectroscopic analyses of the tenuous outer solar atmosphere resulted in the observation of spectral emission lines not connected to any known element at that time. As discussed by Cranmer and Winebarger (2019), these lines were initially thought to signify the identification of previously unknown elements. However, as later work showed, they actually represent unusually high ionization states of already known elements (Cranmer and Winebarger 2019) and point towards an extremely high temperature regime of the solar corona. It is somewhat debated who should be accredited for the discovery and conclusions about a solar corona in the million degree temperature regime (Cranmer and Winebarger 2019; Peter and Dwivedi 2014; Russell 2018), but the general consensus seems to be that the work of Grotrian (1939) and Edlén (1943) on the identification of forbidden lines in the solar spectrum lead to establishing the idea of a hot corona, while Alfvén (1941) underlined this with additional evidence pointing towards an outer region of the solar atmosphere in a temperature range above $1\,\mathrm{MK}$.

It was Parker (1958) who famously investigated the idea of a solar corona that was not static, but rather in a state of continuous radial expansion. This was based on observations of comet tails. Biermann (1951) studied the behaviour of steadily anti-sunward pointing tails consisting of ions, and proposed that their behaviour should be explained not only through solar radiation pressure, but also a necessary additional contribution from a continuously emitted corpuscular radiation emanating from the Sun. The author already suggested a velocity regime on the order of $1000\,\mathrm{km\,s^{-1}}$ for this continuous gas outflow, and densities ranging from 1×10^2 to $1 \times 10^5\,\mathrm{cm^{-3}}$ between magnetically quiet periods and geomagnetic storms (Biermann 1951, 1957).

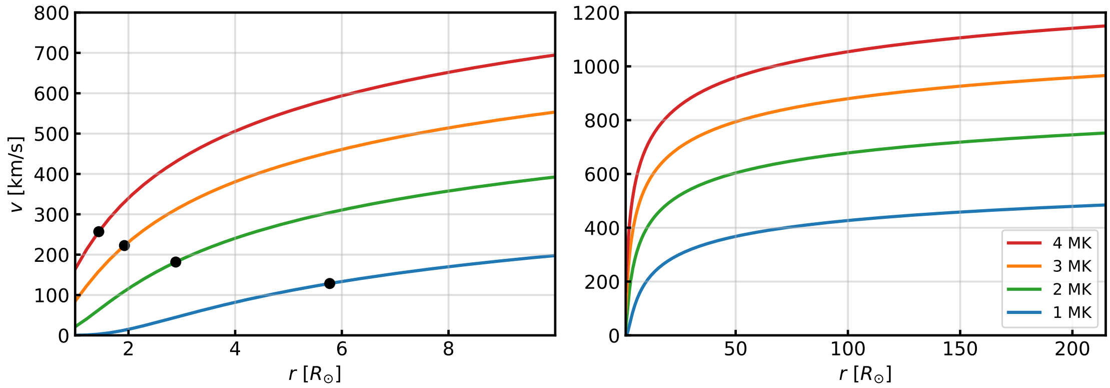

Figure 1.1: Solutions for the *Parker Wind* showing the solar wind velocity v in $\mathrm{km\,s^{-1}}$ with respect to the distance from the solar surface r in units of $\mathrm{R}_\odot$ between $1\,\mathrm{R}_\odot$ and $1\,\mathrm{AU}$, and isothermal coronal temperatures of 1, 2, 3 and 4 MK. The left panel shows velocities for the first 10 $\mathrm{R}_\odot$ where the location of the critical point $r_c \propto T^{-1}$ as a transition between the sub- and supersonic regime is marked with filled-in circles. The right panel shows the whole distance range, illustrating that the solar wind is accelerated heavily in regions close to the Sun, but this rapid increase in velocity tapers off at large distances. Higher assumed coronal temperatures result in overall larger velocities.

Parker (1958) took these observations and investigated the potential dynamical behaviour of the corona in connection with the million degree temperature regime already established for this region. The author argued that a hydrostatic solution for the solar atmosphere would not be possible due to a non-vanishing pressure gradient at large distances - his conclusion, therefore, was to look for solutions in the form of a steadily expanding corona. He proposed that the fluid velocity must transition from a subsonic regime close to the Sun into a supersonic expansion at large distances. To illustrate the expected behaviour of the solar wind with respect to distance from the Sun, it is helpful to look at the most basic form of the wind solution as presented by Parker (1965): an isothermal corona in radially symmetric steady expansion without any influence of a magnetic field. Fig. 1.1 shows radial solar wind velocity profiles for different isothermal temperatures. It can easily be seen that the wind is heavily accelerated within approximately 15 $\mathrm{R}_\odot$, but this gradient flattens at large distances. The solutions in Fig. 1.1 strongly depend on the assumed isothermal temperature of the solar corona, and it is apparent that higher temperatures lead to greater acceleration and higher maximum velocities of the solar wind. A derivation of the *Parker Wind equation* can be found in Appendix A. It is of interest to point out that Parker's solution was initially met with heavy criticism, though the emergence of space missions measuring the properties of the interplanetary plasma quickly proved the existence of a supersonic solar wind [2] .

[2] As Parker recounts himself, the original paper, submitted to the *Astrophysical Journal* in 1958, was judged to be misguided by two referees, with a recommendation against publication (Parker 2001, p. 245). At Parker's insistence that no valid criticism was leveled at his description, the paper was published regardless, and the scientific community only had to wait a few years to find observational confirmation for the existence of a

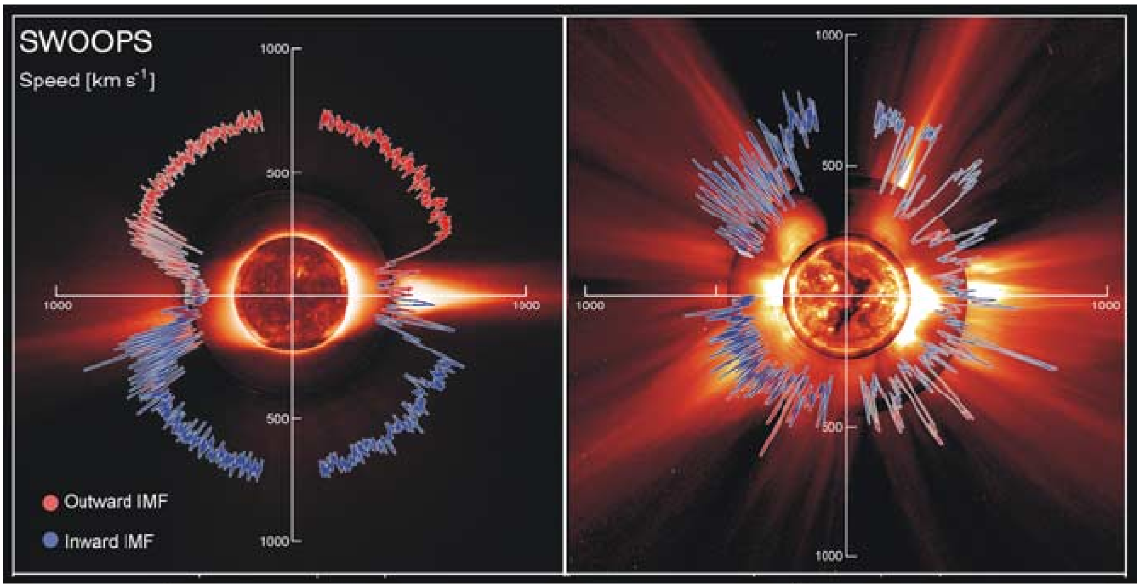

Figure 1.2: Ulysses measurements of solar wind speeds with varying heliolatitude. During the solar minimum (left panel), these measurements show a distinct separation between the fast wind regime ($\sim 750\,\mathrm{km\,s^{-1}}$) at high heliolatitudes and the slow wind regime ($\sim 350\,\mathrm{km\,s^{-1}}$) closer to the solar equator. This global structure of the solar wind completely changes during the solar maximum (right panel), where flows of variable velocities can be observed at all heliolatitudes. In both panels, the red and blue colouration signify outward and inward pointing magnetic field lines respectively. The underlying images are a composite of EUV and white light coronagraph images of the Sun, characteristic for the solar minimum (1996, left) and maximum (2000, right). Image (altered) reproduced from McComas et al. (2003) under the AGU permissions policy.

1.2 The Solar Wind

At the dawn of the space age, shortly after Parker published his seminal paper on the matter, Neugebauer (1997) recalls that instruments onboard the earliest space missions were designed to take measurements in ranges corresponding to several competing theories about the state of the interplanetary plasma: a hot, static solar corona (Chapman and Zirin 1957), Parker's supersonic radial expansion and a subsonic *solar breeze* solution (Chamberlain 1960). Early space missions such as Explorer 10 in 1961 and Mariner 2 in 1962 were able to detect these properties of the solar wind and confirm Parker's model of a supersonically expanding, low-density plasma, together with a major new discovery - a respective bimodal distribution in the velocity and density regime of the solar wind, now called the *slow* and *fast wind* (Cranmer and Winebarger 2019; Neugebauer 1997).

Successful missions after that point further solidified Parker's model, such as Helios 1 and 2 (Marsch et al. 1982), as well as the Ulysses mission, which followed highly inclined orbits measuring the solar wind parameters far outside the ecliptic plane (McComas et al. 1998, 2003). Fig. 1.2 displays the bimodal distribution of the solar wind speed measured by Ulysses. This figure illustrates the global wind structure dependence on the state of the

continuous, supersonic stream of corpuscular radiation throughout the solar system (Parker 2001, p. 248).

solar cycle: during the solar minimum, the wind speed shows a clear distinction between the slow regime at the solar equatorial regions, and the fast regime at higher heliolatitudes. This structure completely changes during the solar maximum, when flows of variable velocities can be found at all heliolatitudes (McComas et al. 2003).

Currently, the Parker Solar Probe (PSP), launched in 2018, and the Solar Orbiter (SolO), launched in 2020, continue the advancement in measuring the plasma parameters of the solar wind at increasing proximity to its source (Kasper et al. 2016; Müller et al. 2020).

1.2.1 Including a Magnetic Field

While the above mentioned, purely hydrodynamic solution might be the best known result of his seminal paper on this topic, Parker already discussed a connection between the ionized solar wind and the solar magnetic field - the ionized mass outflow is coupled to the magnetic field and carries it into the heliosphere. If assumed to be a radial field in the simplified case, the magnetic field lines form a spiral pattern inside the rotational frame of reference of the Sun (Parker 1958) - if the outflow velocity is assumed to be constant after some distance from the solar surface, this pattern forms an Archimedean spiral. Because of the dipolar nature of the solar magnetic field at large distances, this spiral structure is also reflected in a transition region between positive and negative polarity of the field called the heliospheric current sheet (HCS) (Smith 2001; Wilcox and Ness 1965).

Because the magnetized solar wind is coupled to the solar magnetic field, it can also be inferred that the radial expansion of the corona exerts a torque on the Sun through magnetic stress. This torque leads to a spin-down of the solar rotation rate, which is why solar wind descriptions are necessary in analyses of the solar evolution (Johnstone et al. 2015a,b; Matt et al. 2012; Vidotto 2021). In relation between the wind velocity and transferred angular momentum, is important to note that the wind is trans-Alfvénic. At a critical point r_A, called the Alfvén point (or Alfvén surface in three dimensions), the wind speed becomes larger than the Alfvén velocity $v_A = B / \sqrt{4\pi\rho}$, where B is the magnetic field strength and ρ is the mass density (Vidotto 2021). The angular momentum loss through the wind, which contributes to the solar rotational evolution, can then be characterized with the mass loss rate, the solar rotation rate and the specific angular momentum at r_A (Cohen and Drake 2014).

The complexity of the connection between the solar magnetic field, the driving parameters of the solar wind acceleration and the distribution of the solar wind regimes is still not fully understood. Investigating the relation between the solar corona and the mass flow emanated into the heliosphere represents a very active field of study, with the goal of identifying the correct physical mechanisms behind the driving forces of the solar wind.

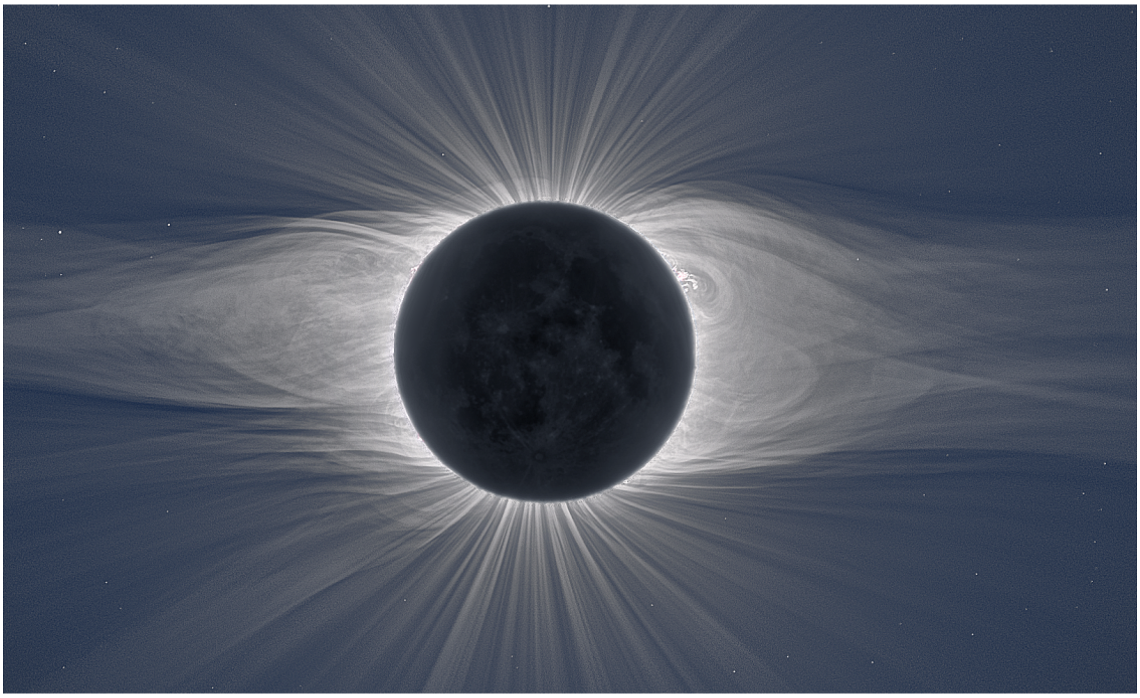

Figure 1.3: Composite white-light image of the solar corona taken during a 2019 total solar eclipse near Tres Cruses, Chile. It illustrates the distribution of polar coronal holes (open magnetic field lines) and equatorial coronal streamers (closed magnetic loops) during the solar minimum, coinciding with the origins of the fast and slow solar wind regimes. Image credit: M. Druckmüller and P. Aniol. Image reproduced with permission from M. Druckmüller.

1.2.2 The Role of the Solar Corona

Advancing the scientific consensus about the nature and origin of the solar wind means moving past the illustrative, but simplified assumptions Parker made in his initial paper. This implies the necessity of more accurate information about the structure and physical properties connected to the origin of the solar wind - namely the solar corona. As McComas et al. (2003) pointed out, the measurements taken from Ulysses during its first and second orbit allowed a comparison of the global solar wind structure during a solar cycle. At the solar minimum, observed during Ulysses' first orbit, there is a noticeable separation between the fast solar wind regime emanating from high heliolatitudes and the equatorial slow wind regime (McComas et al. 1998). This picture gives way to a much more complicated and intermixed structure during the solar maximum observed in Ulysses' second orbit, with fast and slow wind emanating from all heliolatitudes (McComas et al. 2003). This behaviour is also illustrated in Fig. 1.2, showing a comparison between the wind speed measurements taken by Ulysses during the solar cycle.

The state of the solar cycle is closely connected with its magnetic morphology: during the solar minimum, large regions of low-density plasma and open magnetic field lines called *coronal holes* cover the solar poles - they are generally regarded as super-radially expanding bundles of open flux tubes that act as the source regions of the fast solar wind (Cranmer 2009). In contrast to them, the solar surface regions covered with closed magnetic loops seem to be connected to bright, elongated features called *streamers*, which coincide with the origination of the slow solar wind (Cranmer 2009). Fig. 1.3 illustrates the distribution of polar coronal holes and equatorial streamer regions during the solar activity minimum. During the maximum in the solar activity cycle, this neatly ordered picture between the location of coronal holes and streamers gives way to a more complex distribution of these features, closely correlated to the intermixed wind structure mentioned above (McComas et al. 2003). As solar wind models get more complex, reproducing a more detailed magnetic topology illustrative of the activity cycle can therefore help in generating more accurate global models of wind parameters (Boro Saikia et al. 2020; Vidotto et al. 2014b). Even though this complexity better reflects the magnetic field structure at close distances, the heliospheric magnetic field can be assumed to have a purely radial nature after a few $R_{\odot}$, where $|B_r|/|B|$ approaches unity (Riley et al. 2006). All these concepts listed above illustrate the high degree of complexity introduced to investigations regarding accurate representations of both the solar wind in our own vicinity, as well as their translation to generalized descriptions of stellar winds from solar-like stars.

1.2.3 The Coronal Heating Problem

Despite decades of study, the exact mechanisms that heat the solar corona and drive the solar wind are still not known, representing an open question in the field of astrophysics called the *coronal heating problem* - Energy has to be transported from the photosphere through the chromosphere and then deposited in the corona by some mechanism, translating mechanical into thermal energy (Cranmer and Winebarger 2019).

An extensive review of possible mechanisms used to explain the energy transport and subsequent deposition into the corona can be found in Cranmer and Winebarger (2019), where the authors describe a plethora of processes differentiated by the influence of two time scales: the Alfvén travel time τ_A and a photospheric driving time τ_{ph}. The parameter τ_A characterizes a time scale at which perturbations travel along magnetic field lines from the photosphere into the corona, where as τ_{ph} describes the influence of granular motions to the magnetic field footpoint configuration (Cranmer and Winebarger 2019).

Comparing these two time scales, it can be seen that the limiting case of $\tau_A \ll \tau_{\text{ph}}$ corresponds to a series of slowly evolving states of equilibrium, where energy is released through reconnection events connected to the braided magnetic field lines (Parker 1972; Sturrock and Uchida 1981). The other constraining case, $\tau_A \gg \tau_{\text{ph}}$, represents a state where the rapid footpoint motion of the magnetic field induces a continuous jostling of magnetic flux tubes. The induced Alfvén waves are used to explain the energy deposition in the corona through damping processes (e.g. Osterbrock 1961), or through the development of turbulence and subsequent cascade of energy (Hollweg 1986; Matthaeus et al. 1999).

As stated by Cranmer and Winebarger (2019), the complexity of the connection between the solar corona and the solar wind will require a combination of these mechanisms to most accurately reproduce this physical system. A lack of direct observations within the regions of interest connected to the heating of the solar corona and wind poses a problem in investigations around this matter. The advent of PSP and SolO, with planned minimum perihelia of $10\,\mathrm{R}_{\odot}$ and $60\,\mathrm{R}_{\odot}$ respectively (Kasper et al. 2016; Müller et al. 2020), marks a major step forward into directly investigating these scientific questions.

1.2.4 Solar Wind Models

As mentioned previously, Parker (1958, 1965) circumvented the necessity of a particular description leading to the actual formation of a temperature profile describing the heating of the solar corona. The answer to this question is still a very active field of study. Since the initial description of the solar wind, models describing the nature and behaviour of this mass flow have evolved to more accurately reflect *in situ* measurements of the corresponding parameters, and to include better physical descriptions taking the driving forces of the solar wind into account (Gombosi et al. 2018; Vidotto 2021).

With appropriate models of the solar wind, it becomes possible to investigate the mass flow of solar-like stars that show a similar phenomenon, but that differ in key parameters modulating their actual wind behaviour (Cohen and Drake 2014; Matt et al. 2012). As a fully ionized plasma mainly consisting of hydrogen atoms, solar wind models can be generated through a magnetohydrodynamic fluid treatment, where models of increasing complexity move from a single fluid assumption away to also include different species such as electrons or helium ions (Gombosi et al. 2018).

One approach commonly used to model the behaviour of the solar wind, and stellar winds of low-mass stars by extension, is by simplifying the energy-equation through the introduction of a polytropic equation of state, taking the form of a power-law relation between the thermal pressure and the density $\left(p \propto \rho^{\Gamma}\right)$. Working with this relation implicitly assumes the heating of the expanding wind, where the temperature follows the mass density $\left(T \propto \rho^{\Gamma-1}\right)$. The exponent Γ defines the temperature behaviour of the model. $\Gamma = 1$ correlates to an isothermal description where the temperature is independent of the mass density. A value of $\Gamma > 1$ leads to a falling temperature profile, and $\Gamma = 5/3$ is equivalent to an adiabatic expansion process. Polytropic wind models can assume a constant value of Γ for the whole wind domain, where an appropriate polytropic index for the solar wind, based on measurements, ranges between 1.1 and 1.48 (Vidotto 2021). A more complex approach has been presented by e.g. Johnstone et al. (2015b), where the polytropic index is chosen to vary based on distance from the Sun. Since polytropic wind models consider simplified assumptions about the physical processes behind the heating and acceleration of the wind, complexity can be added in other aspects: their domains can be chosen on a larger scale to study the global wind behaviour, and a more complex magnetic field geometry can be added (Réville et al. 2016; Vidotto 2021).

A different way of generating solar wind models is to explicitly treat the energy deposition into the solar corona that heats and drives the wind. The necessity of this arises from the fact that an expanding corona treated as a mono-atomic gas with an adiabatic index of $\Gamma = 5/3$ cannot produce an accelerated solar wind and therefore requires additional energy input to prevent adiabatic cooling (Cranmer and Winebarger 2019). This can be done e.g. by including a process of converting magnetic energy into thermal energy through the dissipation of turbulence within the magnetic field (Cranmer 2010; Vidotto 2021). Compared to polytropic wind models, solar wind descriptions of this nature are computationally more expensive and are oftentimes restricted to much smaller domains, depending on the physical processes in consideration (Vidotto 2021).

1.3 Stellar Winds

In investigating the solar wind and its impact in the Solar System, the question might arise if it is reasonable to assume that other stars exhibit the same phenomenon. Parker (1958) already argued that it is probably not possible for the corona of any star to be in hydrostatic equilibrium, but rather to follow the supersonic radial expansion he described.

While more evolved stars that have moved away from the main sequence show wind phenomena characterized through different mechanisms and parameters, by now it is rather well established that solar-like stars show a radial mass flow similar to the Sun (Vidotto 2021), which exhibits a rather weak mass loss rate on the order of $2 \times 10^{-14}\,\mathrm{M_\odot\,yr^{-1}}$ (Wood et al. 2021). Model descriptions that accurately reflect the solar wind can therefore be used to gather information about the stellar winds of solar-like stars, and by extension draw conclusions about the conditions these produce for their environment and potentially planets in orbit around them (e.g. Cohen et al. 2014). Studying the variation in wind parameters gathered from stars that are similar to the Sun, but show large variation in age, can also help in building a picture about the mass flow evolution, and therefore the stellar evolution in general, of solar-like stars (Réville et al. 2016).

1.3.1 Detection

If the phenomenon of the solar wind is extended to sun-like stars, it would be preferable to challenge existing stellar wind models through direct observations of their parameters in extrasolar systems. However, *in situ* measurements are not possible in these cases and following the nature of their solar counterpart, these stellar winds are very weak. Through these difficulties, researchers have to find ways of characterizing and tracing stellar mass flows through a variety of different identifiers.

Ly-α absorption:

As the solar wind meets and interacts with the ISM, it forms a bubble around the Solar System called the heliosphere: Solar wind particles are decelerated, and through the relative motion of the heliosphere in the ISM, a wall of neutral hydrogen is formed - a stellar wind emanating from a solar-like star will form a similar structure called an astrosphere (Wood 2004).

Observing the Ly-α flux from a star will show modulations in the emission line profile based on the different "obstacles" encountered in its journey to the Solar System. One of these obstacles is the hydrogen wall formed outside an astrosphere, and so careful reconstructions and analyses of Ly-α profiles can be used to indirectly infer stellar mass loss rates and through this constraints on stellar wind parameters (Wood 2004). A caveat of this technique is that it cannot reliably be used to estimate upper limits on mass loss rates: non-detection of the Ly-α signature could imply a very low mass loss rate, but it could also be a result of ISM influences that do not provide information on the stellar wind in question (Vidotto 2021; Wood 2004). Using the Ly-α signature is nevertheless the most prolific method of measuring stellar wind mass loss rates to date (Wood et al. 2021).

Radio free-free emission:

As mentioned above, a drawback of using Ly-α observations to characterize stellar winds is that a non-detection cannot be used to reliably put upper limits on wind mass loss rates. As a fully ionized plasma, a stellar wind emits free-free radiation (bremsstrahlung), most notably in the radio regime for the densest regions of the wind (Vidotto 2021). Fichtinger et al. (2017) used radio observations to estimate the mass loss rates of a sample of four young solar analogues, based on the expected flux spectrum. To date, no winds have directly been detected using this method, although the absence of such continuum radiation can be used to infer upper limits on mass loss rates for stellar winds (Fichtinger et al. 2017; Wood et al. 2021).

While these are two prominent methods implemented in constraining the mass loss and by extension stellar wind parameters in extrasolar systems, there are variety of other techniques that can be used to further characterize and validate measurements. These include (a) probing the atmospheric escape of very close-in planets experiencing conditions unprecedented in the Solar System; (b) measuring slingshot prominences for rapidly rotating stars, which are fed by mass upflows from the stellar wind; and (c) placing upper limits on wind parameters by attributing a part of the total stellar X-ray luminosity to the free-free emission potentially coming from the hot wind (see Vidotto (2021) and references therein). These and other proposed methods to probe stellar winds can be combined to investigate the wind parameters for large samples of stars, providing an extensive picture for the evolution of solar-like stellar winds (Vidotto 2021; Wood et al. 2021), although the lack of direct comparability between these methods still proves to be a hindrance in the overall investigation of global stellar wind parameters.

An interesting aspect of this is the topic of a *wind dividing line*: as presented by Wood et al. (2014), a relation between the mass loss rate $\dot{M}$ and the X-ray surface flux F_X of stars with established wind detection breaks down for values of $F_X > 1 \times 10^6\,\mathrm{erg\,s^{-1}\,cm^{-2}}$. Below this threshold, the mass loss rate increases together with F_X, an indicator of stellar magnetic activity, and after this boundary $\dot{M}$ falls significantly below the established relation. Fig. 1.4 illustrates wind measurements of solar-like stars using the Ly-α method, indicating the existence of wind dividing line with significantly weaker winds above $\log F_X = 6$ (Wood 2018). The evidence for this is centered around π^1UMa, which shows a significantly weaker mass loss rate as suggested by the relation described above. Newer data presented by Wood et al. (2021), including wind measurements for G, K and M dwarfs, weakens the previous evidence for this wind dividing line and suggests a $\dot{M} - F_X$ relation with larger scatter. Observational based investigations and predictions from theoretical models provide complementary methods of describing the behaviour of stellar winds, but the low number of solar-like stars with stellar wind observations still provides large uncertainties in global constraints of this phenomenon.

1.3.2 Stellar Evolution

Understanding the connection between the evolutionary sequences of stellar rotation rate, magnetic activity and wind is paramount in characterizing the behaviour of solar-like stars as they evolve. As the magnetized wind carries away mass from its source, it transfers angular momentum and slows down the rotation (Réville et al. 2015). The connection between the rotation rate and magnetic activity (Vidotto et al. 2014a), as well as the role of the magnetic field as a driving force in the acceleration of the solar wind (Cranmer

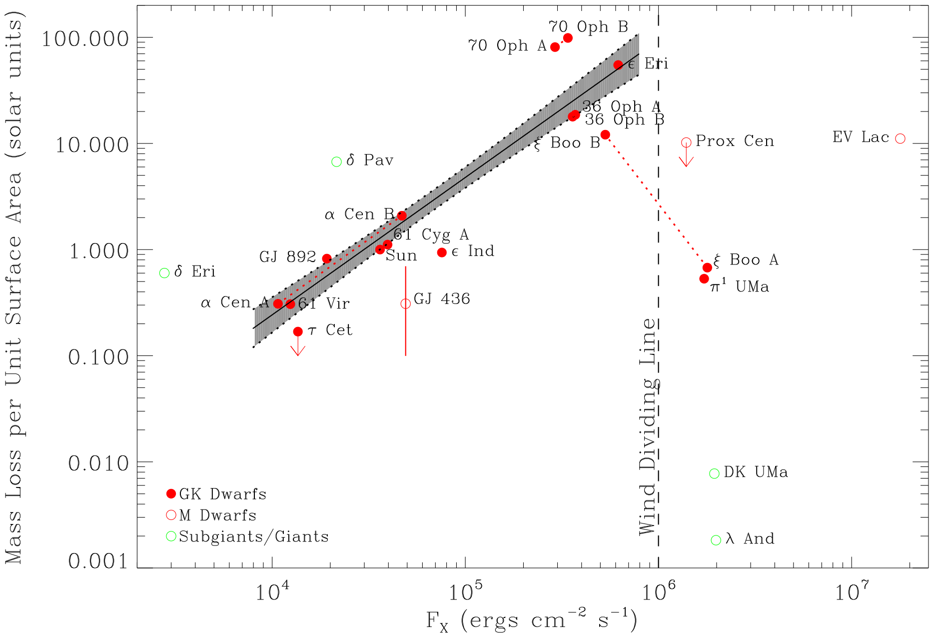

Figure 1.4: Mass-loss rates per unit surface area of low-mass stars in relation to X-ray surface flux F_X. Values are derived from Ly-α absorption fitting. For GK dwarfs (filled red circles), a power law $\dot{M} \propto F_X^{1.29\pm0.16}$ is fitted (shaded area), but this relation seems to break down at $F_X > 1 \times 10^6\,\mathrm{erg\,s^{-1}\,cm^{-2}}$, suggesting the existence of a "wind dividing line". The outliers above this threshold are π^1UMa and the binary ξ Boo A, both showing significantly lower mass loss rates for high F_X values. Newer mass-loss measurements including a larger sample of stars weaken the evidence for this threshold, instead suggesting a less steep power law $\dot{M} \propto F_X^{0.77}$ with a larger scatter. Figure from Wood (2018), reproduced under the Creative Commons Attribution 3.0 license.

and Winebarger 2019; Vidotto 2021), show that these parameters form a feedback loop, decreasing together throughout the main sequence lifetime of a solar-type star.

When extending solar wind descriptions into the bigger picture of stellar winds, investigations into the behaviour of mass loss rates and the connected loss in angular momentum for a variety of solar-like stars therefore present the possibility of deriving scaling relations between major stellar parameters that evolve during the stars lifetime: Matt et al. (2012) presented a stellar wind torque formulation based on the magnetic field strength and stellar rotation rate, using a polytropic wind model; Cohen and Drake (2014) extended this by deriving a similar relation between the stellar mass loss rate and key parameters influenced during stellar evolution such as magnetic field strength and rotation period, as well as stellar base density, but using an explicit way of driving the solar wind through a source term in the energy equation; Ahuir et al. (2020) provided a system of scaling relations for all relevant parameters connected to the spin-down description of solar-like stars.

These magnetic breaking formalisms can be used to reproduce the observational trends established for stellar populations. Gallet and Bouvier (2015) investigated the rotation rate distribution for solar-mass stars with respect to age: the authors illustrated that the large spread of Ω_* for younger, solar-like stars converges towards an age-rotation relation close to $\Omega_* \propto t^{-1/2}$ (Skumanich's law). In investigations concerned with the habitability of stellar systems, the evolutionary processes influencing stellar wind parameters are important in characterizing the environments generated for planets in these systems. Exemplary for this, Lichtenegger et al. (2010) discussed the fact that stronger winds in a younger solar system contribute towards changes in the treatment of atmospheric erosion processes connected to the protection provided by planetary magnetic fields from non-thermal loss processes.

In this work, I have used and modified the general 3D MHD code `NIRVANA` in order to generate a model description of the solar wind. This consists of two parts: gathering and evaluating measurement data taken by the PSP and SolO to find solar wind parameters over a large range of heliocentric distances, as well as, for the first time, using `NIRVANA` to create a model for the solar wind on the basis of implementing an Alfvén wave driven heating mechanism. In Chapter 2, current measurements of solar wind parameters through PSP and SolO are described, which can be used as empirical constraints for solar wind models. Chapter 3 describes the MHD code `NIRVANA` used in this work, as well as the modifications implement in order to facilitate the inclusion of a wave-turbulence driven (WTD) heating mechanism as a driving force of the solar wind. Finally, Chapter 4 describes the results obtained with `NIRVANA`, together with the limitations and problems encountered throughout the development of the model. Chapter 5 provides concluding remarks and an outlook on the topic and work presented here.

Chapter 2

Observational Data

In order to generate an appropriate solar wind model as a proxy to facilitate the study of a larger stellar sample, it is important to validate the initial results against observational data. For this purpose, the measurements obtained from two recent space missions are ideal candidates: PSP and SolO. Both missions carry a variety of scientific instruments to investigate the solar dynamo, the coronal magnetic field, the driving forces of the solar wind and other parameters in the heliosphere (Kasper et al. 2016; Müller et al. 2020). An overview of these can be found in Tab. 2.1. The measurements of these instruments are released on a semi-regular basis and provide empirical constraints for the generation of solar wind models as described in Chapter 3.

2.1 Parker Solar Probe

The Parker Solar Probe is a NASA funded space mission launched in August 2018[1] that carries a payload of four suites of scientific instruments, as listed in Tab. 2.1. Of these four, the Solar Wind Electrons, Alphas and Protons (SWEAP) investigation is of interest for this work, comprised of four instruments itself (Kasper et al. 2016):

- The Solar Probe Cup (SPC) is a Faraday Cup at the edge of the PSP heat shield, pointed in a sunward direction.
- The Solar Probe Analyzers (SPAN) are a set of three electrostatic analyzers (ESAs) taking measurements from behind the spacecrafts heat shield.

In this case, measurements from the SPC instrument are of interest due to its continuous observation of the solar wind from its location on the spacecraft: the ESAs of the SPAN suite are blocked from directly observing the plasma flow by the heat shield most of the time, and SPC is designed to fill this gap (Case et al. 2020; Kasper et al. 2016).

[1] *Parker Solar Probe: Humanity's First Visit to a Star*.

Table 2.1: Instruments carried by PSP and SolO. Both missions have similar goals in investigating the solar dynamo, the acceleration of the solar wind and the heliospheric plasma environment among other objectives (Kasper et al. 2016; Müller et al. 2020). The instruments on board the SolO spacecraft listed here only include *in situ* instruments - SolO also carries six remote-sensing instruments that provide complementary observations of the Sun and its surroundings through a suite of telescopes (Müller et al. 2020).

	Parker Solar Probe [1]
FIELDS	Measuring the shape of the electric and magnetic field throughout the heliosphere
WISPR	Imaging instrument observing large scale structures in the corona before they reach the spacecraft
SWEAP	Measuring density, velocity and temperature of the most prominent solar wind constituents (electron, protons, alphas)
IS⊙IS	Detecting solar energetic particles and high-energy solar wind particles outside the range of SWEAP
	Solar Orbiter [2]
EDP	Measuring energetic particles originating from the Sun over a large range of energies
MAG	Determining the strength and direction of the solar magnetic field
SWA	Observing key parameters of the bulk solar wind species, such as density, velocity and temperature
RPW	Measuring changes in the magnetic and electric field around the spacecraft

[1] *Parker Solar Probe Instruments*
[2] *Solar Orbiter Instruments*

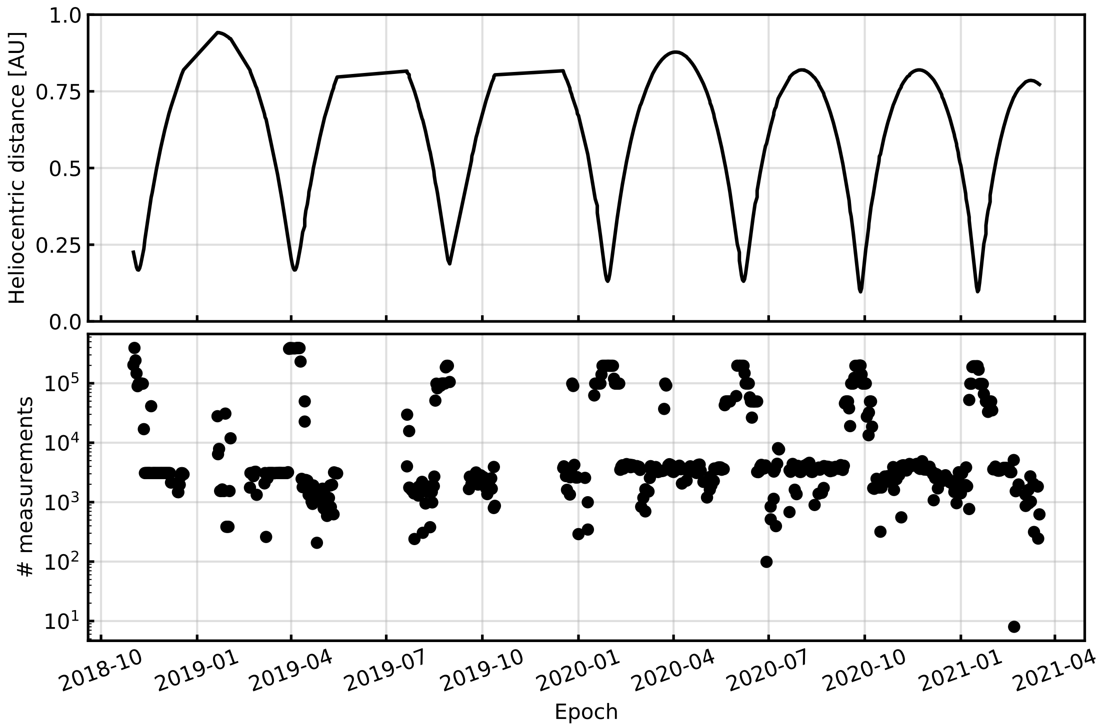

Figure 2.1: Comparison between the heliocentric distance of PSP and the total number of measurements points from SPC between October, 2018 and March, 2021, representing the total range of available data. (*Upper panel*) Heliocentric distance of the spacecraft in AU with respect to time. Seven perihelia can be seen in this time period, progressively moving closer to the Sun. The current closest perihelion sits at $20.72\,\mathrm{R}_{\odot}$. (*Lower panel*) Total number of measurement points provided with respect to time. It is rather visible in this panel that the number of measurements taken increases by about two orders of magnitude when the spacecraft enters the distance regime labelled *encounter* (less than $0.25\,\mathrm{AU}$). Comparison between the top and bottom panel shows that SPC measurements are not available during periods of time mostly centred around large heliocentric distances.

Case et al. (2020) describe the operational principle of SPC: the instrument operates through the selection of particles based on their energy-to-charge ratio (E/q) by a modulating high-voltage (HV) grid. Non-repelled particles induce an AC signal on a collector plate, which makes up the raw data acquired from SPC.

In general, the orbit of PSP is divided into two regimes: *cruise* (at heliocentric distances beyond $0.25\,\mathrm{AU}$) and *encounter* (at heliocentric distances of less than $0.25\,\mathrm{AU}$). During the cruise phase of an orbit, SPC (and in general the other instruments as part of the payload as well) operate more sporadically due to e.g. restrictions in power and operational use while data transfer is in progress, while measurement cadence is increased significantly during the encounter phase, when the spacecraft is in a region of increased scientific interest (Case et al. 2020). An illustration of this is provided in Fig. 2.1, comparing both the heliocentric distance of PSP and the total number of measurements taken by the SPC instrument with respect to the epoch, spanning the whole range of available measurements.

Data processing reduces the raw information sent by the instrument to Level-2 and Level-3 science data products. Level-2 data includes current spectra (meaning the measured current for a set of energy-per-charge windows) for each measurement window as well as a differential energy flux as total current per measurement area (Case et al. 2020), which are further refined in Level-3 data products. In these, the solar wind plasma properties are calculated both through fits of Maxwellian distributions to the current spectra, as well as through moment calculations of a reduced velocity distribution function (RDF) gained from the differential energy flux (Case et al. 2020). These properties include the proton density, velocity vector and temperature based on the thermal speed as displayed in Eq. 2.1, where T corresponds to the temperature and m to the mass of the particle.

$$v_{\text{th}} = \sqrt{\frac{2k_B T}{m}} \tag{2.1}$$

SPC supplies the measurements for the velocity, density and temperature with respect to both the spacecraft frame (SC) and an inertial *Radial-Tangential-Normal* frame (RTN) in heliocentric inertial coordinates (HIC). The latter are in reference to the solar equatorial plane and can therefore be used to place the measurements both with respect to heliocentric distance, as well as heliolatitude. The velocities reported in this frame have already been corrected for the variable motion of the spacecraft, depending on the distance. Fig. 2.2 illustrates an exemplary orbital trajectory for PSP, ranging from August 22nd, 2020 to January 11th, 2021 and covering the time period designated as encounter 6 through the SPC data release.

2.2 Solar Orbiter

Solar Orbiter is a space mission lead by ESA. It launched in February 2020 and carries a diverse payload of ten scientific instruments (Müller et al. 2020). Of interest for this work are the measurements from the Solar Wind Analyzer (SWA), a suite of instruments very similar in their goals to the SWEAP suite onboard PSP. The SWA instruments include:

- The Electrostatic Analyzer System (SWA-EAS), a high-cadence sensor measuring solar wind electrons.
- The Heavy Ion Sensor (SWA-HIS), a sensor for the heavy ion composition and kinetic properties of the solar wind.
- The Proton-Alpha System (SWA-PAS), a sensor measuring the solar wind protons and alphas.

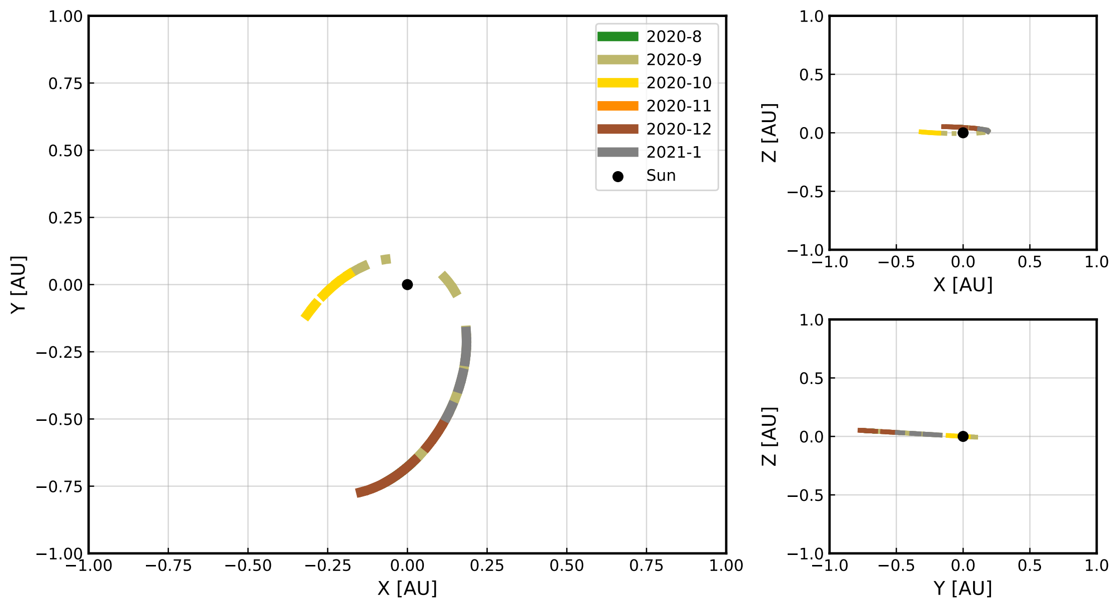

Figure 2.2: PSP positional data between August, 2020 and January, 2021, designated as encounter 6. The three panels illustrate planar cuts in the HIC system, where the xy-plane corresponds to the solar equatorial plane, and the z-axis is aligned with the solar rotational axis. Data points are separated by colour into the respective months of observation. Notable features of the trajectory include overlap in the positional space, as the designated encounter duration does not coincide with a trajectory between perihelion and aphelion, as well as an absence of large measurement stretches centred around November, 2020, where data evaluation excluded these measurements.

In the science case here, measurements from the SWA-PAS are of specific interest. Its technical specifications are illustrated by Owen et al. (2020): similar to SPC, described in Section 2.1, the instrument is mounted facing in a sunward direction, sitting behind a cut-out in the heat shield of the spacecraft. It consists of an electrostatic analyzer (ESA) element and eleven channel electron multipliers (CEMs), which allows the generation of a 3D VDF with a cadence of $4\,\mathrm{s}$.

SWA measurements are further reduced to produce data intended for use in the scientific community: As described by Case et al. (2020), Level-2 data products specifically include solar wind parameters of interest in the form of ground-calculated 3D VDF moments representing density, bulk velocity and temperature of the proton and alpha particle component. Measurements are provided in both the spacecraft frame of reference and with respect to the RTN frame of reference. In order to place these parameters along the trajectory of SolO, auxiliary data for the spacecraft orbit and altitude can be found in e.g. the SPICE kernel data set for the mission, which is further described in Section 2.3.

Solar Orbiter will enter its nominal science orbit after an Earth gravity-assisted manoeuvre in November 2021 (Müller et al. 2020), but has provided measurements from its *in situ* instruments during the cruise phase of the mission. Fig. 2.3 illustrates the orbital position of SolO corresponding to the available data release.

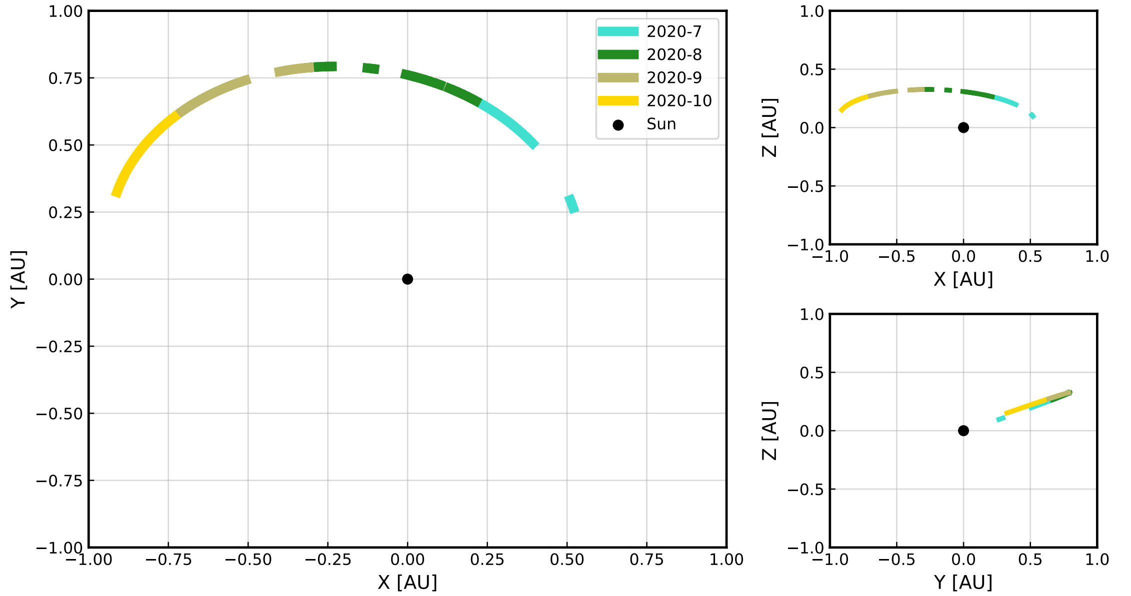

Figure 2.3: Solar Orbiter positional data between July, 2020 and October, 2020, as provided by the SPICE kernel. The three panels illustrate planar cuts in the HIC system, where the xy-plane corresponds to the solar equatorial plane, and the z-axis is aligned with the solar rotational axis. Data points are separated by colour into the respective months of observation, located between the first perihelion of the space craft in June, 2020 and a the first Venus gravity-assisted manoeuvre in December, 2020.

2.3 Data Analysis

SPC data availability ranges between October, 2018 and March, 2021 (as of October, 2021) and encompasses seven encounters, with the closest approach reaching $20.72\,\mathrm{R}_\odot$, or 9.64×10^{-2} AU. SWA data has been published between the dates of July, 2020 and October, 2020. This time frame represents part of the cruise phase for SolO, covering an increasing heliocentric distance from 0.591 AU between its first perihelion in June, 2020 and the first Venus gravity-assisted manoeuvre in December, 2020 (Müller et al. 2020). Both PSP and SolO supply their public data in the form of *Common Data Format* (CDF) files on a semi-regular basis[2][3]. I have implemented general data handling using `pycdf`, a Python interface for the CDF library.

Parker Solar Probe Data:

From the measurements provided from the SPC instrument, I have used the Level-3 data product corresponding to processed science data. I have evaluated the data quality of the available SPC measurements based on (1) excluding fill measurement points where a specified value x is set to -1×10^{-31} and (2) the `general_flag` connected to each data

[2] *Data - The Solar Wind Electrons, Alphas and Protons (SWEAP)*.
[3] *Solar Orbiter Archive*.

set, where a value other than 0 indicates conditions that are not nominal. Going through the overall data set available from the SPC instrument with these flags reduces the total amount of measurements by 48.84 % to approximately 1.0542×10^7 individual data points.

Fig. 2.4 shows an exemplary evaluation of the available SPC measurement data, coinciding with the designated time frame for encounter 6 (August 23rd, 2020 to January 11th, 2021). It displays a measurement frequency map for the three major parameter of density, velocity and temperature connected to the solar wind. The measurement data is binned with respect to distance ($\Delta v = 1 \times 10^{-3}\,\mathrm{AU}$), as well as with respect to the measured parameter as shown in the figure. In order to provide better comparability between the results of solar wind simulations and the measurements taken by SPC, Fig. 2.5 illustrates the same reduced data set in the form of a median evaluation to reduce the influence of outlier measurement points, overplotted on the actual data set.

Two parameters of specific interest in characterizations of stellar wind properties and environments are the mass loss rate and ram pressure respectively. As discussed in previous Sections, the mass loss rate is an important factor in characterizing the stellar rotational evolution through angular momentum transport. On the other hand, the ram pressure exerted by the stellar wind can significantly contribute to atmospheric escape investigations concerned with non-thermal loss processes (Lichtenegger et al. 2010). Fig. 2.6 displays the mass loss and ram pressure values related to the above described measurement time frame, together with a nominal mass loss reference value of $2 \times 10^{-14}\,\mathrm{M_\odot\,yr^{-1}}$ (Wood et al. 2021). The mass loss rate and ram pressure are calculated through Eq. 2.2 and 2.3 respectively.

$$\dot{M} = 4\pi r^2 \cdot \rho v \tag{2.2}$$

$$P_{\mathrm{ram}} = \rho v^2 \tag{2.3}$$

In these equations, ρ represents the fluid density and v the corresponding velocity. The total availability of SPC spans seven designated encounters, and data plots for these time periods can be found in Appendix B.

An obvious feature visible in all three panels of Fig. 2.4 is an apparent bimodal distribution of the displayed parameters at close distances. While this might suggest a view of the bimodal distribution expected for the two solar wind regimes, it is in fact a result of the considered data regime. When compared to Fig. 2.2, it becomes apparent that the spacecraft passes the perihelion during this encounter and therefore provides multiple measurement for smaller heliocentric distances. The visible bimodality is consequently a result of this time series and the corresponding overlapping orbit. Fig. 2.5 illustrates the large range of individual measurement points for all three parameters, spanning, in some instances, multiple orders of magnitude. Concluding from that, using measurement

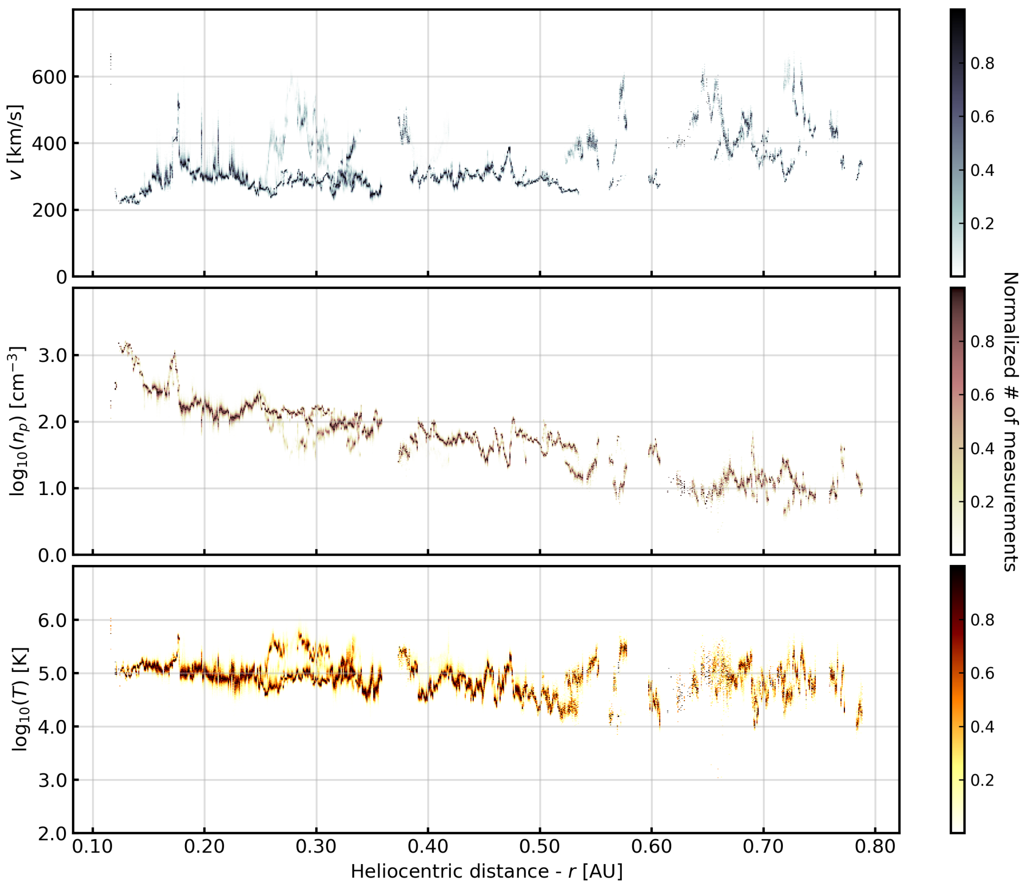

Figure 2.4: SPC measurements in a time frame between 22nd of August, 2020 and 11th of January, 2021 (encounter 6 of PSP). All three measurements are sorted into distance bins of size $\Delta r = 1 \times 10^{-3}\,\mathrm{AU}$, and color-maps indicate the normalized frequency of measured values with respect to each distance bin. (*Upper panel*) Proton velocity in $\mathrm{km\,s^{-1}}$, binned in increments of $\Delta v = 1\,\mathrm{km\,s^{-1}}$. (*Middle panel*) Logarithmic proton number density in units of $\mathrm{cm^{-3}}$, with a bin size of $\Delta \log \rho_p = 0.1$. (*Lower panel*) Logarithmic proton temperature in units of K, binned in increments of $\Delta \log T = 0.1$.

constraints derived form median values will better reflect the overall solar wind parameters by accounting for these outliers.

Solar Orbiter Data:

To relate the measured parameters of the SWA-PAS instrument to the spacecraft position in the heliosphere, I have used ancillary data provided in the SPICE kernel for this mission[4]. The SPICE toolkit, developed under the Navigation and Ancillary Information Facility (NAIF), was originally intended to provide orbital geometry parameters for NASA planetary missions, but has come to include auxiliary data for many international missions (Acton et al. 2018; Acton 1996). Using the pythonic wrapper `SpiceyPy` for the SPICE toolkit (Annex et al. 2020) has allowed me to integrate a correlation between the `EPOCH` parameter from

[4]ESA SPICE Service .

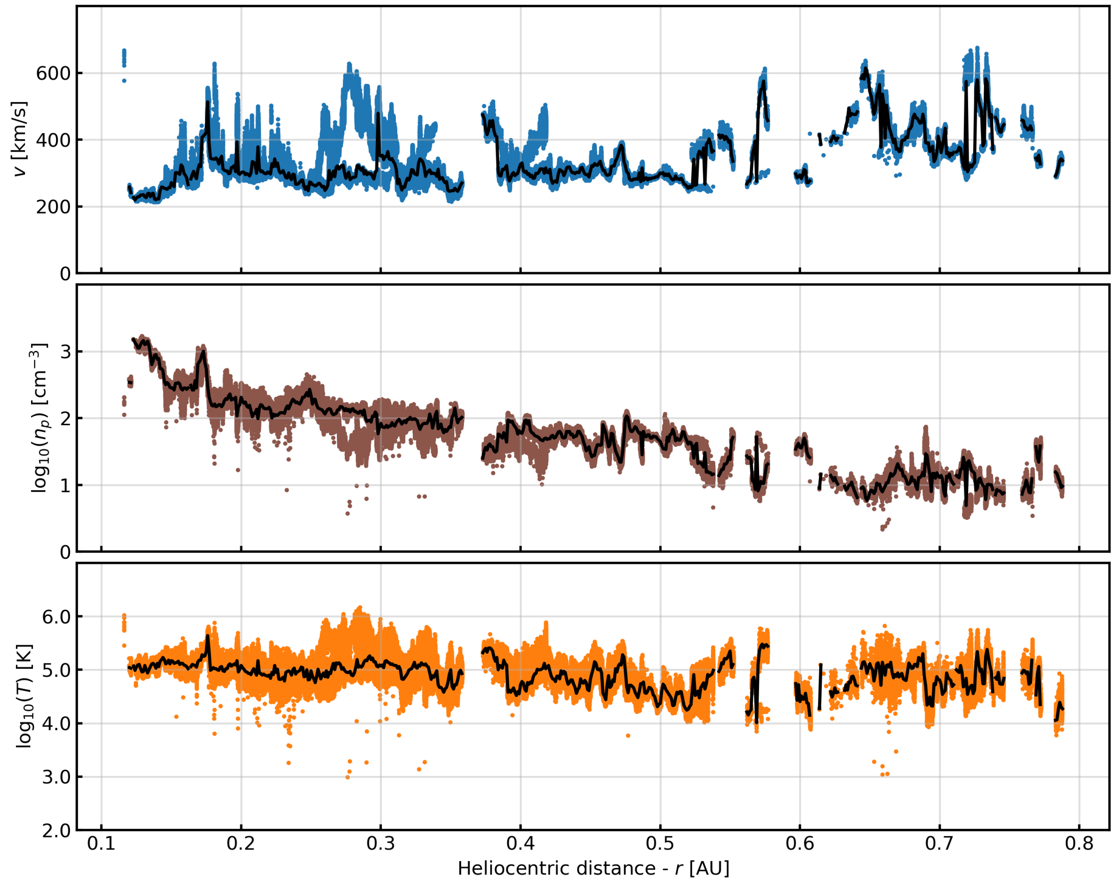

Figure 2.5: Same as Fig. 2.4, but displaying median values of the parameters in question (solid lines) over the individual data points.

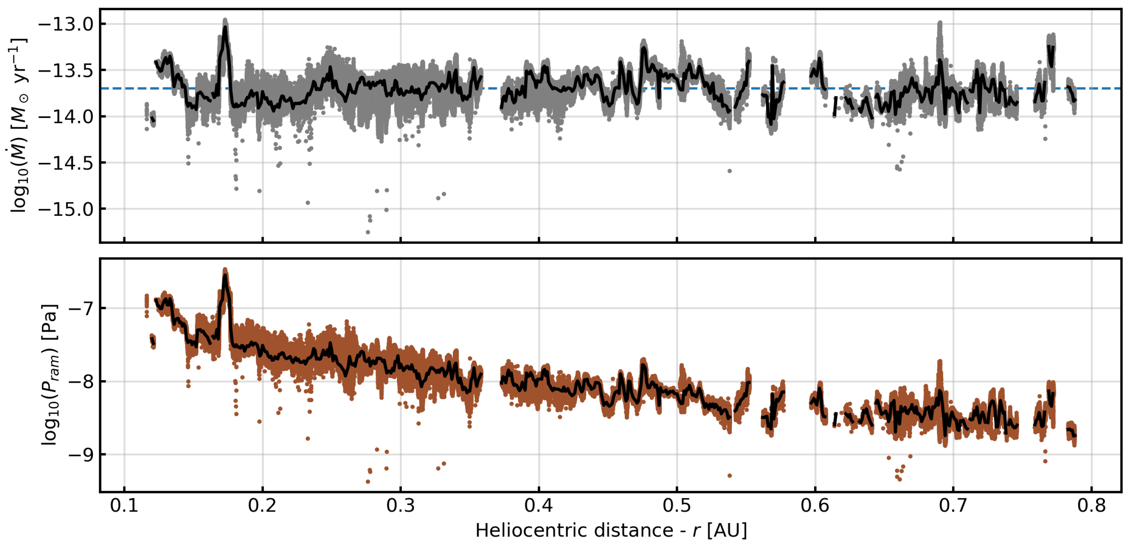

Figure 2.6: Mass loss rate in units of $\mathrm{M}_{\odot}\,\mathrm{yr}^{-1}$ (upper panel) and ram pressure in units of Pa (bottom panel) with respect to heliocentric distance in AU, resulting from the measurements of SPC. Mean values (solid black lines) are overplotted onto individual data points. The blue dashed line in the upper panel indicates a reference value of $2 \times 10^{-14}\,\mathrm{M}_{\odot}\,\mathrm{yr}^{-1}$ (Wood et al. 2021).

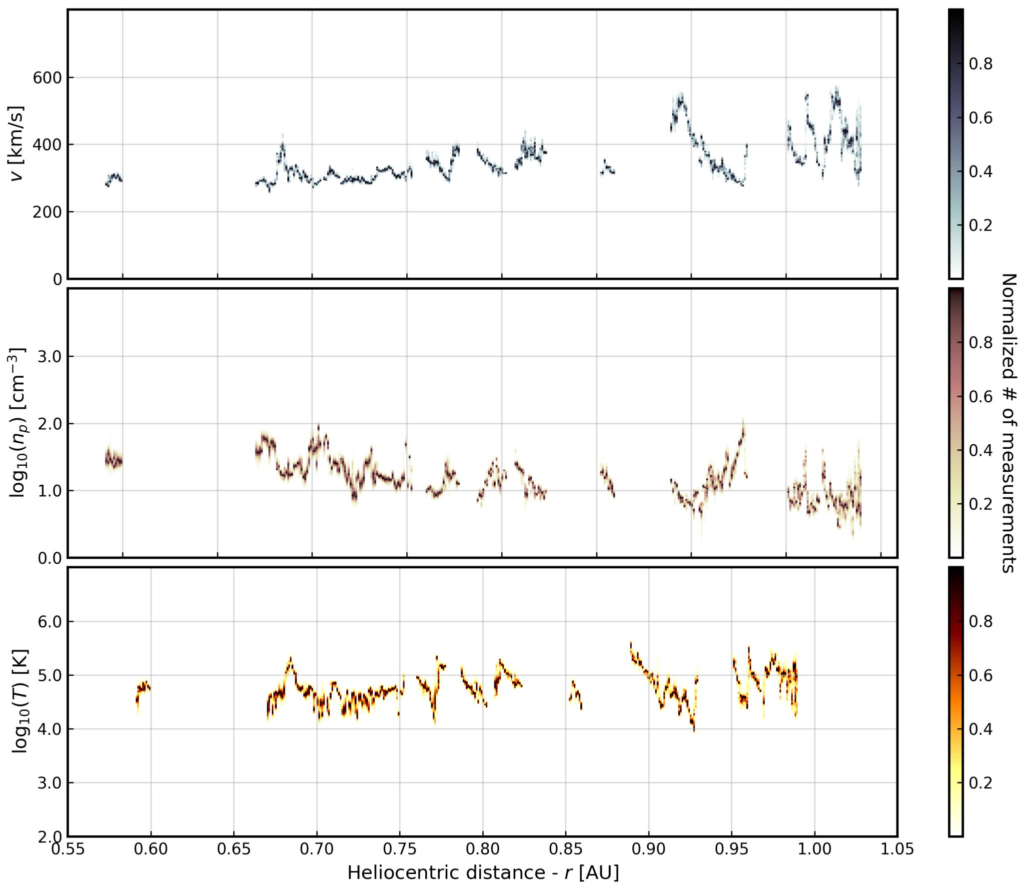

Figure 2.7: SWA-PAS measurement data between July 6th, 2020 and October 28th, 2020. All three measurements are sorted into distance bins of size $\Delta r = 1 \times 10^{-3}$ AU, and color-maps indicate the normalized frequency of measured values with respect to each distance bin. (*Upper panel*) Proton velocity in $\mathrm{km\,s^{-1}}$, binned in increments of $\Delta v = 1\,\mathrm{km\,s^{-1}}$. (*Middle panel*) Logarithmic proton number density in units of $\mathrm{cm^{-3}}$, with a bin size of $\Delta \log \rho_p = 0.1$. (*Lower panel*) Logarithmic proton temperature in units of K, binned in increments of $\Delta \log T = 0.1$.

the SWA-PAS measurement data and the spacecraft position into the evaluation routine of the data set.

For data analysis, I have used the Level-2 data product representing reduced science data. Similar to the evaluation routine for the SPC data, I have reduced the SWA-PAS measurements based on a data validity flag (only including measurements with a flag value of 3, where 1 and 2 represent non-ideal conditions). As pointed out previously, SolO has not entered its science orbit, but has provided a window of *in situ* measurements between October and December, 2020. Fig. 2.7 and 2.8 show the evaluation of the available SWA-PAS data set in form of a measurement frequency map and median values respectively (complementary to Fig. 2.4 and 2.5), spanning heliocentric distances between approximately 0.6 and 1.0 AU. Fig. 2.9 displays the mass loss rate and ram pressure as a result from the measured data, comparable to Fig. 2.6.

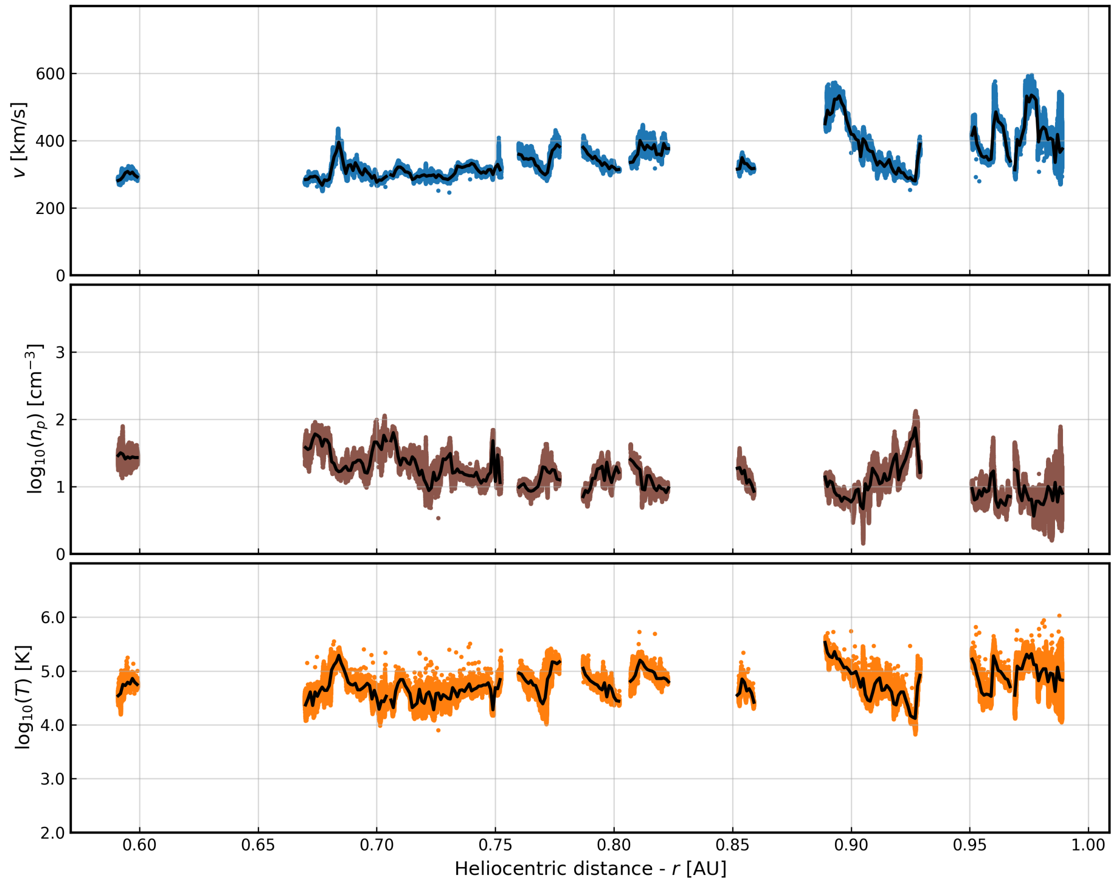

Figure 2.8: Same as Fig. 2.7, but displaying the corresponding median values, overplotted on individual data points.

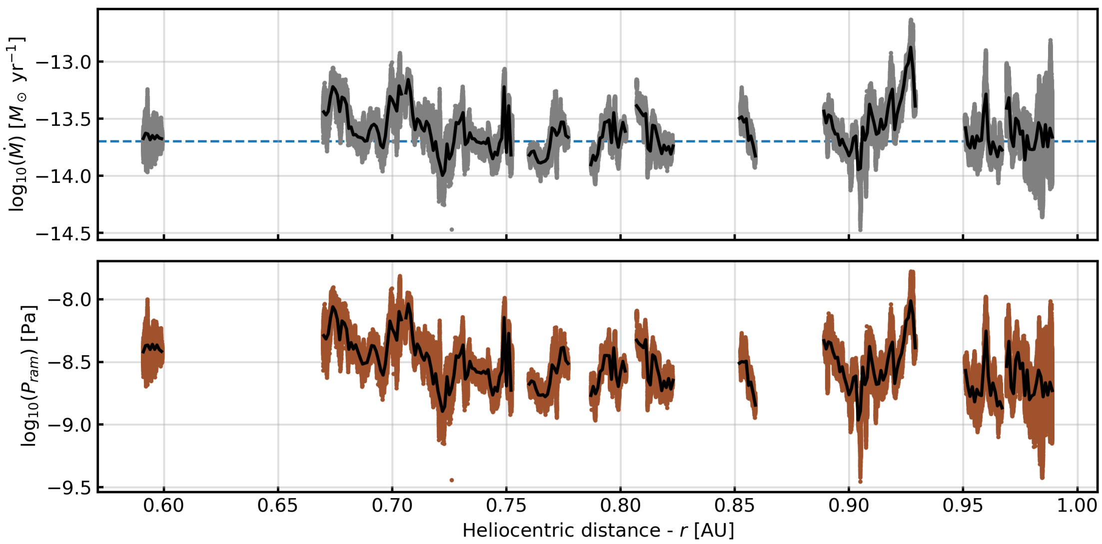

Figure 2.9: Mass loss rate in units of $\mathrm{M}_{\odot}\,\mathrm{yr}^{-1}$ with respect to heliocentric distance in AU, resulting from the measurements of SWA-PAS. Mean values (solid black lines) are overplotted onto individual data points (grey). The blue dashed line indicates a reference value of $2 \times 10^{-14}\,\mathrm{M}_{\odot}\,\mathrm{yr}^{-1}$ (Wood et al. 2021).

Chapter 3

A Numerical Model

This work uses a generalized, three dimensional MHD code called NIRVANA (Ziegler 2008) to create a model of the solar wind based on an explicit, wave-turbulence driven heating mechanism (Cranmer 2010). This model can be compared to observational data gathered from the *Parker Solar Probe* and *Solar Orbiter*. Creating a solar wind description consistent with empirical data presents a way of studying the properties of generalized stellar winds by varying the appropriate input parameters in congruence with a sample of solar-like stars.

3.1 NIRVANA

NIRVANA is a grid-based C-code solving, in its full complexity, the time-dependent equations of a gas-dynamical system including non-relativistic, compressible magnetohydrodynamics, dissipative processes, ambipolar diffusion, self-gravity, and source terms in force and energy (Ziegler 2008). It supports Cartesian, cylindrical and spherical geometries in 2D and 3D, adaptive mesh refinement (AMR), as well as serial or parallel operation.

For the application in this work, NIRVANA solves the non-dissipative equations of magnetohydrodynamics with source terms in force and energy:

$$\frac{\partial \rho}{\partial t} + \nabla\left(\vec{m}\right) = 0 \tag{3.1}$$

$$\frac{\partial \vec{m}}{\partial t} + \nabla\left[\vec{m}\vec{v} + p_{tot}\cdot I - \frac{\vec{B}\vec{B}}{\mu}\right] = \rho\vec{f}_e + \vec{f}_C \tag{3.2}$$

$$\frac{\partial e}{\partial t} + \nabla\left[\left(e + p_{tot}\right)\vec{v} - \frac{\left(\vec{v}\vec{B}\right)\vec{B}}{\mu}\right] = \left(\rho\vec{f}_e + \vec{f}_C\right)\vec{v} + \mathcal{L} \tag{3.3}$$

$$\frac{\partial \vec{B}}{\partial t} - \nabla\times\left(\vec{v}\times\vec{B}\right) = 0 \tag{3.4}$$

In these equations, $\mu = 4\pi \times 10^{-7}\,\mathrm{V\,s\,A^{-1}\,m^{-1}}$ represents the magnetic vacuum permeability. There are eight primary variables in this set of equations: the fluid mass density ρ, the momentum density $\vec{m} = \rho\vec{v}$ (where $\vec{v}$ is the fluid velocity), the magnetic field $\vec{B}$ and the total energy density e, which is an abbreviation for the sum of the kinetic, thermal and magnetic energy density (shown respectively in Eq. 3.5):

$$e = \frac{\rho\vec{v}^2}{2} + \varepsilon + \frac{\vec{B}^2}{2\mu} \tag{3.5}$$

The variable p_{tot} appearing in Eq. 3.2 and 3.3 represent the total pressure given by the sum of the gas pressure and the magnetic pressure:

$$p_{tot} = p + \frac{|\vec{B}|^2}{2\mu} \tag{3.6}$$

Eq. 3.1 - 3.2 therefore represent the single-fluid MHD equations with additional source terms in force (set by the terms $\vec{f_e}$ and $\vec{f_c}$) and energy (represented by the term $\mathcal{L}$).

3.2 Simulation Setup

The simulations in this work use a three-dimensional, spherical domain with the coordinates (r, θ, ϕ) representing the distance from the origin of the domain, the polar angle and the azimuth angle respectively. NIRVANA provides the possibility for both initial mesh refinement (IMR), as well as AMR, allowing a non-uniform mesh-generation with smaller radial cell sizes closer to the origin of the domain. The implementation of these mesh refinement mechanisms has conflicted with the generation of appropriate results for the simulations, which is why they haven been omitted in this work. In a similar manner, NIRVANA allows the inclusion of a fully three dimensional domain, but for the simulations here this has been reduced to a single hemisphere. The reasoning for both of these restrictions is more extensively described in Chapter 4. This means that the final simulation domain encompasses $[1\mathrm{R}_\odot, 1\mathrm{AU}] \times [0, \pi/2] \times [0, 2\pi]$, with $[384, 32, 64]$ grid cells respectively, resulting in a radial grid cell size of 0.557 $\mathrm{R}_\odot$. Fig. 3.1 illustrates the simulation domain.

At the azimuthal boundaries, the fluid is constrained by periodic boundary conditions. At the rotation axis of the domain ($\phi = 0$), "free" boundary conditions are implemented that naturally extend the domain through π-shifted values. The radial outer boundary is constrained by simple outflow conditions. At the inner radial boundary, the density of the plasma is held at a constant value of $1 \times 10^8\,\mathrm{cm}^{-3}$, representative of the upper solar atmosphere (see Cranmer (2009) and references therein). The momentum density is set to 0, the magnetic field is anchored through a constant, purely radial component and the

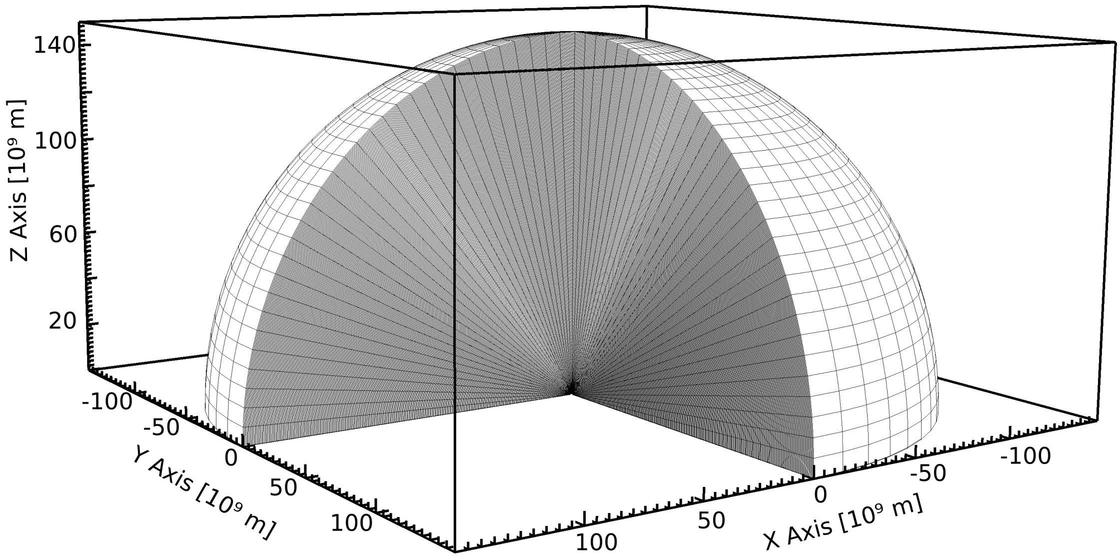

Figure 3.1: Final mesh decomposition as a hemisphere with dimensions $[1R_\odot, 1AU] \times [0, \pi/2] \times [0, 2\pi]$ and grid cell numbers $[384, 32, 64]$ for the radial, polar and azimuthal direction respectively. Restrictions in the application of NIRVANA have limited the domain decomposition both with respect to a non-uniform grid through IMR and the extension to a fully spherical domain in the polar direction. These restrictions are further elaborated on in Chapter 4.

energy density uses a zero-gradient condition.

The density grid values are introduced through a simple step function from the inner boundary value and a step size of 7 orders of magnitude, reflecting an ambient density value. The magnetic field is implemented through $B_r = B_0 \cdot (R_\odot/r)^2$ as a purely radial field following , where B_0 represents a surface field strength value, with a nominal value of $B_0 = 3\,\mathrm{G}$ corresponding to the solar magnetic field (Johnstone et al. 2015a).

Equation of state:

The simulation uses an adiabatic equation of state to connect the pressure and temperature to the other primary variables of the system through the kinetic energy density ε, which is calculated through rearranging Eq. 3.5:

$$p = (\gamma - 1)\,\varepsilon \tag{3.7}$$

$$T = (\gamma - 1)\,\varepsilon \cdot \frac{\bar{\mu} m_u}{k_B \rho} \tag{3.8}$$

$\bar{\mu}$ represents the mean molecular weight, $m_u = 1.660\,57 \times 10^{-27}\,\mathrm{kg}$ the atomic mass unit and $k_B = 1.3806 \times 10^{-23}\,\mathrm{J\,K^{-1}}$ the Boltzmann constant. The adiabatic index $\gamma = 5/3$ is chosen to reflect a mono-atomic gas.

Sources of force:

The parameter $\vec{f_e}$ in Eq. 3.2 and 3.3 represents an external force term specified as a cell-centred, mass-normalized quantity. It is defined as the gravitational force of the Sun acting upon the plasma from the centre of the domain, given in spherical coordinates by:

$$\vec{f_e} = -\frac{GM_\odot}{|\,\vec{r}\,|^3} \cdot \vec{r} \tag{3.9}$$

where $G = 6.673 \times 10^{-11}\,\mathrm{m}^3\,\mathrm{kg}^{-1}\,\mathrm{s}^{-2}$ represents the gravitational constant and $M_\odot = 1.99 \times 10^{30}\,\mathrm{kg}$ the mass of the Sun.

In a similar manner, $\vec{f_C}$ is a force source term describing the effects of a rotating frame of reference. It introduces effects based on the rotation rate of the Sun (based on the average rotation period of the Sun of $P = 28\,\mathrm{d}$, $\omega_0 = 2.597 \times 10^{-6}\,\mathrm{rad\,s}^{-1}$), manifesting in a Coriolis and a centrifugal force term.

$$\vec{f_C} = \underbrace{-2\rho\vec{\Omega} \times \vec{v}}_{\text{coriolis}} \underbrace{-\rho\vec{\Omega} \times (\vec{\Omega} \times \vec{r})}_{\text{centrifugal}} \tag{3.10}$$

The vectors $\vec{r}$ and $\vec{v}$ represent the position and velocity in the rotating frame of reference respectively. In spherical coordinates, the angular velocity vector $\vec{\Omega} = (\omega_0, 0, 0)$ represents the rotation around the geometric axis and only consists of its first entry:

3.3 WTD Heating Source Term

This model of the solar wind makes use of a wave-turbulence driven heating mechanism described by Cranmer (2010). It is based on the reflection and subsequent dissipation of Alfvén waves travelling as perturbations along magnetic flux tubes. The local turbulent heating rate Q_p is calculated through the plasma density ρ, plasma velocity v, magnetic field strength B and heliocentric distance r as input parameters and additionally depends on the correlation length scale $L_\perp$ and Alfvén wave energy density U_A as free parameters. The author also argues for the inclusion of an efficiency factor $\mathcal{E}_{\text{turb}}$ to account for regions where the turbulent cascade might be quenched (Cranmer 2010), but due to non-significant variations in the output for the simulation configuration considered here, the efficiency factor is not included.

As described by Cranmer (2010), Alfvén waves are treated as linear, incompressible and transverse perturbations in magnetic flux tubes extending into the heliosphere. These waves are partially reflected back down towards the Sun and interact with outward propagating waves, dissipating into MHD turbulence and depositing energy in the corona leading to the generation of a turbulent heating rate Q_p. The model was developed by the author with the intention of finding appropriate approximations of the necessary parameters to implement this turbulent heating rate into global models of the heliosphere, where a direct solution to the partial differential equation might be computationally too expensive. A full derivation of the analytic background can be found in Cranmer (2010): below is an outline of the computational routine.

As mentioned above, the heating rate is characterized through the interaction and dissipation of outward propagating waves, from here on denoted by a subscript $(-)$, and reflected inward propagating waves, form here denoted by a subscript $(+)$. The perturbations in velocity $v_\perp$ and the magnetic field $B_\perp$ resulting of these waves are combined into Elsässer variables $z_\pm$:

$$z_\pm = v_\perp \pm \frac{B_\perp}{\sqrt{4\pi\rho}} \tag{3.11}$$

A reflection coefficient $\mathcal{R}$ is defined as well, comparing the amplitudes of these two waves and characterizing the reflection "efficiency":

$$\mathcal{R} = \frac{|z_+|}{|z_-|} \tag{3.12}$$

This coefficient is crucial in calculating the heating rate, since it defines the amplitude of the reflected wave. $\mathcal{R}$ depends on the Alfvén wave frequency ω_i, and Cranmer (2010) outlines a routine to calculate a radius- and frequency-dependent $\mathcal{R}$ based on the limiting cases of very low ($\mathcal{R}_{\text{zero}}$) and very high frequencies ($\mathcal{R}_\infty$):

$$\mathcal{R} = \mathcal{R}_{\text{zero}}^{1-\epsilon}\mathcal{R}_\infty^{\epsilon} \tag{3.13}$$

The bridging exponent $\epsilon = (1+\omega_0/\omega)^{-1}$ has been determined through experimentation (Cranmer 2010). The turbulent heating rate Q_p is then calculated through the spectrum-weighted Elsässer variables $Z_\pm$:

$$Q_p = \rho \cdot \frac{Z_+ Z_- (Z_+ + Z_-)}{4L_\perp} \tag{3.14}$$

The outward and inward propagating waves are related through the reflection coefficient:

$$Z_- = \sqrt{\frac{4U_A}{\rho\left(1+\langle\mathcal{R}\rangle^2\right)}} \quad \rightarrow \quad Z_+ = \langle\mathcal{R}\rangle\, Z_- \tag{3.15}$$

The free parameters $L_\perp$ and U_A in Eq. 3.14 and 3.15 respectively are described in Section 3.3.1 below. The spectrum-weighted reflection coefficient $\langle\mathcal{R}\rangle$ is calculated through a discretization into 17 frequency bins spanning almost five orders of magnitude, with weights f_i corresponding to a high-frequency dominated power spectrum for Alfvén waves from Cranmer and van Ballegooijen (2005):

$$\langle \mathcal{R} \rangle = \sum_i \mathcal{R}(\omega_i) \cdot f_i \tag{3.16}$$

The routine was provided by Cranmer (2010) in the form of a `FORTRAN 77` file. I translated this into `C` in order to incorporate into `NIRVANA`, which allows the inclusion of an energy source term (parameter $\mathcal{L}$ in Eq. 3.3) as stated above. Natively, `NIRVANA` only supports heating and cooling functions with dependencies on (local) fluid mass density ρ and temperature T values. In order to facilitate the inclusion of a more complex heating source term, the code has been additionally modified in the calculation of the heatloss time step and the heatloss solving routine.

3.3.1 Free Parameters

Both the correlation length scale $L_\perp$ and the wave energy density $U_A = \rho v_\perp^2$ are free parameters in the calculation of this heating routine.

Correlation length scale $(L_\perp)$**:**
The transverse correlation length scale $L_\perp$ characterizes the reflection of outward propagating Alfvén waves necessary to induce the turbulent cascade. The correlation length is assumed to following the scaling relation proposed by Hollweg (1986).

$$L_\perp \approx \frac{6.0}{\sqrt{B\,[\mathrm{G}]}}\ \mathrm{Mm} \tag{3.17}$$

A scaling factor of 6.0, as shown in Eq. 3.17, has been chosen as an intermediate value between 11.55 and 2.876 based on normalizations from previous reasonable results (see Cranmer (2010) and references therein).

Wave energy density (U_A)**:**
The free parameter $U_A = \rho v_\perp^2$ represents the wave energy density. It is applied in Eq. 3.18, making use of the conservation of an energy flux to magnetic field strength ratio (F/B) for dispersionless Alfvén waves (Cranmer 2010).

$$\frac{F}{B} = \frac{(v + v_A)^2\ U_A}{v_A B} = 5 \times 10^4\,\mathrm{erg\,s^{-1}\,cm^{-2}\,G^{-1}} \tag{3.18}$$

As Cranmer (2010) argued, the perpendicular velocity amplitude $v_\perp$ can be derived from emission line doppler broadening. The author presents a large range of potentially applicable values resulting in a parameter range of $F/B = 2 \times 10^4\ -\ 1 \times 10^5\,\mathrm{erg\,cm^{-2}\,s^{-1}\,G^{-1}}$

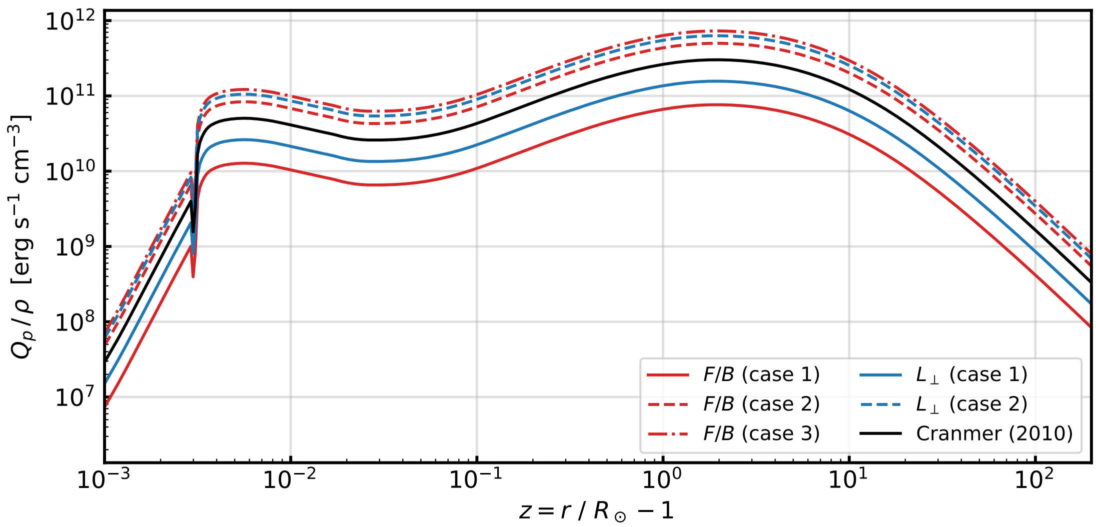

Figure 3.2: Comparison of heating routine output described in Cranmer (2010), showing volumetric heating rate with respect to heliocentric distance in reference to the solar surface. The black line denotes the exemplary input for a coronal hole regime as described by the author, with $L_\perp = 6.0/\sqrt{B\,[\mathrm{G}]}\mathrm{Mm}$ and $F/B = 5 \times 10^4\,\mathrm{erg\,s^{-1}\,cm^{-2}\,G^{-1}}$; the blue lines show a variation in the correlation length scale $L_\perp$ with a scaling factor of 11.55 (case 1) and 2.876 (case 2); the red lines illustrate a variation in the flux-over-field strength value F/B connected to the wave energy density U_A, with numerical factors of 2 (case 1), 7 (case 2) and 9 (case 3) (see Cranmer 2010, and references therein).

and assuming the intermediate value shown in Eq. 3.18.

Fig. 3.2 shows a comparison between the calculated volumetric heating rate as shown in Cranmer (2010) and a variation in both the correlation length scale and flux-to-field ratio parameter. The volumetric heating rate in units of $\mathrm{erg\,s^{-1}\,cm^{-3}}$ acts as an explicit energy contribution to the system. The calculations represented in Fig. 3.2 show Q_p/ρ with plasma parameters described by Cranmer (2010). For values of $r/R_\odot - 1 < 3 \times 10^{-3}$, the calculation routine assumes perfect wave reflection conditions ($\langle\mathcal{R}\rangle = 1$) based on density values of $\rho > 2 \times 10^{-13}\,\mathrm{g\,cm^{-3}}$. After this point, the calculation routine is executed fully, leading to the small discontinuity in form of a downward directed spike visible in the figure. Varying both free parameters modifies the global values of the heating function, while preserving the overall shape of the output.

As would be expected, reducing the flux-to-field ratio F/B and therefore the upward energy flux also reduces the volumetric heating rate (F/B, case 1), while increasing this free parameter has the opposite effect (F/B, case 2 and 3). Varying the correlation length scale has an inverse effect, where a larger value results in a reduction and smaller value in an increase of the volumetric heating rate ($L_\perp$, case 1 and case 2 respectively).

Chapter 4

Results

This chapter outlines the process of working with NIRVANA: It contains descriptions of the advancement in generating a solar wind model based on the wave-turbulence driven heating mechanism described in the previous chapter, as well as a discussion of the problems encountered in working with the combination of this specific code and the implemented heating routine. The simulations were run on computational nodes of the Vienna Scientific Cluster (VSC-4).

4.1 Initial Testing

The first step taken in order to familiarize myself with NIRVANA was to break the complex question of a solar wind model down into a more simplified version. I did this by making an effort to reproduce an isothermal, purely hydrodynamic *Parker Wind*. NIRVANA allows the choice of an isothermal equation of state, negating the necessity of solving the energy equation (Eq. 3.3). In this case, the simulation domain is increased to a full sphere, meaning a polar angle domain of $[0, \pi]$, but otherwise decomposed as stated in Section 3.2. Fig 4.1 shows the results of an isothermal wind with a temperature of $T_{\text{iso}} = 2 \times 10^6\,\text{K}$, both for the radial wind speed and the number density, as well as parameter profiles with respect to heliocentric distance. The hydrodynamic wind is highly symmetrical in both angular directions and shows no bimodal distribution with respect to heliolatitude. The distance profiles displayed in Fig. 4.1 are therefore representative of the overall wind structure. As would be expected, the solar wind profile resulting from this overestimates the velocity gradient found in observations of the solar wind, as already discussed in Section 1.1. Isothermal winds are not accurate in reflecting wind parameter measurements taken by *in situ* observations, but they serve to illustrate the transsonic behaviour expected from the global mass flow (e.g. Johnstone et al. 2015b).

Moving to a more complicated treatment of the solar wind, I extended the isothermal

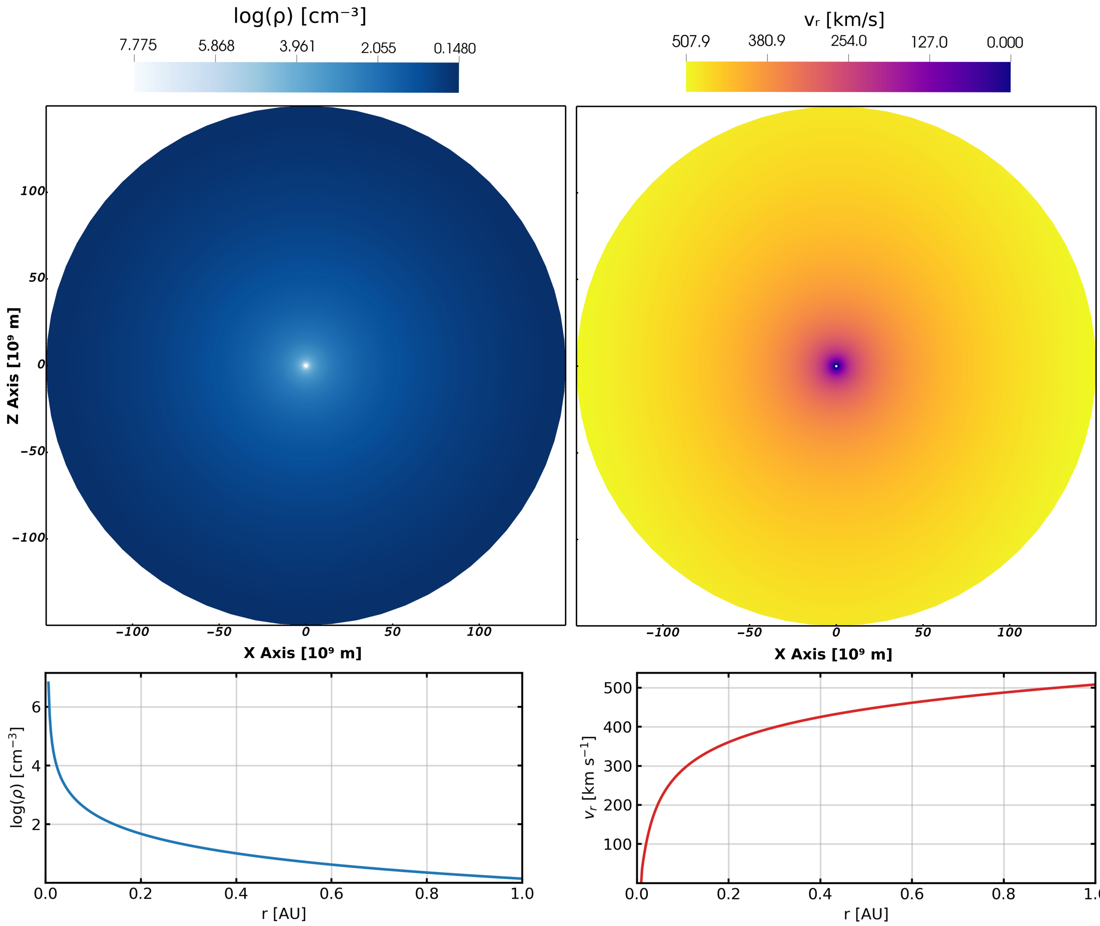

Figure 4.1: Representation of a *Parker Wind* solution generated with NIRVANA. The isothermal wind is assumed to have a temperature of $T_{\rm iso} = 2 \times 10^6\,{\rm K}$. (*Upper panels*) Polar slices (xz-plane) of the simulation domain, displaying colormaps for the number density (left, in units of ${\rm cm}^{-3}$) and radial velocity (right, in units of ${\rm km\,s^{-1}}$). As discussed in Chapter 1, the hydrodynamic, isothermal wind overestimates the velocity gradient at large distance quite significantly, but it still provides an idea on the expected behaviour of the solar wind. (*Lower panels*) Profiles of the density (left, blue line) and radial velocity (right, red line) with respect to heliocentric distance. The *Parker Wind* is highly symmetrical in both angular directions, meaning that these profiles are representative of the overall wind distribution generated by this model.

wind by introducing a magnetic field, as well as a heating source term and the connected adiabatic equation of state. For the heating processes considered in the corona, it is of interest to resolve the area close to the star as fine as possible, since most of the heating input and variation happens in this region (as can be seen in Fig. 3.2). Contrary to that, regions further out in the domain do not need to be resolved to as much of a fine degree. This means that part of the effort in translating the simplified isothermal wind setup to the more complex version included the introduction of initial mesh refinement to generate a non-uniform mesh.

This introduces one of the issues I encountered in using `NIRVANA`: IMR in this code is implemented through a subroutine when initially generating the mesh. This checks the coordinates throughout the mesh and applies a chosen refinement level based on a set of specified mathematical relations, which define distinct parts of the simulation domain. In an ideal case, this would be implemented to generate increasingly refined radial shells, which produce subsequently smaller radial grid cells. However, `NIRVANA` can only implement this refinement uniformly for all coordinate directions, meaning that the grid cell size simultaneously shrinks in both angular directions as well. Specifically, a refinement of level n means that the grid cells size shrinks in all coordinate directions by a factor of 2^n. This results in a conflict between the desired radial cell size and the unnecessary angular refinement, which significantly affects both the output size of individual simulation snapshots, as well as the simulation time step size. The latter is calculated through the Courant-Friedrichs-Lewy condition, inversely proportional to the physical size of the grid cell. As a compromise in solving this problem, the domain was not refined, but the total amount of radial grid cells was set to 384. This results in a grid cell size of 0.557 $\mathrm{R}_\odot$ in the radial direction. Fig. 4.2 shows a comparison between the iterative time step sizes for a non-refined domain, as well as for a setup with an initially lower number of radial grid cells (248) and two levels of refinement. As the figure indicates, the difference in time step size between the IMR and non-IMR cases moves around two orders of magnitude in size, with the time step size connected to the IMR case being approximately $\Delta t = 1 \times 10^{-2}\,\mathrm{s}$. Assuming a radial domain extension of $1\,\mathrm{AU}$ and a shock wave traveling at $1000\,\mathrm{km\,s^{-1}}$, the perturbation would require roughly 1.5×10^7 time steps to reach the outer boundary of the domain. The wall time for a simulation running this long is not within a reasonable range. This is the reason for the solution in domain decomposition described above, substituting the implementation of IMR in favor of an initially finer, but uniform grid.

With the introduction of a magnetized wind, a second problem emerged in the generation of the solar wind model. This concerns the behaviour of the magnetic field during the simulation. As stated in Chapter 3, the magnetic field was assumed to be a purely radial field with an inverse square dependence of the field strength. During simulations of

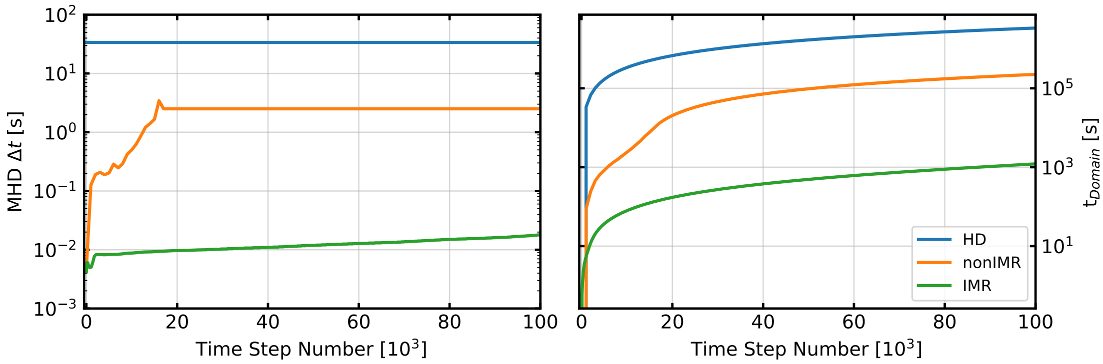

Figure 4.2: Comparison of time step sizes Δt for both a domain with implemented initial mesh refinement (green line) and a domain without IMR (orange line) for the first 10^5 time steps. In the case of no IMR, the radial domain is decomposed into 384 cells, whereas in the IMR case the mesh is initialized with 248 cells and two levels of refinement. As a comparison, the time step size for the hydrodynamic case described in the beginning of this chapter is included in this figure as well (blue line).

a fully 3D domain, encompassing a polar angle of $\phi \in [0, \pi]$, the transition region of the magnetic field polarity (which would correspond to the HCS) does not stay centered at the solar rotational equator, but breaks down and leaves an almost unipolar field instead of a pure dipole. Fig. 4.3 illustrates this for a nominal simulation, where the left and right panels show the polarity of the magnetic field within 25×10^3 and 200×10^3 time steps respectively. This problem could potentially be a result of increasingly amplified perturbations in the transition region of the magnetic field polarity not being handled properly due to a relative course grid in this region. A possible solution to this problem could be to implement a spatially restricted mesh refinement around the equatorial plane of the simulation domain, in order to better resolve and possibly handle instabilities arising in this region. However, at the current state of the model, IMR has not been implemented. Therefore, I have circumvented this problem by reducing the spherical domain to a single hemisphere, meaning $\phi \in [0, \pi]$

4.2 Final Setup

The finalized setup concerning the simulation is therefore characterized by a uniform grid extending to a three dimensional, hemispherical domain. Fig. 4.4 represents the results of a simulation run using the choices of free parameters presented in the initial setup of the WTD heating routine. The figure shows polar slices for the major wind parameters of radial velocity v_r, number density ρ and temperature T. It is apparent from this that the steady state is highly spherically symmetric: therefore, radial wind parameter profiles are representative of the global state reached at the end of the simulation. Judging the steady

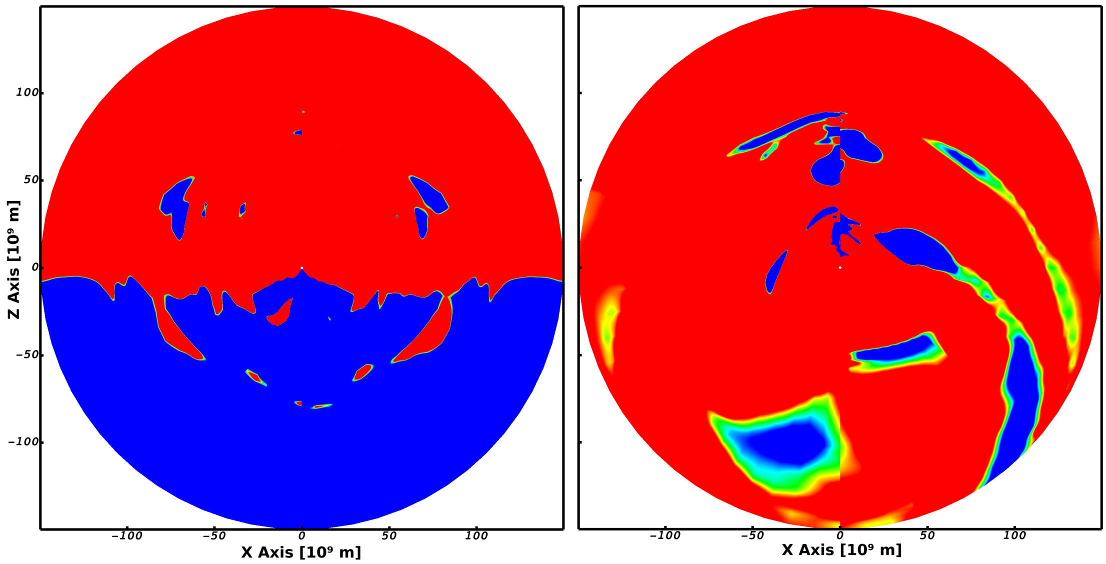

Figure 4.3: Magnetic field polarity during the simulation of a fully 3D domain, shown within 25×10^3 (left panel) and 200×10^3 (right panel) time steps. Red regions denote radially outward, and blue regions show radially inward directed field components. In this case, the domain was implemented with a uniform, non-refined grid. The panels show polar slices of the simulation domain with the z-axis denoting the direction solar rotational axis and the x-axis aligned with the solar rotational equator. In the left panel, the underlying radial dipole structure is still visible, whereas the right panel shows an almost unipolar field.

state of simulation runs can be achieved by comparing the incremental changes in plasma parameter over larger differences in domain time. Fig. 4.5 illustrates this in an exemplary case for the radial wind velocity in the case of the initially assumed free parameters, showing strong variations in the beginning of the simulation run, when perturbation waves are traveling through the domain, followed by a settling process into a steady state. The bottom panel of the figure illustrates the remaining variations in v_r for an exemplary position close to the outer boundary of the domain. These variations are derived as absolute differences between simulation states separated by $1e4$ time steps, and they are on the order of $1 \times 10^{-4}\,\mathrm{km\,s^{-1}}$, representing an acceptable state for the simulation run.

Because the overall evolution of this model strongly depends on the implemented energy source term, it is of interest to compare the specific output of the heating routine in terms of a volumetric heating rate Q_p/ρ to the initially presented behaviour as seen in Fig. 3.2, which corresponds to the input parameter range from Cranmer (2010). In Fig. 4.6, the volumetric heating rate from simulation results is displayed with variations in the free parameters $L_\perp$ and F/B. Comparing this to Fig. 3.2 illustrate key aspects in the implementation of this energy source term to the solar wind simulations. The first one to highlight is the spatial domain for both calculations: in the reference results, radial distance values start within $1 \times 10^{-3}\,\mathrm{R}_\odot$ and represent a much finer radial resolution outwards to

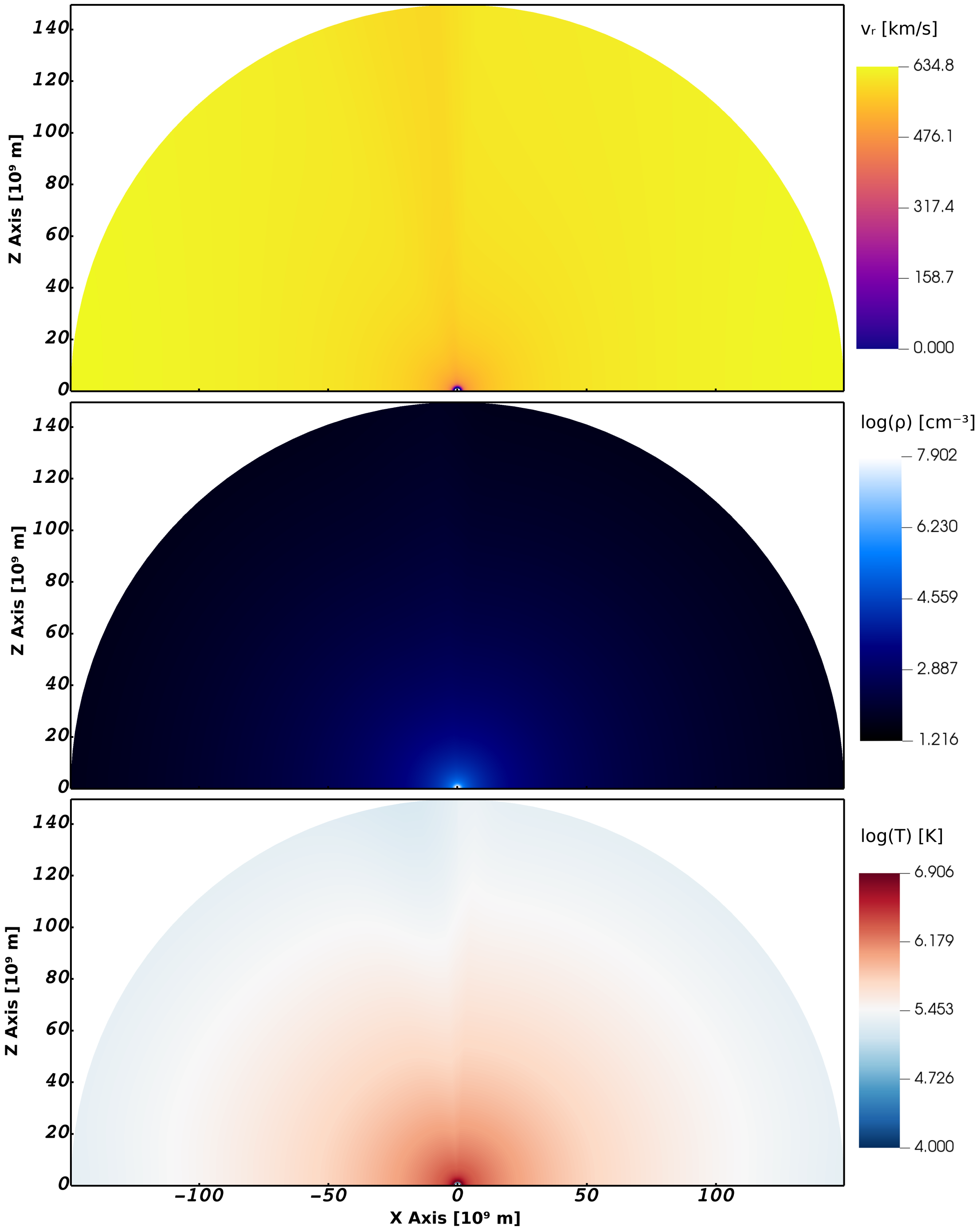

Figure 4.4: Polar slices of solar wind simulation results corresponding to the initially assumed set of free parameters for the WTD heating routine. (*Top panel*) Colormap plot of radial velocity v_r in $\mathrm{km\,s^{-1}}$. (*Middle panel*) Number density $\log_{10}(\rho)$ in units of cm^{-3} (*Bottom panel*) Temperature $\log_{10}(T)$ in K. The polar cuts are aligned to the rotational axis of the Sun and extend to the solar equator. All three panels show a highly spherically symmetric distribution of the respective parameters, with an exception on the polar upper boundary corresponding to the rotational axis.

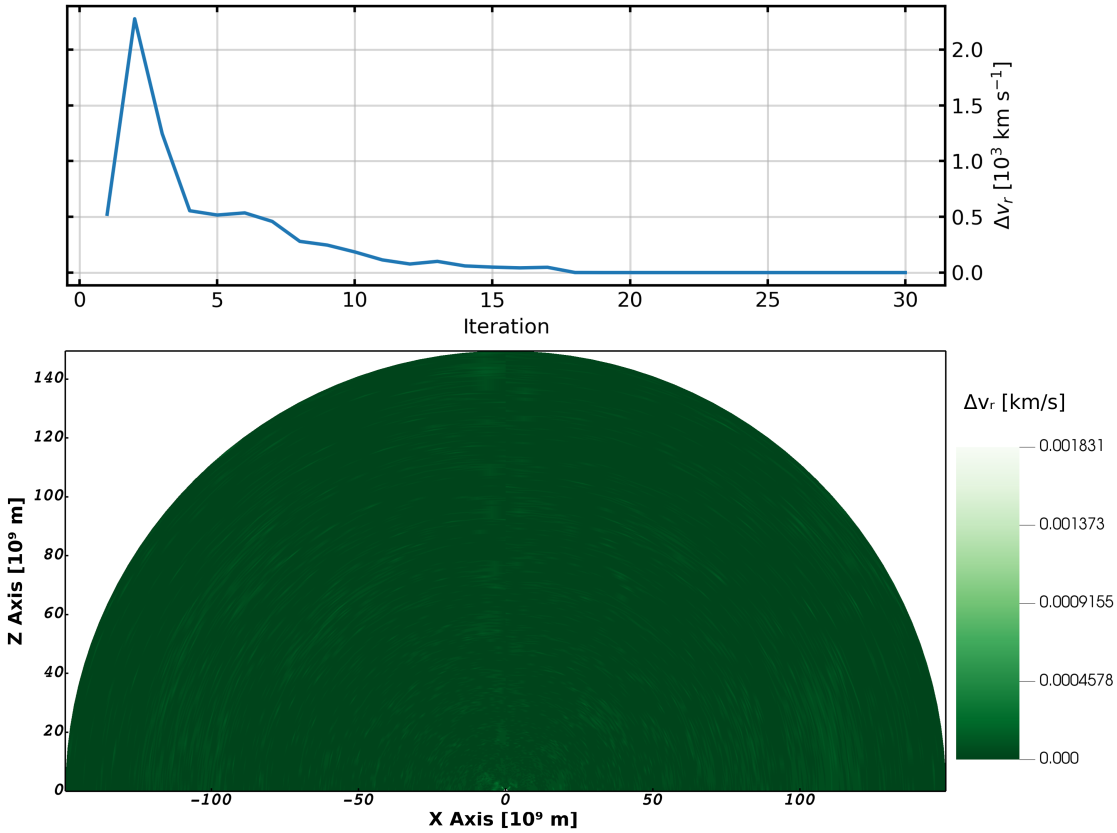

Figure 4.5: Relative difference in the parameter v_r (radial wind velocity) throughout the simulation run labeled *Initial* in this Chapter, illustrating the approach to an acceptable steady state solution. (*Upper panel*) Relative difference of v_r in $\mathrm{km\,s^{-1}}$ for iterative simulation states, related to a nodal value close to the outer boundary of the simulation domain. The simulation states are 1×10^4 time steps apart respectively. The curve shows three perturbations traveling through the simulation domain with successively smaller velocity peaks, before settling into a steady state. (*Bottom panel*) Polar slice, aligned to the solar rotational axis, displaying a colourmap of the residual v_r between the last 1×10^4 time steps. The variation in Δv_r is on the order of $< 5 \times 10^{-4}\,\mathrm{km\,s^{-1}}$, with a maximum of approximately $\Delta v_r = 1.8 \times 10^{-3}\,\mathrm{km\,s^{-1}}$, representing adequate variations to accept a steady state.

approximately $1\,\mathrm{AU}$. Much of the variation in the volumetric heating rate connected to this routine happens within $1 \times 10^{-1}\,\mathrm{R}_{\odot}$, which is resolved in this reference configuration of a coronal hole parameter space. In contrast to that, the results shown in Fig. 4.6 from the simulation grid do not have this fine radial resolution, as described previously. Excluding the innermost grid point, the results reproduced here start at a heliocentric distance of approximately $0.5\,\mathrm{R}_{\odot}$. As would be expected, much of the radial variations connected to the volumetric heating rate are therefore not reproduced here. This represents a good point of further refining this model: introducing a non-uniform grid through appropriate IMR would allow a much better level of radial refinement close to the stellar surface and therefore a better treatment of the variations in the heating output connected to the energy source term.

Comparing the actual values connected to this radial profile shows that the general trends between the solutions stemming from the simulation runs and the exemplary values from Cranmer (2010) are in agreement. The volumetric heating rate displays two peaks: the second one, occurring at approximately $2\,\mathrm{R}_{\odot}$, is clearly reflected in Fig. 3.2. At distances below that, the course simulation grid cannot reproduce the behaviour presented by Cranmer (2010), but the volumetric heating rate stays within an order of magnitude when compared to these results. The behaviour of Q_p/ρ with respect to the free parameter variation also follows the description given in Section 3.3.1, displaying lower values with increasing correlation length scale and decreasing flux-to-field ratio. The peak of the volumetric heating rate also moves to the right (i.e. to larger distances) for an increasing $L_{\perp}$. For large heliocentric distances, the volumetric heating rate converges for a variation in F/B, whereas its behaviour switches for $L_{\perp}$, showing increased values for a larger correlation length scale. In general terms, Fig. 3.2 and 4.6 show an agreeing value range of Q_p/ρ between approximately 1×10^{7} to $1 \times 10^{12}\,\mathrm{erg\,s^{-1}\,cm^{-3}}$.

Fig. 4.7 illustrates the wind velocity, number density and temperature profiles for a number of simulation runs using the constraints on the correlation length scale $L_{\perp}$ and the flux-to-field ratio F/B as described in Section 3.3.1. These radial profiles are compared to both the results achieved using the initial choices of $L_{\perp}$ and F/B, as well as the wind parameter measurements of PSP and SolO respectively, which span a large range of heliocentric distances. The PSP measurements correspond to the time frame of encounter 6, between August of 2020 and January of 2021. Data from SolO spans the available release time frame between October and December of 2020. These two data releases cover heliocentric distances between approximately $0.1\,\mathrm{AU}$ and $1\,\mathrm{AU}$, illustrating major wind parameter values and trends. With low heliolatitudes characterizing the orbits of both spacecrafts, the wind speed, density and temperature measurements of both PSP

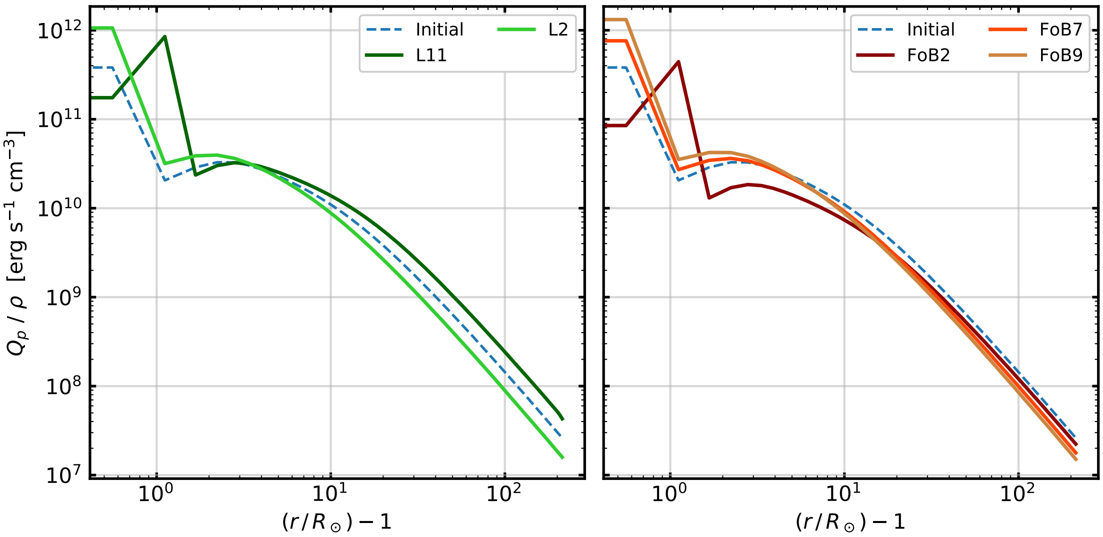

Figure 4.6: Variation in volumetric heating rate Q_p/ρ in units of $\mathrm{erg\,s^{-1}\,cm^{-3}}$ in reference to distance from the solar surface in units of $(r\,/\,R_\odot) - 1$. The blue dashed line in both panels represents results achieved with the nominal values of $L_\perp = 6.0/\sqrt{B\,[\mathrm{G}]}\mathrm{Mm}$ and $F/B = 5 \times 10^4\,\mathrm{erg\,s^{-1}\,cm^{-2}\,G^{-1}}$. (*Left panel*) Results from variations in the correlation length scale $L_\perp$ representing a scaling factor of 11.55 (marked as L11) and 2.876 (denoted with L2). (*Right panel*) Results from parameter variations of the flux-to-field ratio F/B connected to the wave energy density U_A as described in Section 3.3.1, illustrating values of 2×10^4 (marked as FoB2), 7×10^4 (denoted by FoB7) and 9×10^4 (marked as FoB9). Both columns reproduce constraints on the free parameters as discussed in Cranmer (2010).

and SolO are reflective of constraints connected to the slow solar wind regime.

There are several key aspects of the solutions visible in this figure. Looking at the radial wind velocity (corresponding to the first row of panels in Fig. 4.7), it is rather apparent that a significant discrepancy exists between the measurement constraints and the values gathered from the simulations. In both cases ($L_\perp$ and F/B variations), the terminal wind speed reached at $1\,\mathrm{AU}$ varies between 600 and $800\,\mathrm{km\,s^{-1}}$, which would be associated with the fast wind regime expected to emanate from coronal holes. In contrast to that, measurements from PSP and SolO are centered around approximately 350 to $400\,\mathrm{km\,s^{-1}}$, indicative of the slow solar wind regime. This coincides with the orbital trajectories of both spacecrafts, which move close to the solar equator in the observed time frame.

The variations in the number density appear smaller, though the logarithmic scale of the second row of panels in Fig. 4.7 is deceptive in this regard. In all cases, the density profiles follow the radial trends constrained by PSP and SolO closely, although the model results overestimate the density with a constant offset, similar to the velocity profiles. Connected to the large velocities seen in these cases, assuming a fast wind regime would imply a density value on the order of 1 - $10\,\mathrm{cm^{-3}}$, which is overestimated by one to two orders of magnitude here.

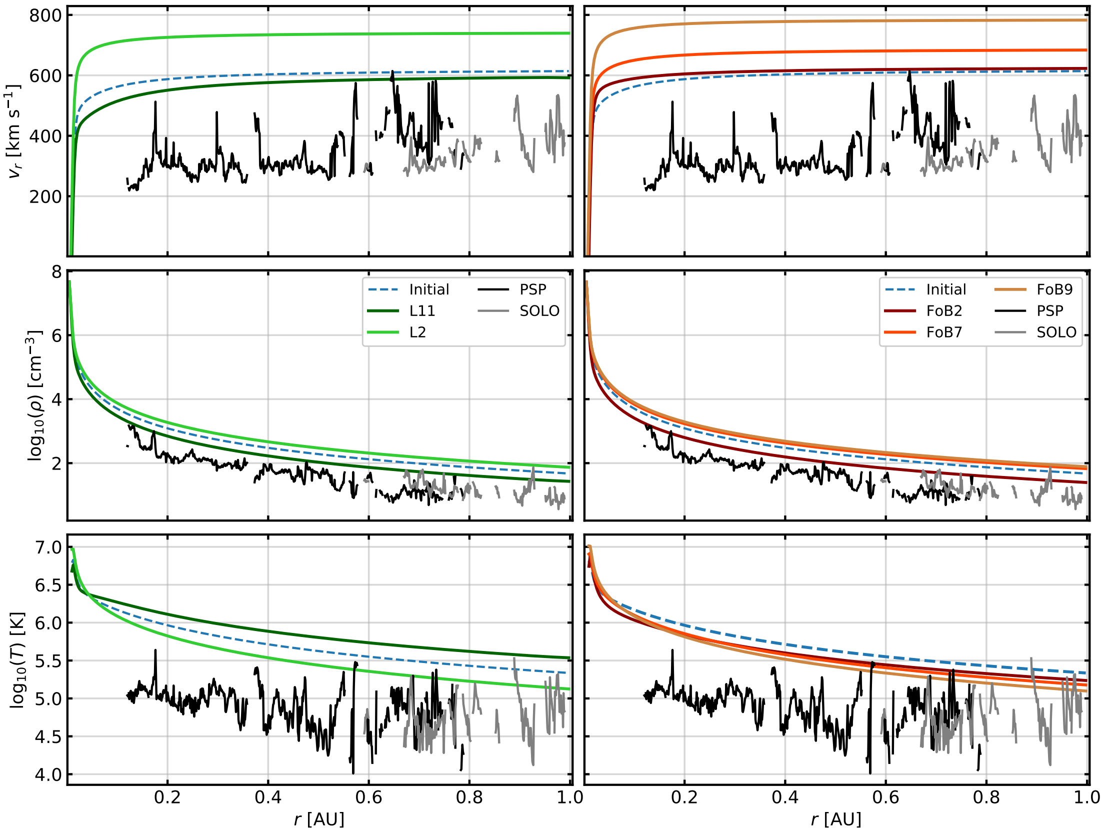

Figure 4.7: Radial wind parameter profiles for solar wind simulations resulting from variations in the free parameters of $L_\perp$ and F/B. The three panels, from top to bottom, represent the radial wind speed v_r in $\mathrm{km\,s^{-1}}$, number density $\log_{10}(\rho)$ in $\mathrm{cm^{-3}}$ and temperature $\log_{10}(T)$ in K respectively. The values are given with respect to heliocentric distance r in AU. The blue dashed line in all panels represents results achieved with the nominal values of $L_\perp = 6.0/\sqrt{B\,[\mathrm{G}]}\mathrm{Mm}$ and $F/B = 5 \times 10^4\,\mathrm{erg\,s^{-1}\,cm^{-2}\,G^{-1}}$. (*Left column*) Results from variations in the correlation length scale $L_\perp$ representing a scaling factor of 11.55 (marked as L11) and 2.876 (denoted with L2). (*Right column*) Results from parameter variations of the flux-to-field ratio F/B connected to the wave energy density U_A as described in Section 3.3.1, illustrating values of 2×10^4 (marked as FoB2), 7×10^4 (denoted by FoB7) and 9×10^4 (marked as FoB9). Both columns reproduce constraints on the free parameters as discussed in Cranmer (2010). Black and grey curves show constraints on the wind parameters through the measurements of PSP and SolO respectively.

The discrepancy between the simulation results and measurement constraints can also be seen in the bottom row of panels in Fig. 4.7: it shows that the simulation results overestimate the temperature at a scale of one order of magnitude for small heliocentric distances. This discrepancy drops to approximately half an order of magnitude for larger distances, although the larger scale of measurement variations for both PSP and SolO at these distances lead to an overlap between the results and constraints in some cases. Depending on the change in free parameters, the temperature reached at very small heliocentric distances are also very high, reaching 1×10^7 K in the cases of a small correlation length scale or a large flux-to-field ratio (cases L2 and FoB9 in Fig. 4.7 respectively).

While the velocity and density structures resulting from the free parameter variations presented here mainly show profiles differentiated by their absolute values, the temperature distributions show significant variation with respect to their radial behaviour as well. This can most clearly be seen in the bottom left panel of Fig. 4.7: the temperature profile resulting from a larger correlation length scale shows a steep radial decline at small heliocentric distances before flattening out significantly, reaching a value of approximately $\log T = 5.5$ at a distance of $1\,\mathrm{AU}$. In comparison to that, the temperature profiles resulting from smaller correlation length scales show a similarly steep profile close to the inner boundary of the domain, but this steep trend continues towards lower temperatures much further than in the previous case. The temperature profiles of both bottom panels in Fig. 4.7 closely reflect the behaviour in the volumetric heating rate as seen in Fig. 4.6 and described previously in this chapter.

Nevertheless, all three parameters follow the trends displayed in the measurement constraints to some extend: for the available heliocentric distance regime, the wind velocity increases slightly at close distances, after which it reaches a near-constant terminal value. In contrast to that, the density and temperature results of the simulation runs follow radially decreasing profiles very closely resembling the trends visible in the measurement data. A lack of direct measurements for heliocentric distances below approximately $0.1\,\mathrm{AU}$ prevents a comparison of the trends at very low heights in the solar corona. This is where the variation in free parameters results in the most distinct differences of the radial wind parameter profiles - future data releases for both PSP and SolO will start to fill in this gap when both missions approach their desired perihelia.

Finally, it is of interest to investigate the mass loss and ram pressure profiles resulting from the individual simulation runs in comparison to values that can be derived from PSP and SolO measurements. Radial profiles of these two properties with respect to the same variations in free parameters as described previously are shown in Fig.4.8. Since both the mass loss rate and ram pressure are derived from primary simulation results, the discrepancies in velocity and density discussed previously are perpetuated here. The

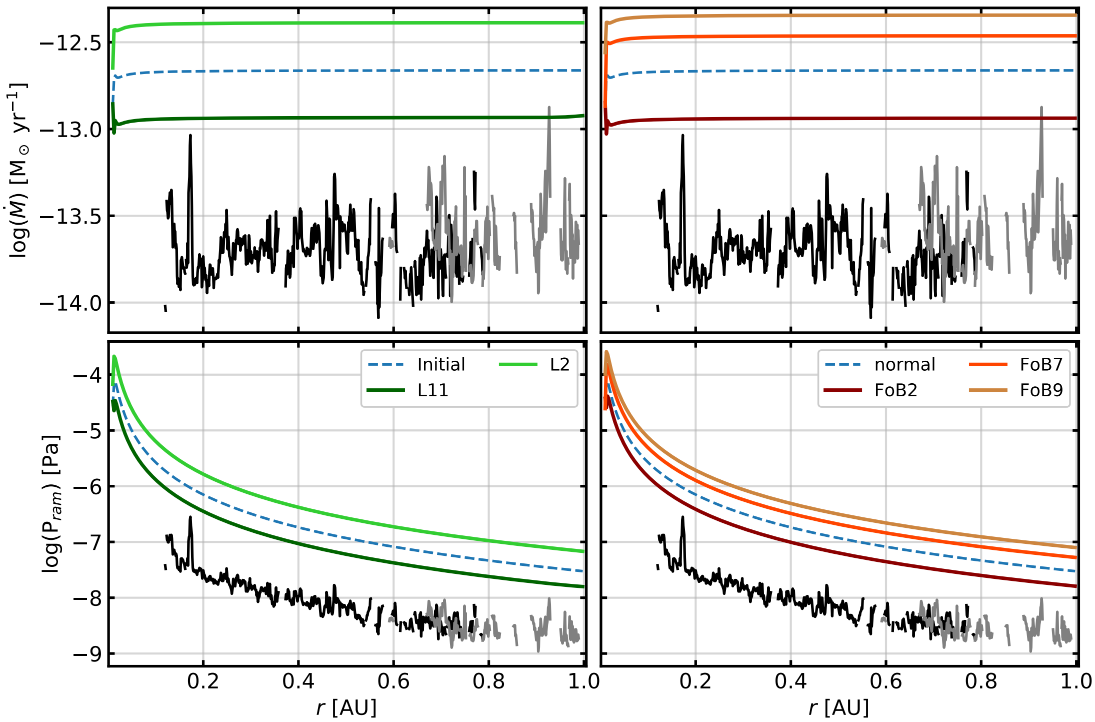

Figure 4.8: Mass loss and ram pressure profiles for solar wind simulations with variations in free parameters of $L_\perp$ and F/B, compared to PSP and SolO measurements. The left and right columns of panels are split with respect to $L_\perp$ and F/B variations respectively, as described in Fig. 4.7. The two rows of panels display mass loss rate in $\mathrm{M_\odot\,yr^{-1}}$ (top row) and wind ram pressure in units of Pa (bottom row) with respect to heliocentric distance in AU. Both parameters are derived from simulation results following Eq. 2.2 and 2.3.

overestimation of both parameters with respect to the *in situ* measured values leads to a difference in mass loss rate of between approximately one half to one order of magnitude (as shown in the upper row of panels in Fig. 4.8). This is to be expected due to high velocity and density values, following Eq. 2.2. In a similar manner, the ram pressure values seen in the bottom row of panels in Fig. 4.8 overestimate the values corresponding to the *in situ* measurements. As displayed in Eq. 2.3, the ram pressure value depends on the square of the velocity, increasing the discrepancy in values between the simulation results and measurements to approximately one to one and a half orders of magnitude.

The results gathered from the here presented simulation runs are only in rudimentary agreement with the wind parameter constraints imposed by PSP and SolO measurements. This reflects the fact that the solar wind model generated in this work is a somewhat basic description of a highly complex problem. Nevertheless, the global trends expected for the solar wind parameters in terms of velocity, density and temperature profiles are reproduced here, illustrating the potential of further development to generate a solar wind model based on a WTD heating mechanism that more closely reflects the solar wind structure. Accurate models in this regard are necessary to investigate the stellar wind parameters of larger samples of solar-type stars, gaining a more concise picture of this phenomenon.

Chapter 5

Conclusion

Models of the solar wind have evolved significantly since the first descriptions of a supersonically expanding solar corona. Through the inclusion of more complex physical mechanisms such as the influence of magnetic fields and stellar rotation on the mass outflow, descriptions of the solar wind have become more accurate in reflecting observations taken *in situ* by spacecrafts such as the Parker Solar Probe and Solar Orbiter.

The simulation setup implemented to `NIRVANA`, the general-purpose MHD code used in this work, imposes limitations on the generation of an appropriate grid to investigate the effects of the adopted WTD heating routine. An ideal domain decomposition would include a non-uniform grid with small radial grid cells closer to the inner boundary of the simulation domain, where the heating mechanism produces the most varied behaviour. This conflicts with the process of implementing initial mesh refinement in the code, which refines the domain uniformly in all coordinate directions. Improving the simulation results could therefore include either scaling down the domain size overall, in order to produce smaller radial grid cells in a uniform manner, or modifying the IMR routine within `NIRVANA` to facilitate a non-uniform refinement algorithm. Scaling down the simulation domain would potentially exclude many of the current available measurements of PSP and SolO at larger heliocentric distances. However, both spacecrafts will eventually approach perihelia much closer to the Sun and provide complementary measurements of solar wind parameters at a proximity not reached before, gathering insight into the physical mechanisms that heat the solar corona and drive the solar wind.

The magnetic field implementation in this work was done using a simplified, purely radial field, which overlooks the complexity of the coronal field structure at small heliocentric distances. Introducing a magnetic field more representative of the solar case would most likely help to reproduce the structure of the solar wind more accurately and better reflect the slow wind regime measurements provided by PSP and SolO. Using dipolar, quadrupolar or octupolar components to represent the magnetic field would provide a way of approaching the complexity of the coronal field structure. Investigations have also been carried out using spherical harmonic decompositions of solar magnetograms, providing a way of further moving towards realistic boundary conditions for the magnetic fields.

All of these points reflect the potential of using `NIRVANA` to generate a representative model of the solar wind and investigate the behaviour of stellar winds for solar-like stars. The accessibility of `NIRVANA` also provides the potential of adapting the energy source term currently represented by a WTD heating routine to different treatments representative of other mechanisms. That being stated, generating a consistent simulation procedure from a generalized MHD code requires a great deal of small-scale adjustments and intimate familiarity with the code base. The solar wind model generated in this work reflects a somewhat basic description of a highly complex problem, and the results achieved in this work therefore only reproduce the radial solar wind parameter trends seen in the constraints imposed by PSP and SolO, while not being in exact agreement. This illustrates both the potential and necessity of further development regarding a solar wind model using `NIRVANA`.

Developing an accurate solar wind model constrained by *in situ* measurements of PSP and SolO also provides the potential of investigating larger samples of solar-like stars on their stellar wind parameters. While not within the scope of this work, it represents a way of using the results and conclusions derived here to generate comparability to stellar wind investigations conducted using other simulation codes. The results of stellar wind simulations are imperative in gaining a larger understanding of this general phenomenon when compared to the reasonably small sample of solar-like stars for which wind observations are available.

References

Acton, C., Bachman, N., Semenov, B., and Wright, E. (2018). “A look towards the future in the handling of space science mission geometry”. *Planet. Space Sci.* 150, pp. 9–12. DOI: 10.1016/j.pss.2017.02.013.

Acton, C. H. (1996). “Ancillary data services of NASA’s Navigation and Ancillary Information Facility”. *Planet. Space Sci.* 44.1, pp. 65–70. DOI: 10.1016/0032-0633(95)00107-7.

Ahuir, J., Brun, A. S., and Strugarek, A. (2020). “From stellar coronae to gyrochronology: A theoretical and observational exploration”. *A&A* 635, A170, A170. DOI: 10.1051/0004-6361/201936974.

Alfvén, H. (1941). “On the solar corona”. *Arkiv för matematik, astronomi och fysik* 27 A.25, p. 1. ISSN: 0365-4133.

Annex, A., Pearson, B., Seignovert, B., Carcich, B., Eichhorn, H., et al. (2020). “SpiceyPy: a Pythonic Wrapper for the SPICE Toolkit”. *The Journal of Open Source Software* 5.46, 2050, p. 2050. DOI: 10.21105/joss.02050.

Biermann, L. (1951). “Kometenschweife und solare Korpuskularstrahlung”. *ZAp* 29, p. 274.

Biermann, L. (1957). “Solar corpuscular radiation and the interplanetary gas”. *The Observatory* 77, pp. 109–110.

Boro Saikia, S., Jin, M., Johnstone, C. P., Lüftinger, T., Güdel, M., et al. (2020). “The solar wind from a stellar perspective. How do low-resolution data impact the determination of wind properties?” *A&A* 635, A178, A178. DOI: 10.1051/0004-6361/201937107.

Carrington, R. C. (1859). “Description of a Singular Appearance seen in the Sun on September 1, 1859”. *MNRAS* 20, pp. 13–15. DOI: 10.1093/mnras/20.1.13.

Case, A. W., Kasper, J. C., Stevens, M. L., Korreck, K. E., Paulson, K., et al. (2020). “The Solar Probe Cup on the Parker Solar Probe”. *ApJS* 246.2, 43, p. 43. DOI: 10.3847/1538-4365/ab5a7b.

Chamberlain, J. W. (1960). “Interplanetary Gas.II. Expansion of a Model Solar Corona.” *ApJ* 131, p. 47. DOI: 10.1086/146805.

Chapman, S. (1918). "An Outline of a Theory of Magnetic Storms". *Proceedings of the Royal Society of London Series A* 95.666, pp. 61–83. DOI: 10.1098/rspa.1918.0049.

Chapman, S. and Zirin, H. (1957). "Notes on the Solar Corona and the Terrestrial Ionosphere". *Smithsonian Contributions to Astrophysics* 2, p. 1.

Cohen, O., Drake, J. J., Glocer, A., Garraffo, C., Poppenhaeger, K., et al. (2014). "Magnetospheric Structure and Atmospheric Joule Heating of Habitable Planets Orbiting M-dwarf Stars". *ApJ* 790.1, 57, p. 57. DOI: 10.1088/0004-637X/790/1/57.

Cohen, O. and Drake, J. J. (2014). "A Grid of MHD Models for Stellar Mass Loss and Spin-down Rates of Solar Analogs". *ApJ* 783.1, 55, p. 55. DOI: 10.1088/0004-637X/783/1/55.

Cranmer, S. R. and van Ballegooijen, A. A. (2005). "On the Generation, Propagation, and Reflection of Alfvén Waves from the Solar Photosphere to the Distant Heliosphere". *ApJS* 156.2, pp. 265–293. DOI: 10.1086/426507.

Cranmer, S. R. (2009). "Coronal Holes". *Living Reviews in Solar Physics* 6.1, 3, p. 3. DOI: 10.12942/lrsp-2009-3.

Cranmer, S. R. (2010). "An Efficient Approximation of the Coronal Heating Rate for use in Global Sun-Heliosphere Simulations". *ApJ* 710.1, pp. 676–688. DOI: 10.1088/0004-637X/710/1/676.

Cranmer, S. R. and Winebarger, A. R. (2019). "The Properties of the Solar Corona and Its Connection to the Solar Wind". *ARA&A* 57, pp. 157–187. DOI: 10.1146/annurev-astro-091918-104416.

Data - The Solar Wind Electrons, Alphas and Protons (SWEAP). URL: http://sweap.cfa.harvard.edu/Data.html. (accessed: 12.10.2021).

Edlén, B. (1943). "Die Deutung der Emissionslinien im Spektrum der Sonnenkorona. Mit 6 Abbildungen." *ZAp* 22, p. 30.

ESA SPICE Service. *Solar Orbiter Operational SPICE Kernel Dataset*. DOI: 10.5270/esa-kt1577e.

Fichtinger, B., Güdel, M., Mutel, R. L., Hallinan, G., Gaidos, E., et al. (2017). "Radio emission and mass loss rate limits of four young solar-type stars". *A&A* 599, A127, A127. DOI: 10.1051/0004-6361/201629886.

Gallet, F. and Bouvier, J. (2015). "Improved angular momentum evolution model for solar-like stars. II. Exploring the mass dependence". *A&A* 577, A98, A98. DOI: 10.1051/0004-6361/201525660.

Gombosi, T. I., van der Holst, B., Manchester, W. B., and Sokolov, I. V. (2018). “Extended MHD modeling of the steady solar corona and the solar wind”. *Living Reviews in Solar Physics* 15.1, 4, p. 4. DOI: 10.1007/s41116-018-0014-4.

Grotrian, W. (1939). “Zur Frage der Deutung der Linien im Spektrum der Sonnenkorona”. *Naturwissenschaften* 27.13, pp. 214–214. DOI: 10.1007/BF01488890.

Hodgson, R. (1859). “On a curious Appearance seen in the Sun”. *MNRAS* 20, pp. 15–16. DOI: 10.1093/mnras/20.1.15.

Hollweg, J. V. (1986). “Transition region, corona, and solar wind in coronal holes”. *J. Geophys. Res.* 91.A4, pp. 4111–4125. DOI: 10.1029/JA091iA04p04111.

Johnstone, C. P., Güdel, M., Brott, I., and Lüftinger, T. (2015a). “Stellar winds on the main-sequence. II. The evolution of rotation and winds”. *A&A* 577, A28, A28. DOI: 10.1051/0004-6361/201425301.

Johnstone, C. P., Güdel, M., Lüftinger, T., Toth, G., and Brott, I. (2015b). “Stellar winds on the main-sequence. I. Wind model”. *A&A* 577, A27, A27. DOI: 10.1051/0004-6361/201425300.

Kasper, J. C., Abiad, R., Austin, G., Balat-Pichelin, M., Bale, S. D., et al. (2016). “Solar Wind Electrons Alphas and Protons (SWEAP) Investigation: Design of the Solar Wind and Coronal Plasma Instrument Suite for Solar Probe Plus”. *Space Sci. Rev.* 204.1-4, pp. 131–186. DOI: 10.1007/s11214-015-0206-3.

Kislyakova, K. G., Johnstone, C. P., Odert, P., Erkaev, N. V., Lammer, H., et al. (2014). “Stellar wind interaction and pick-up ion escape of the Kepler-11 “super-Earths””. *A&A* 562, A116, A116. DOI: 10.1051/0004-6361/201322933.

Lichtenegger, H. I. M., Lammer, H., Grießmeier, J. M., Kulikov, Y. N., von Paris, P., et al. (2010). “Aeronomical evidence for higher CO_2 levels during Earth’s Hadean epoch”. *Icarus* 210.1, pp. 1–7. DOI: 10.1016/j.icarus.2010.06.042.

Marsch, E., Schwenn, R., Rosenbauer, H., Muehlhaeuser, K. H., Pilipp, W., et al. (1982). “Solar wind protons: Three-dimensional velocity distributions and derived plasma parameters measured between 0.3 and 1 AU”. *J. Geophys. Res.* 87.A1, pp. 52–72. DOI: 10.1029/JA087iA01p00052.

Matt, S. P., MacGregor, K. B., Pinsonneault, M. H., and Greene, T. P. (2012). “Magnetic Braking Formulation for Sun-like Stars: Dependence on Dipole Field Strength and Rotation Rate”. *ApJ* 754.2, L26, p. L26. DOI: 10.1088/2041-8205/754/2/L26.

Matthaeus, W. H., Zank, G. P., Oughton, S., Mullan, D. J., and Dmitruk, P. (1999). "Coronal Heating by Magnetohydrodynamic Turbulence Driven by Reflected Low-Frequency Waves". *ApJ* 523.1, pp. L93–L96. DOI: 10.1086/312259.

McComas, D. J., Bame, S. J., Barraclough, B. L., Feldman, W. C., Funsten, H. O., et al. (1998). "Ulysses' return to the slow solar wind". *Geophys. Res. Lett.* 25.1, pp. 1–4. DOI: 10.1029/97GL03444.

McComas, D. J., Elliott, H. A., Schwadron, N. A., Gosling, J. T., Skoug, R. M., et al. (2003). "The three-dimensional solar wind around solar maximum". *Geophys. Res. Lett.* 30.10, 1517, p. 1517. DOI: 10.1029/2003GL017136.

Müller, D., St. Cyr, O. C., Zouganelis, I., Gilbert, H. R., Marsden, R., et al. (2020). "The Solar Orbiter mission. Science overview". *A&A* 642, A1, A1. DOI: 10.1051/0004-6361/202038467.

Neugebauer, M. (1997). "Pioneers of space physics: A career in the solar wind". *J. Geophys. Res.* 102.A12, pp. 26887–26894. DOI: 10.1029/97JA02444.

Osterbrock, D. E. (1961). "The Heating of the Solar Chromosphere, Plages, and Corona by Magnetohydrodynamic Waves." *ApJ* 134, p. 347. DOI: 10.1086/147165.

Owen, C. J., Bruno, R., Livi, S., Louarn, P., Al Janabi, K., et al. (2020). "The Solar Orbiter Solar Wind Analyser (SWA) suite". *A&A* 642, A16, A16. DOI: 10.1051/0004-6361/201937259.

Parker, E. N. (1958). "Dynamics of the Interplanetary Gas and Magnetic Fields." *ApJ* 128, p. 664. DOI: 10.1086/146579.

Parker, E. N. (1965). "Dynamical Theory of the Solar Wind". *Space Sci. Rev.* 4.5-6, pp. 666–708. DOI: 10.1007/BF00216273.

Parker, E. N. (1972). "Topological Dissipation and the Small-Scale Fields in Turbulent Gases". *ApJ* 174, p. 499. DOI: 10.1086/151512.

Parker, E. N. (2001). "A history of the solar wind concept". In: *The Century of Space Science*. Ed. by J. A. M. Bleeker, J. Geiss, and M. C. E. Huber. Dordrecht: Springer Netherlands, pp. 225–255. ISBN: 978-94-010-0320-9. DOI: 10.1007/978-94-010-0320-9_9.

Parker Solar Probe: Humanity's First Visit to a Star. URL: https://www.nasa.gov/content/goddard/parker-solar-probe-humanity-s-first-visit-to-a-star. (accessed: 23.08.2021).

Parker Solar Probe Instruments. URL: https://www.nasa.gov/content/goddard/parker-solar-probe-instruments. (accessed: 23.08.2021).

Peter, H. and Dwivedi, B. N. (2014). "Discovery of the Sun's million-degree hot corona". *Frontiers in Astronomy and Space Sciences* 1, 2, p. 2. DOI: 10.3389/fspas.2014.00002.

Réville, V., Brun, A. S., Matt, S. P., Strugarek, A., and Pinto, R. F. (2015). "The Effect of Magnetic Topology on Thermally Driven Wind: Toward a General Formulation of the Braking Law". *ApJ* 798.2, 116, p. 116. DOI: 10.1088/0004-637X/798/2/116.

Réville, V., Folsom, C. P., Strugarek, A., and Brun, A. S. (2016). "Age Dependence of Wind Properties for Solar-type Stars: A 3D Study". *ApJ* 832.2, 145, p. 145. DOI: 10.3847/0004-637X/832/2/145.

Riley, P., Linker, J. A., Mikić, Z., Lionello, R., Ledvina, S. A., et al. (2006). "A Comparison between Global Solar Magnetohydrodynamic and Potential Field Source Surface Model Results". *ApJ* 653.2, pp. 1510–1516. DOI: 10.1086/508565.

Russell, A. J. B. (2018). "Commentary: Discovery of the Sun's million-degree hot corona". *Frontiers in Astronomy and Space Sciences* 5, 9, p. 9. DOI: 10.3389/fspas.2018.00009.

Smith, E. J. (2001). "The heliospheric current sheet". *J. Geophys. Res.* 106.A8, pp. 15819–15832. DOI: 10.1029/2000JA000120.

Solar Orbiter Archive. URL: https://soar.esac.esa.int/soar/. (accessed: 12.10.2021).

Solar Orbiter Instruments. URL: https://www.nasa.gov/content/solar-orbiter-instruments. (accessed: 23.08.2021).

Sturrock, P. A. and Uchida, Y. (1981). "Coronal heating by stochastic magnetic pumping". *ApJ* 246, pp. 331–336. DOI: 10.1086/158926.

The Extrasolar Planets Encyclopaedia. URL: http://exoplanet.eu/. (accessed: 25.10.2021).

Vidotto, A. A., Gregory, S. G., Jardine, M., Donati, J. F., Petit, P., et al. (2014a). "Stellar magnetism: empirical trends with age and rotation". *MNRAS* 441.3, pp. 2361–2374. DOI: 10.1093/mnras/stu728.

Vidotto, A. A., Jardine, M., Morin, J., Donati, J. F., Opher, M., et al. (2014b). "M-dwarf stellar winds: the effects of realistic magnetic geometry on rotational evolution and planets". *MNRAS* 438.2, pp. 1162–1175. DOI: 10.1093/mnras/stt2265.

Vidotto, A. A. (2021). "The evolution of the solar wind". *Living Reviews in Solar Physics* 18.1, 3, p. 3. DOI: 10.1007/s41116-021-00029-w.

Wilcox, J. M. and Ness, N. F. (1965). "Quasi-Stationary Corotating Structure in the Interplanetary Medium". *J. Geophys. Res.* 70.23, pp. 5793–5805. DOI: 10.1029/JZ070i023p05793.

Wood, B. E. (2004). “Astrospheres and Solar-like Stellar Winds”. *Living Reviews in Solar Physics* 1.1, 2, p. 2. DOI: 10.12942/lrsp-2004-2.

Wood, B. E. (2018). “Implications of Recent Stellar Wind Measurements”. In: *Journal of Physics Conference Series*. Vol. 1100. Journal of Physics Conference Series, p. 012028. DOI: 10.1088/1742-6596/1100/1/012028.

Wood, B. E., Müller, H.-R., Redfield, S., and Edelman, E. (2014). “Evidence for a Weak Wind from the Young Sun”. *ApJ* 781.2, L33, p. L33. DOI: 10.1088/2041-8205/781/2/L33.

Wood, B. E., Müller, H.-R., Redfield, S., Konow, F., Vannier, H., et al. (2021). “New Observational Constraints on the Winds of M dwarf Stars”. *ApJ* 915.1, 37, p. 37. DOI: 10.3847/1538-4357/abfda5.

Ziegler, U. (2008). “The NIRVANA code: Parallel computational MHD with adaptive mesh refinement”. *Computer Physics Communications* 179.4, pp. 227–244. DOI: 10.1016/j.cpc.2008.02.017.

Appendix A

Park Wind Solution

In his seminal work, Parker (1958) illustrated, through the conservation of mass and momentum, that the velocity of a solar wind must transition from a subsonic regime close to the Sun into a supersonic expansion after a critical distance r_c. This behaviour is linked to the radial temperature profile $T(r)$ throughout the expanding corona and assumes a stellar atmosphere strongly bound through gravity (Parker 1958, 1965). To illustrate the expected behaviour of the solar wind with respect to distance from the Sun, it is helpful to look at the most basic form of the wind solution: an isothermal corona in radially symmetric steady expansion without any influence of a magnetic field.

We start with the equation of mass continuity, satisfying the condition that there are no mass sinks in the hydrodynamic system representing the solar wind

$$\frac{\partial \rho}{\partial t} + \vec{\nabla}\left(\rho \vec{v}\right) = 0 \tag{A.1}$$

Here, ρ denotes the mass density and $\vec{v}$ the wind velocity. We continue with the equation of momentum conservation, which satisfies the condition that changes in momentum are results of net forces acting upon the system

$$\rho\left(\frac{\partial \vec{v}}{\partial t} + \vec{v}\cdot\vec{\nabla}\vec{v}\right) = -\frac{\rho G M_{\odot}}{r^2}\cdot\vec{e}_r - \vec{\nabla}P \tag{A.2}$$

For an isothermal solar wind, only gravitational forces and the thermodynamic pressure act upon the wind. In this equation, $\vec{e}_r$ represents the unit vector in radial direction and P denotes the thermal pressure. Staying with the simplified model of solar mass outflow, we can assume a steady state (implying $\partial_t = 0$) and spherical symmetry ($\partial_\theta = \partial_\phi = 0$). Under these assumptions, Eq. A.1 and A.2 simplify to the base equations in the thermally driven solar wind derived by Parker (1958)

$$\frac{d}{dr}\left(\rho r^2 v_r\right) = 0 \tag{A.3}$$

$$\rho v_r \frac{dv_r}{dr} = -\frac{\rho G M_\odot}{r^2} - \frac{dP}{dr} \tag{A.4}$$

We now substitute the thermal pressure term P with the ideal gas law

$$P = \frac{\rho k_B T}{\mu m_p} = \rho c_s^2 \tag{A.5}$$

where k_B represents the Boltzmann constant, m_p the mass of a proton, μ the mean molecular weight and T the temperature of the wind. We follow simplifying assumptions and treat the wind with an isothermal equation of state, assuming $T =$ const., and use this to calculate the radial derivative of P

$$\frac{dP}{dr} = \frac{k_B T}{\mu m_p} \cdot \frac{d\rho}{dr} = c_s^2 \cdot \frac{d\rho}{dr} \tag{A.6}$$

Where c_s represents the isothermal speed of sound. We use Eq. A.3 to substitute $d\rho/dr$ into the previous equation, resulting in:

$$\frac{dP}{dr} = c_s^2 \left(-\frac{\rho}{v_r}\frac{dv_r}{dr} - \frac{2\rho}{r}\right) \tag{A.7}$$

This term can be implemented into Eq. A.4, which is rearranged to form the momentum equation of an isothermal solar wind

$$\rho v_r \frac{dv_r}{dr} = -\frac{\rho G M_\odot}{r^2} + c_s^2 \left(\frac{\rho}{v_r}\frac{dv_r}{dr} + \frac{2\rho}{r}\right) \tag{A.8}$$

$$\frac{v_r^2 - c_s^2}{v_r}\frac{dv_r}{dr} = \left(-\frac{G M_\odot}{r^2} + \frac{2c_s^2}{r}\right) \tag{A.9}$$

It is apparent that Eq. A.9 has a singularity at $v_r = c_s$. The continuity of this equation is given if both enumerator and denominator reach zero simultaneously. With this, the critical point r_c is introduced, where $v_r(r_c) = c_s$

$$-\frac{G M_\odot}{r_c^2} + \frac{2c_s^2}{r_c} = 0 \qquad \rightarrow \qquad r_c = \frac{G M_\odot}{2c_s^2} \tag{A.10}$$

This parameter can be substituted into Eq. A.9, and integrating this equation gives a solution for the wind speed v_r with respect to distance r

$$\left(\frac{v_r}{c_s}\right)^2 - \ln\left(\frac{v_r}{c_s}\right)^2 = 4\frac{r_c}{r} + 4\ln\frac{r}{r_c} + C \tag{A.11}$$

The last part in deriving the solution presented by Parker (1958, 1965) is to analyse the family of solutions representative of Eq. A.11, which are separated by the integration constant C. As argued by Parker (1965), the solution is required to pass through the critical point, with subsonic velocities before and supersonic velocities after this point. This transsonic solution is characterized by Eq. A.12 with a value of $C = -3$

$$\frac{v_r^2}{c_s^2} - \ln\left(\frac{v_r^2}{c_s^2}\right) = 4\left[\ln\left(\frac{r}{r_c}\right) + \frac{r_c}{r}\right] - 3 \tag{A.12}$$

This equation can be solved with e.g. a bisection algorithm. While this solution is only a simplified approximation for the solar wind, it serves to illustrate key factors in its behaviour. Fig. 1.1 shows a range of wind speed profiles with varying isothermal temperatures.

Appendix B

PSP Solar Wind Measurements

The SPC measurement data presented in Chapter 2 represents the solar wind parameters measured during encounter 6 of the PSP orbit. The whole available measurement time frame spans a time period including 7 encounters. The following figures represent the same data analysis described in Sec. 2.3 for these time periods, showing the orbital trajectory of the spacecraft, as well as the wind velocity, density and temperature measured by SPC and the derived mass loss rate and ram pressure values.

Many of the features described in Sec. 2.3 can also be identified in these figures, especially the apparent bimodal structure of the solar wind parameters with respect to distance. This is a result of overlapping distance values as the spacecraft approaches and recedes from the perihelion during the respective encounter. Data reduction by quality flags excludes a large amount of the total measurement data, especially at large heliocentric distances. This can lead to indicators for monthly data being present in the legend of a figure, while not represented in the actual trajectory plot, as can exemplary be seen in Fig. B.5. If an encounter period includes date ranges for which no measurement is available, the dates in question might be referenced in the figure description, while not being present in the plot itself (as exemplified by Fig. B.1).

Encounter 1

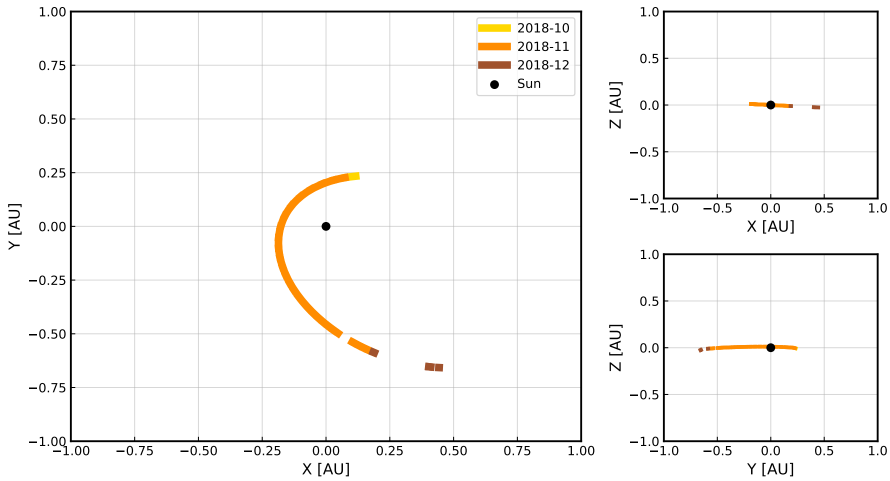

Figure B.1: PSP positional data between October 31st, 2018 and January 19th, 2019, encompassing encounter 1. The three panels illustrate planar cuts in the HIC system, where the xy-plane corresponds to the solar equatorial plane, and the z-axis is aligned with the solar rotational axis. Data points are separated by colour into the respective months of observation. No measurement data is available from January 1st to 19th.

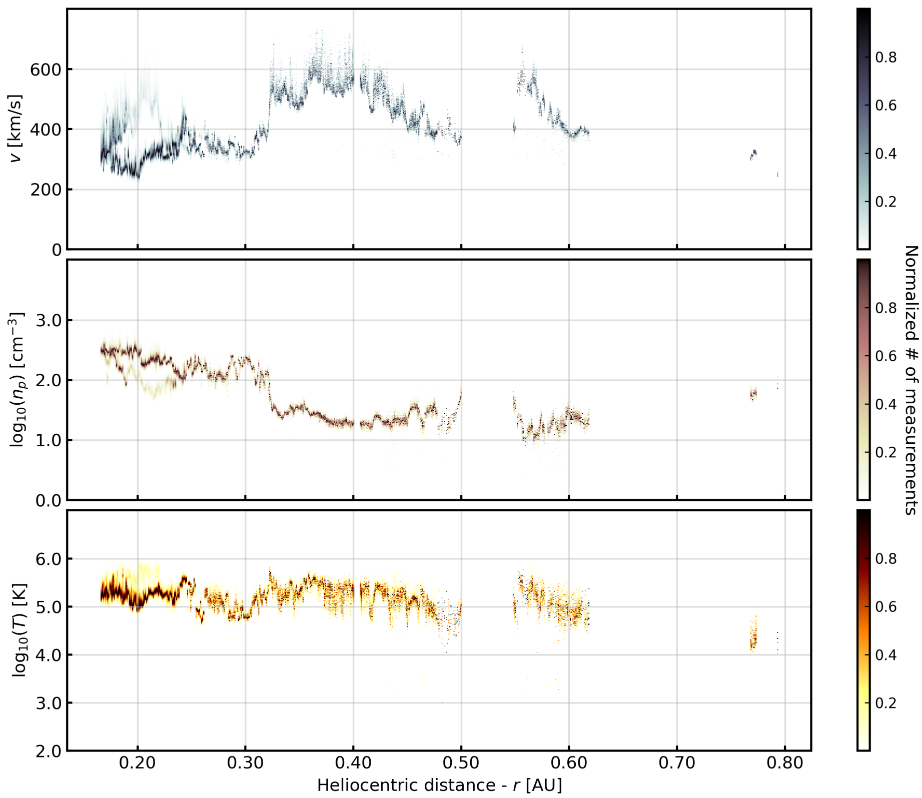

Figure B.2: SPC measurements in a time frame between October 31st, 2018 and January 19th, 2019 (encounter 1 of PSP). Measurement data is analyzed as described in Sec. 2.3 and represents velocity in $\mathrm{km\,s^{-1}}$ (upper panel), density in units of $\mathrm{cm^{-3}}$ (middle panel) and temperature in K (bottom panel).

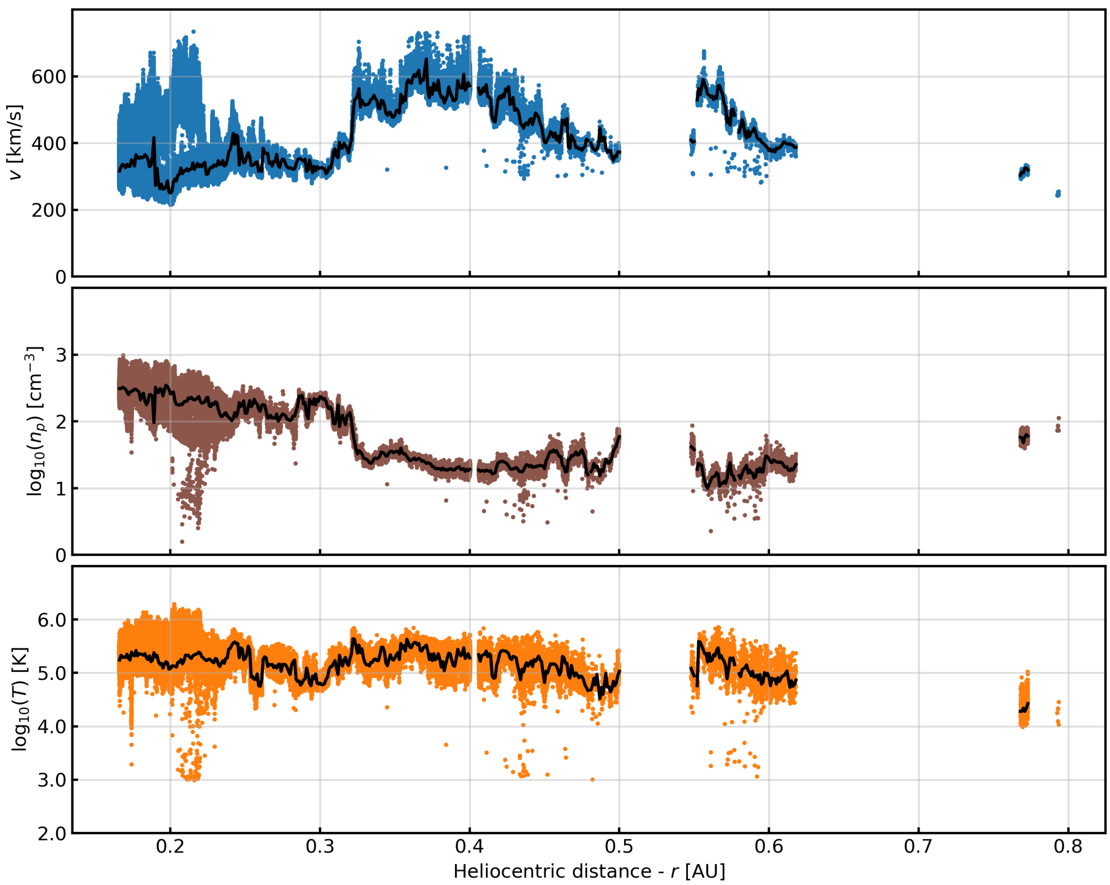

Figure B.3: Same as Fig. B.2, but displaying median values of the parameters in question (solid lines) over the individual data points.

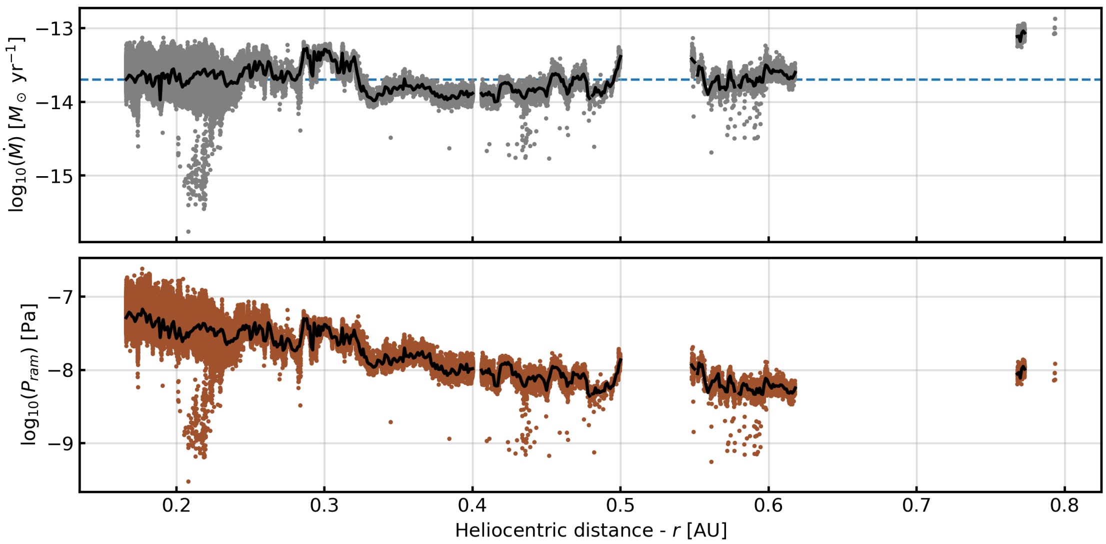

Figure B.4: Mass loss rate in units of $\mathrm{M_\odot\,yr^{-1}}$ (upper panel) and ram pressure in units of Pa (bottom panel) with respect to heliocentric distance in AU, connected to the measurements represented in Fig. B.3. Mean values (solid black lines) are overplotted onto individual data points. The blue dashed line in the upper panel indicates a reference value of $2 \times 10^{-14}\,\mathrm{M_\odot\,yr^{-1}}$ (Wood et al. 2021).

Encounter 2

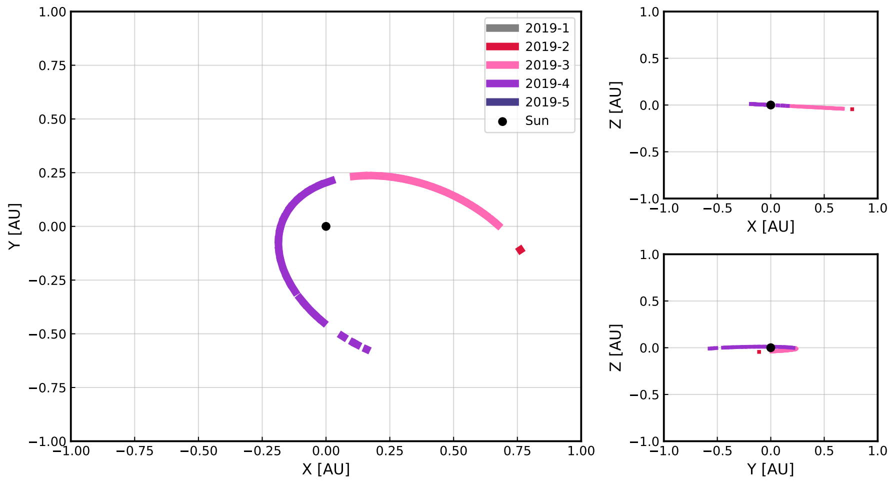

Figure B.5: PSP positional data between January 20th, 2019 and July 19th, 2019, encompassing encounter 2. The three panels illustrate planar cuts in the HIC system, where the xy-plane corresponds to the solar equatorial plane, and the z-axis is aligned with the solar rotational axis. Data points are separated by colour into the respective months of observation. No measurement data is available from July 1st to 19th.

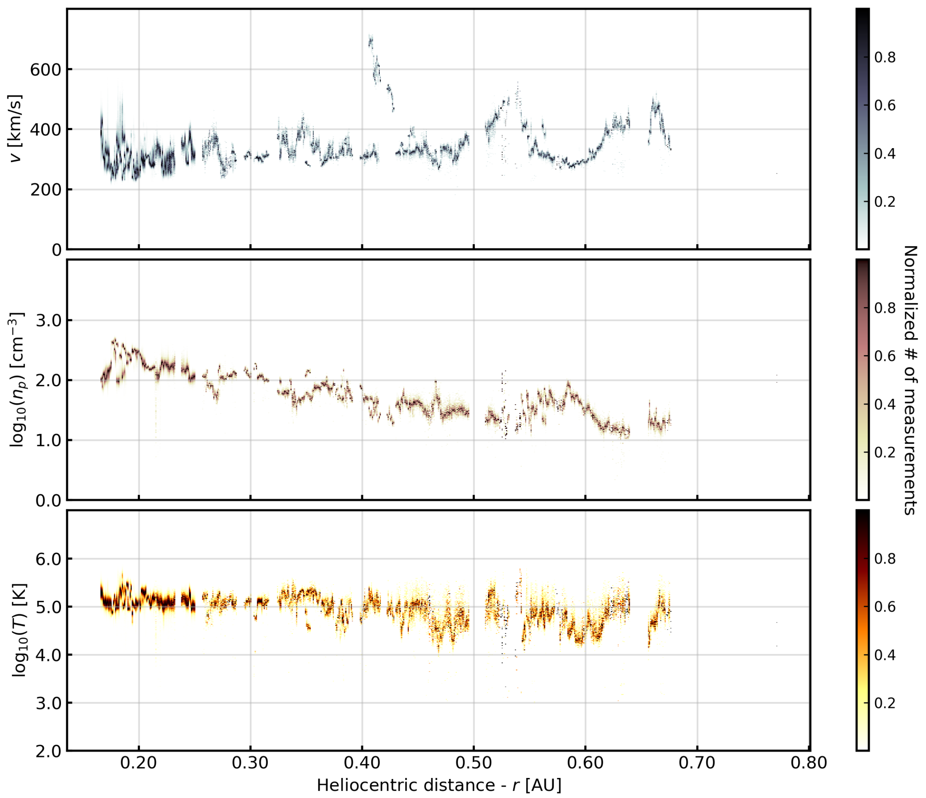

Figure B.6: SPC measurements in a time frame between January 20th, 2019 and July 19th, 2019 (encounter 2 of PSP). Measurement data is analyzed as described in Sec. 2.3 and represents velocity in $\mathrm{km\,s^{-1}}$ (upper panel), density in units of $\mathrm{cm^{-3}}$ (middle panel) and temperature in K (bottom panel).

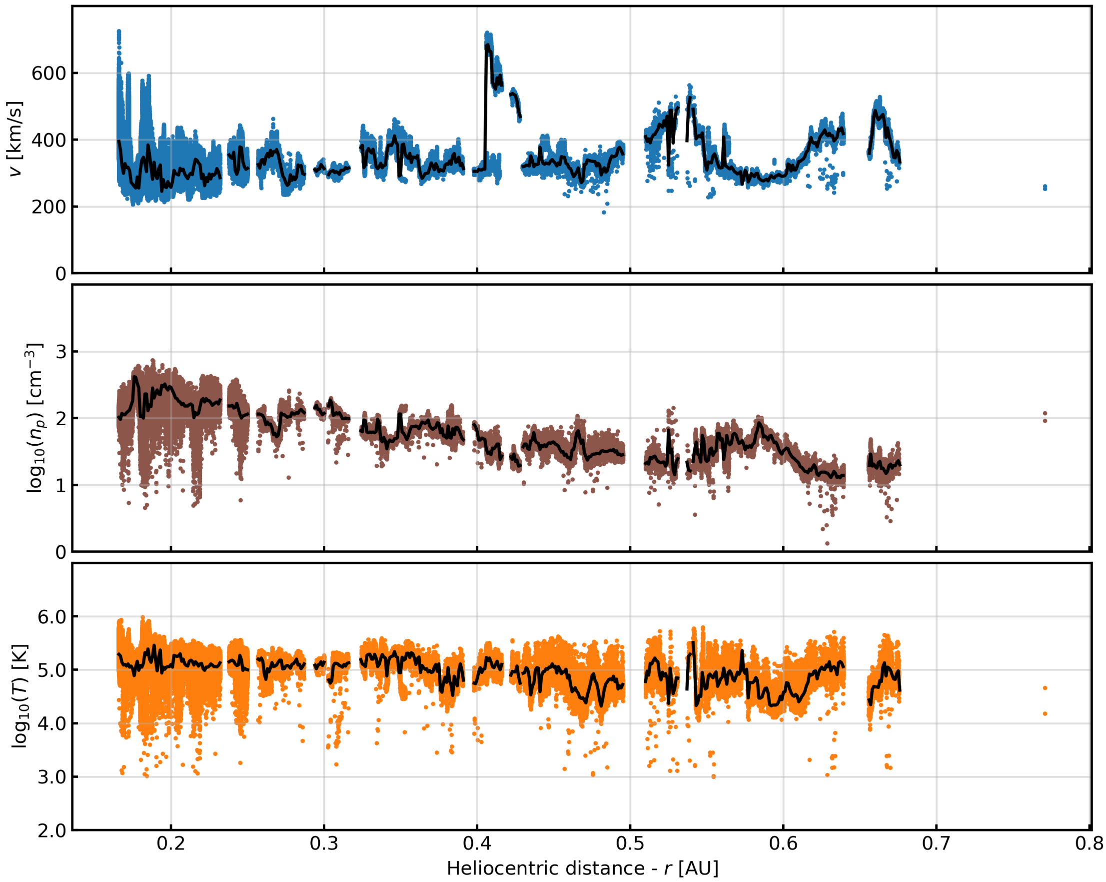

Figure B.7: Same as Fig. B.6, but displaying median values of the parameters in question (solid lines) over the individual data points.

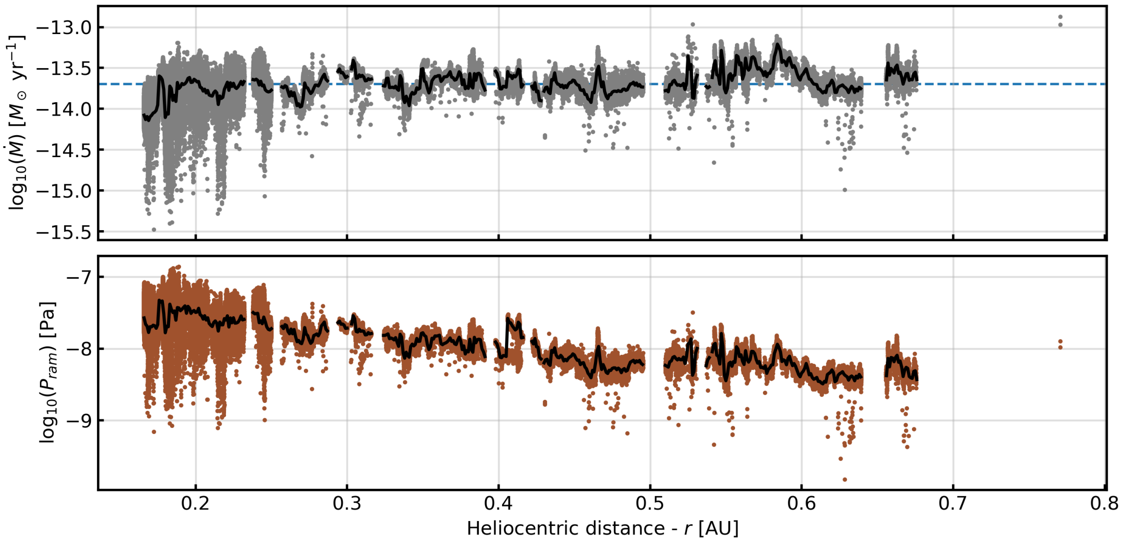

Figure B.8: Mass loss rate in units of $M_\odot\,yr^{-1}$ (upper panel) and ram pressure in units of Pa (bottom panel) with respect to heliocentric distance in AU, connected to the measurements represented in Fig. B.7. Mean values (solid black lines) are overplotted onto individual data points. The blue dashed line in the upper panel indicates a reference value of $2 \times 10^{-14}\,M_\odot\,yr^{-1}$ (Wood et al. 2021).

Encounter 3

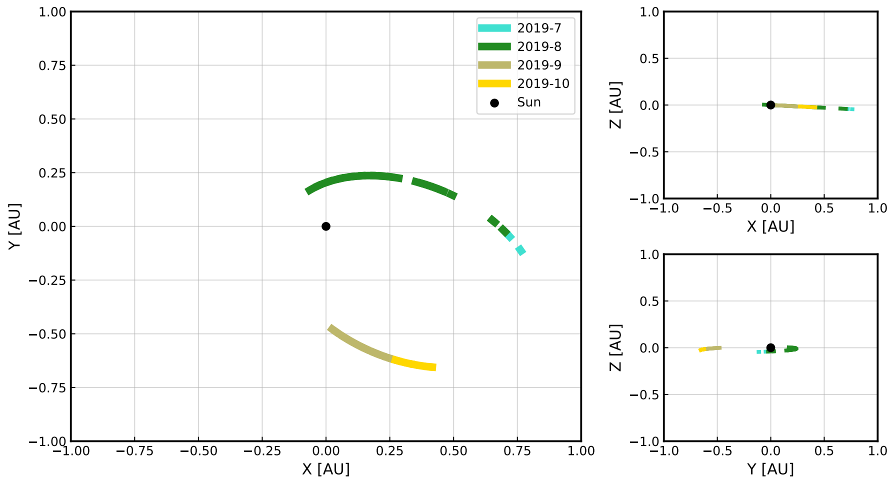

Figure B.9: PSP positional data between July 20th, 2019 and October 13th, 2019 encompassing encounter 3. The three panels illustrate planar cuts in the HIC system, where the xy-plane corresponds to the solar equatorial plane, and the z-axis is aligned with the solar rotational axis. Data points are separated by colour into the respective months of observation.

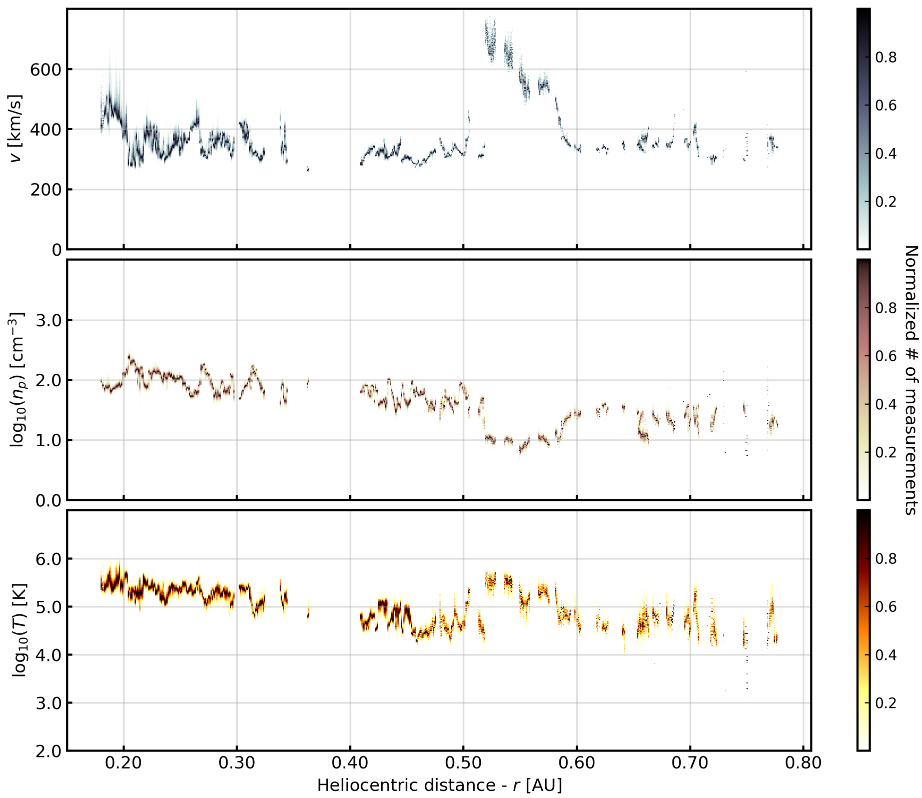

Figure B.10: SPC measurements in a time frame between July 20th, 2019 and October 13th, 2019 (encounter 3 of PSP). Measurement data is analyzed as described in Sec. 2.3 and represents velocity in $\mathrm{km\,s^{-1}}$ (upper panel), density in units of $\mathrm{cm^{-3}}$ (middle panel) and temperature in K (bottom panel).

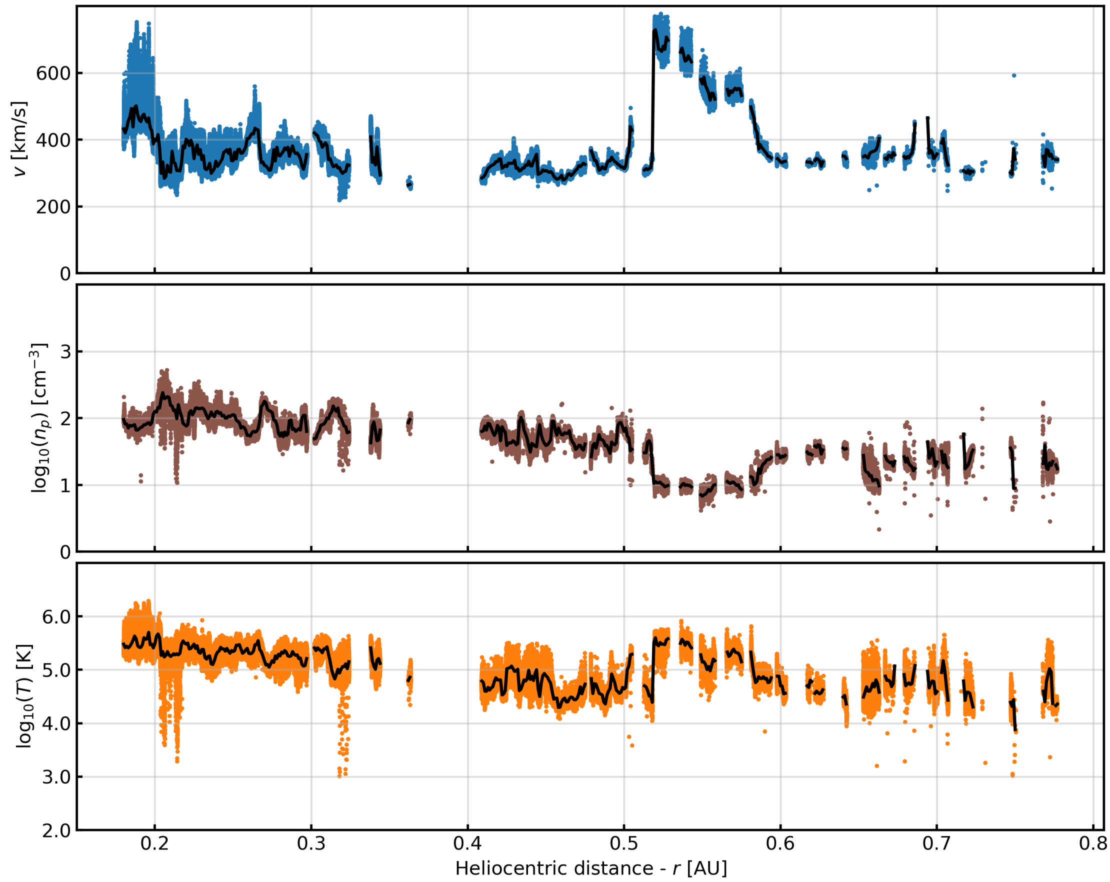

Figure B.11: Same as Fig. B.10, but displaying median values of the parameters in question (solid lines) over the individual data points.

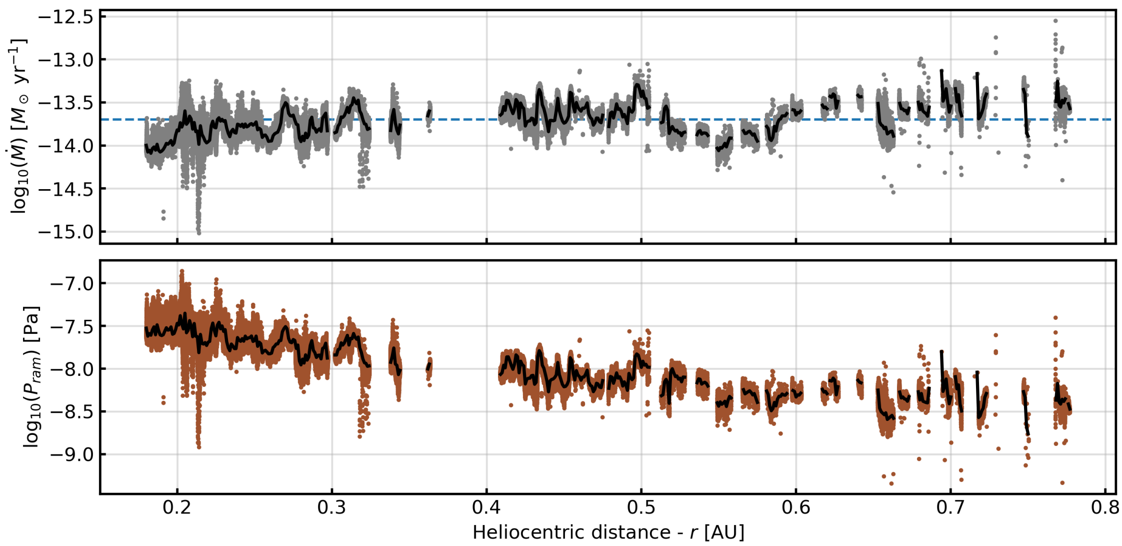

Figure B.12: Mass loss rate in units of $\mathrm{M_\odot\,yr^{-1}}$ (upper panel) and ram pressure in units of Pa (bottom panel) with respect to heliocentric distance in AU, connected to the measurements represented in Fig. B.11. Mean values (solid black lines) are overplotted onto individual data points. The blue dashed line in the upper panel indicates a reference value of $2 \times 10^{-14}\,\mathrm{M_\odot\,yr^{-1}}$ (Wood et al. 2021).

Encounter 4

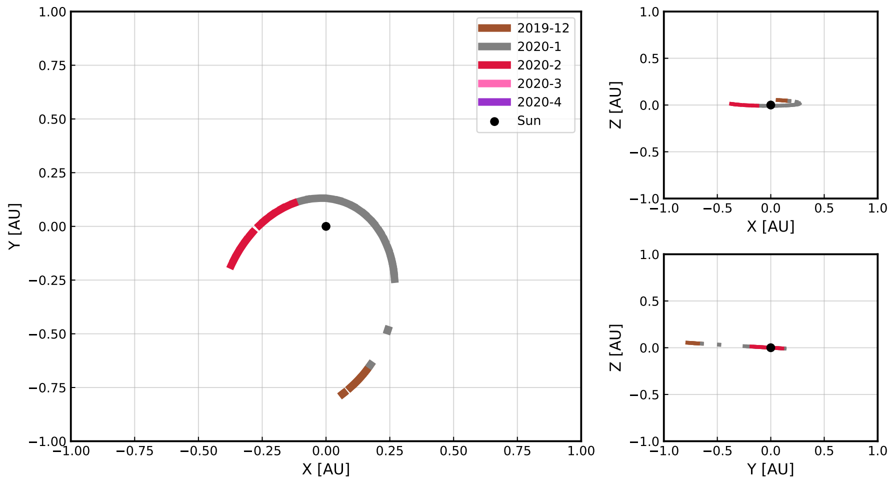

Figure B.13: PSP positional data between October 13th, 2019 and April 30th, 2020 encompassing encounter 3. The three panels illustrate planar cuts in the HIC system, where the xy-plane corresponds to the solar equatorial plane, and the z-axis is aligned with the solar rotational axis. Data points are separated by colour into the respective months of observation.

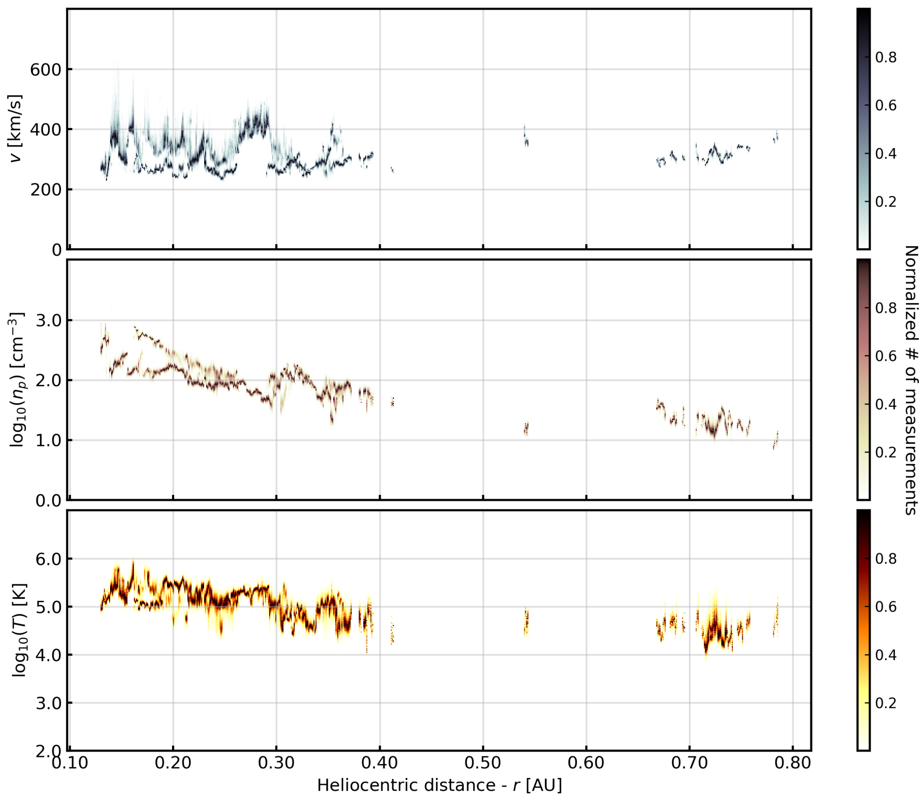

Figure B.14: SPC measurements in a time frame between October 13th, 2019 and April 30th, 2020 (encounter 4 of PSP). Measurement data is analyzed as described in Sec. 2.3 and represents velocity in $\mathrm{km\,s^{-1}}$ (upper panel), density in units of $\mathrm{cm^{-3}}$ (middle panel) and temperature in K (bottom panel).

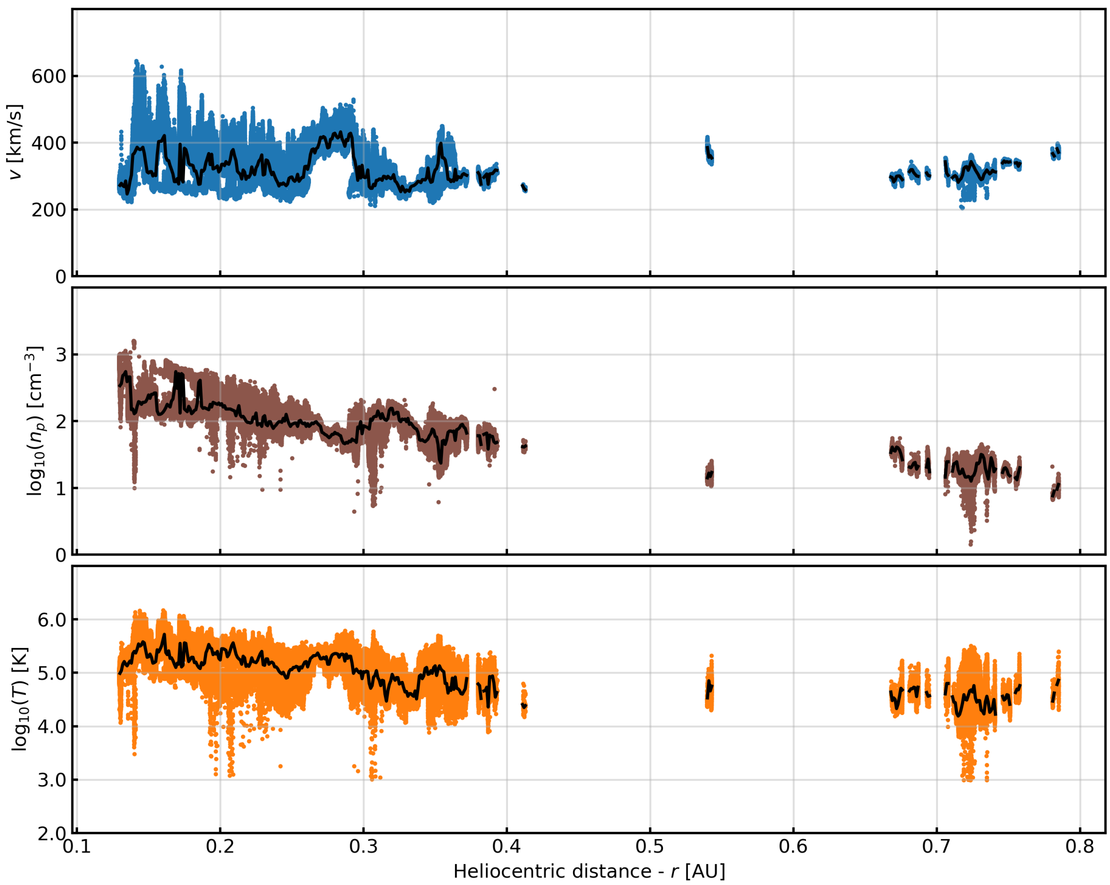

Figure B.15: Same as Fig. B.14, but displaying median values of the parameters in question (solid lines) over the individual data points.

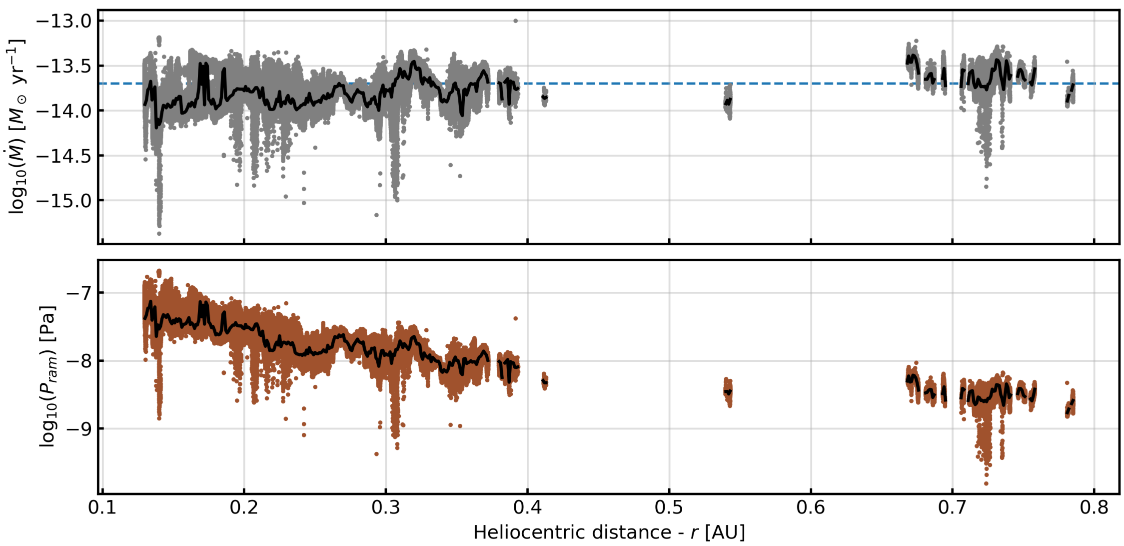

Figure B.16: Mass loss rate in units of $\mathrm{M_\odot\,yr^{-1}}$ (upper panel) and ram pressure in units of Pa (bottom panel) with respect to heliocentric distance in AU, connected to the measurements represented in Fig. B.15. Mean values (solid black lines) are overplotted onto individual data points. The blue dashed line in the upper panel indicates a reference value of $2 \times 10^{-14}\,\mathrm{M_\odot\,yr^{-1}}$ (Wood et al. 2021).

Encounter 5

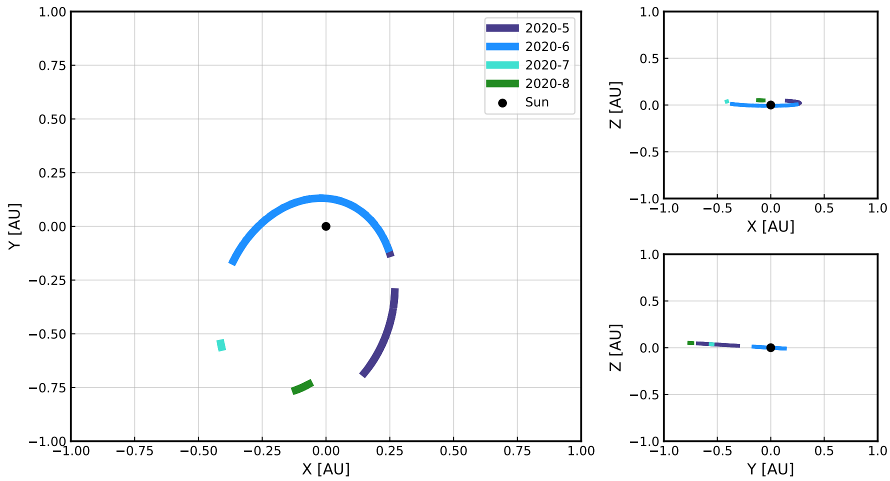

Figure B.17: PSP positional data between May 1st, 2020 and August 22nd, 2020 encompassing encounter 5. The three panels illustrate planar cuts in the HIC system, where the xy-plane corresponds to the solar equatorial plane, and the z-axis is aligned with the solar rotational axis. Data points are separated by colour into the respective months of observation.

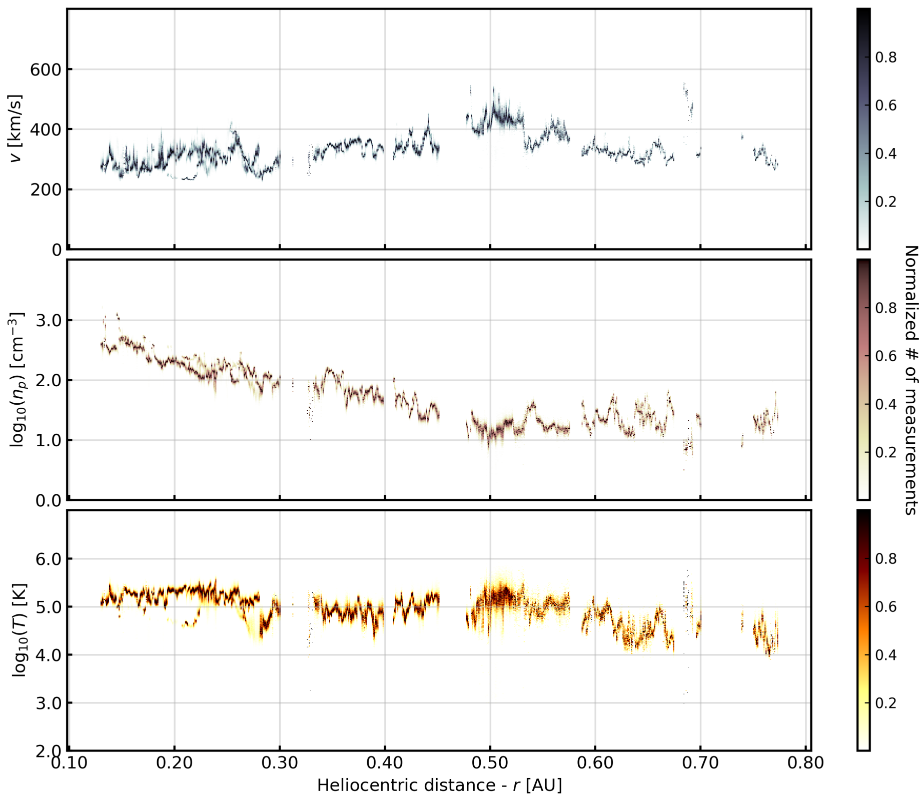

Figure B.18: SPC measurements in a time frame between May 1st, 2020 and August 22nd, 2020 (encounter 5 of PSP). Measurement data is analyzed as described in Sec. 2.3 and represents velocity in $\mathrm{km\,s^{-1}}$ (upper panel), density in units of $\mathrm{cm^{-3}}$ (middle panel) and temperature in K (bottom panel).

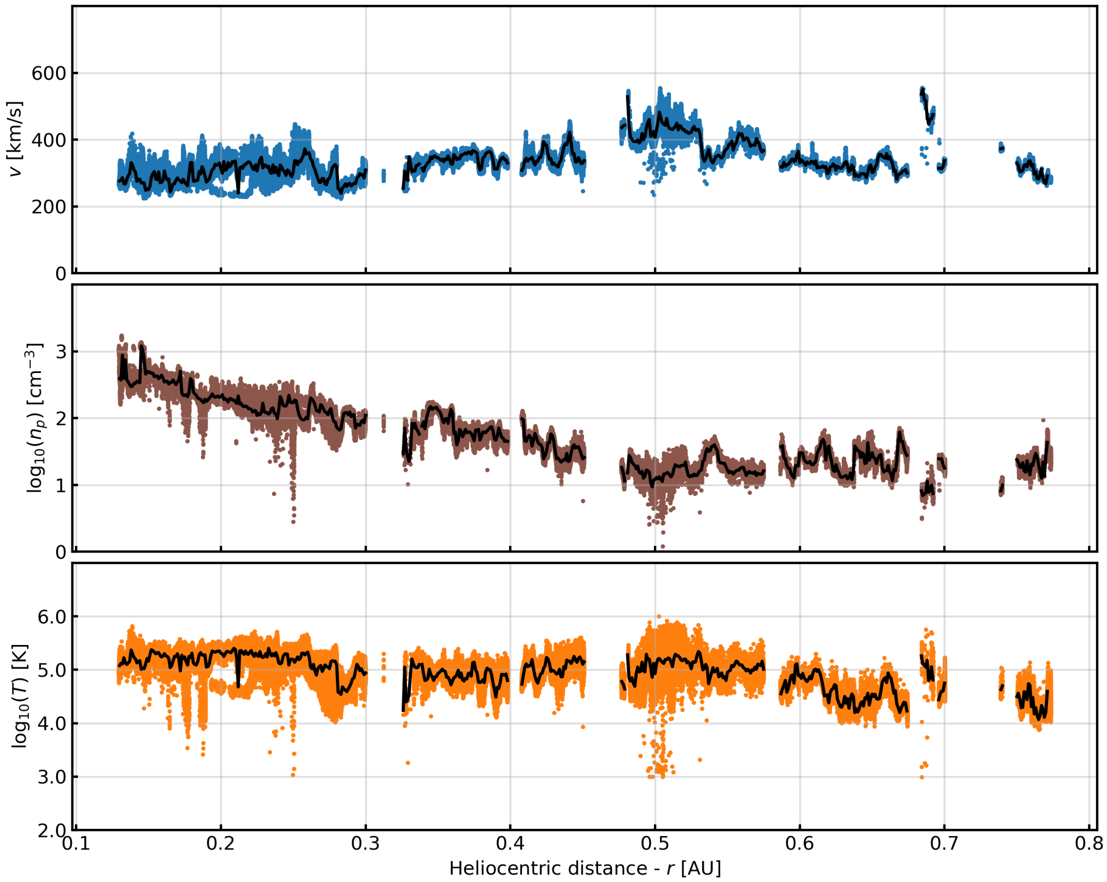

Figure B.19: Same as Fig. B.18, but displaying median values of the parameters in question (solid lines) over the individual data points.

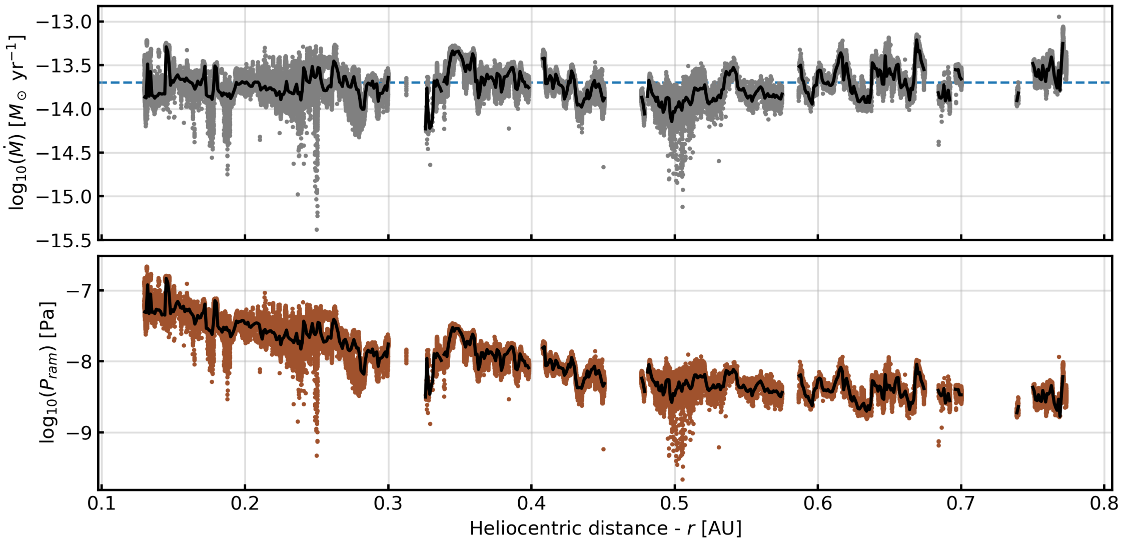

Figure B.20: Mass loss rate in units of $M_{\odot}\,yr^{-1}$ (upper panel) and ram pressure in units of Pa (bottom panel) with respect to heliocentric distance in AU, connected to the measurements represented in Fig. B.19. Mean values (solid black lines) are overplotted onto individual data points. The blue dashed line in the upper panel indicates a reference value of $2 \times 10^{-14}\,M_{\odot}\,yr^{-1}$ (Wood et al. 2021).

Encounter 7

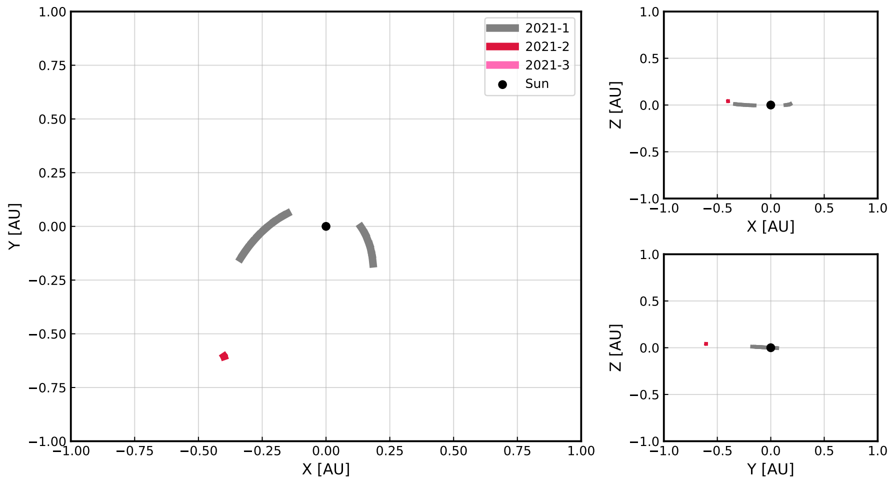

Figure B.21: PSP positional data between January 12th, 2021 and March 17th, 2021 encompassing encounter 7. The three panels illustrate planar cuts in the HIC system, where the xy-plane corresponds to the solar equatorial plane, and the z-axis is aligned with the solar rotational axis. Data points are separated by colour into the respective months of observation.

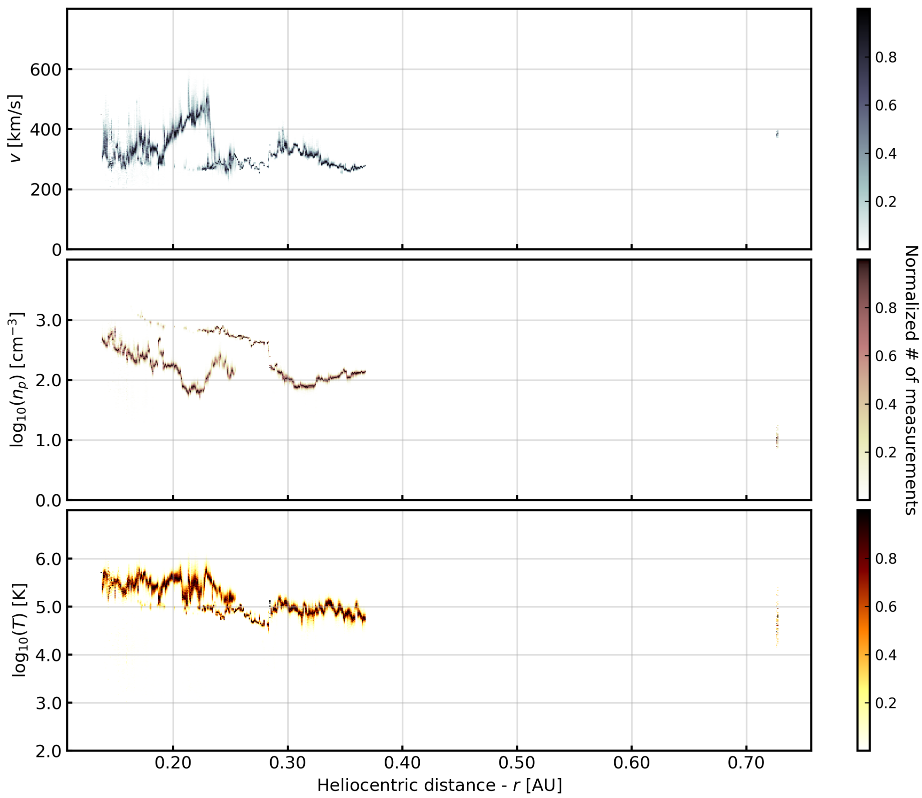

Figure B.22: SPC measurements in a time frame between January 12th, 2021 and March 17th, 2021 (encounter 7 of PSP). Measurement data is analyzed as described in Sec. 2.3 and represents velocity in $\mathrm{km\,s^{-1}}$ (upper panel), density in units of $\mathrm{cm^{-3}}$ (middle panel) and temperature in K (bottom panel).

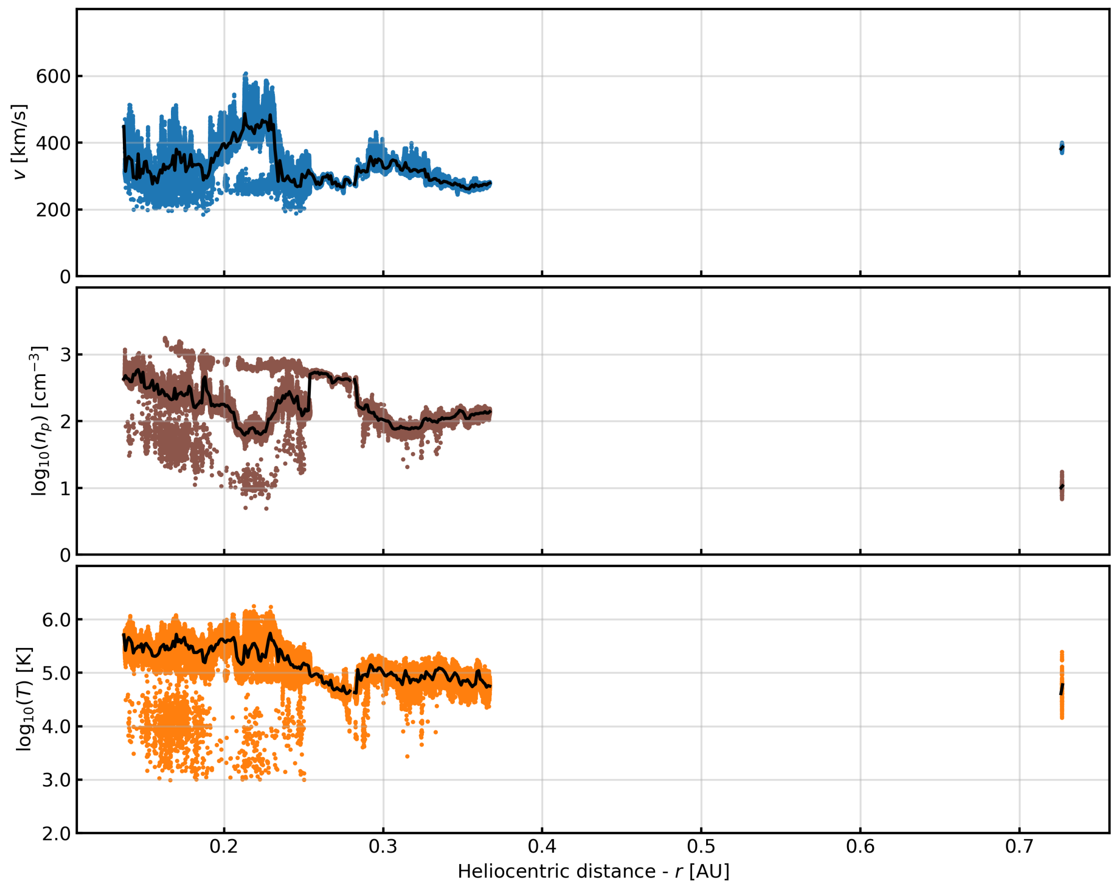

Figure B.23: Same as Fig. B.22, but displaying median values of the parameters in question (solid lines) over the individual data points.

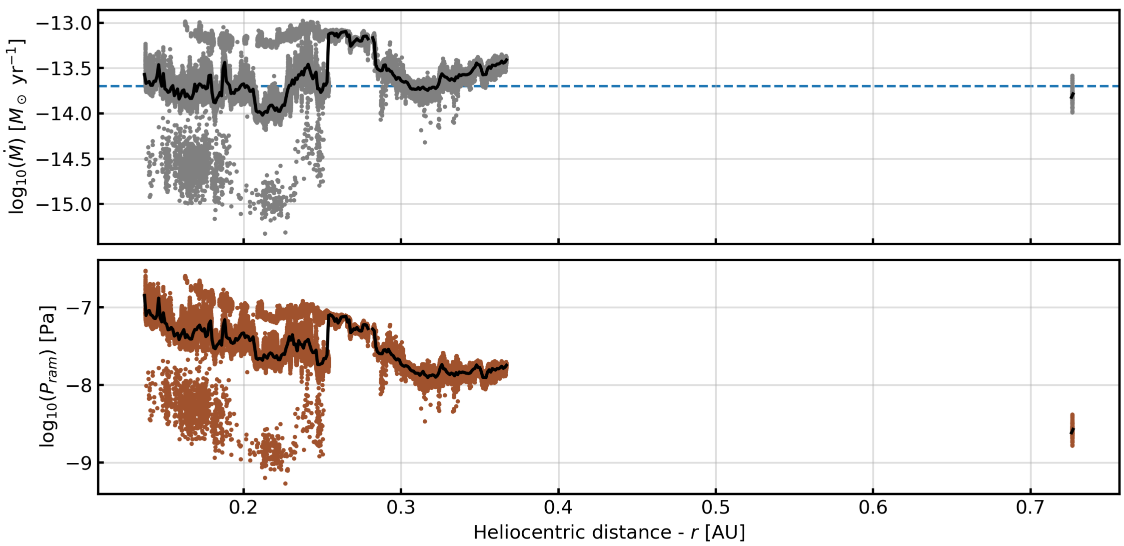

Figure B.24: Mass loss rate in units of $M_\odot\,yr^{-1}$ (upper panel) and ram pressure in units of Pa (bottom panel) with respect to heliocentric distance in AU, connected to the measurements represented in Fig. B.23. Mean values (solid black lines) are overplotted onto individual data points. The blue dashed line in the upper panel indicates a reference value of $2 \times 10^{-14}\,M_\odot\,yr^{-1}$ (Wood et al. 2021).